MULTICELLULAR AGENT-BASED COMPUTATIONAL MODELING APPROACHES TO INVESTIGATE CELL- AND TISSUE- SCALE EFFECTORS OF COLLECTIVE MIGRATION WITHIN AN *IN VIVO* CONTEXT

A DISSERTATION

Presented to the faculty of the

Schools of Medicine and Engineering and Applied Science

in partial fulfillment of the requirements for the degree of

Doctor of Philosophy

---

by TIEN COMLEKOGLU

December 2024

DEPARTMENTS OF BIOMEDICAL ENGINEERING AND CELL BIOLOGY

UNIVERSITY of VIRGINIA

APPROVAL SHEET

This dissertation is in partial fulfillment of the requirements for the degree of

Doctor of Philosophy in Biomedical Engineering

Tien Comlekoglu

Dissertation Author

This dissertation has been read and approved by the examining committee:

Shayn Peirce-Cottler, Ph.D.

Dissertation Advisor

Department of Biomedical Engineering, University of Virginia

Douglas DeSimone, Ph.D.

Dissertation Advisor

Department of Cell Biology, University of Virginia

Silvia Blemker, Ph.D.

Committee Chair

Department of Biomedical Engineering, University of Virginia

James Glazier, Ph.D.

Committee Member

Department of Intelligent Systems Engineering, Indiana University

Jason Kerrigan, Ph.D.

Committee Member

Department of Mechanical and Aerospace Engineering, University of Virginia

T.J. Sego, Ph.D.

Committee Member

Department of Medicine, University of Florida

DEDICATION

When I first walked through MR5 and Pinn Hall in the summer of 2018, I was a bright-eyed bushy-tailed first year medical student who couldn't have imagined being in the position to put together a PhD dissertation. The past four years have been an incredible adventure in mathematics, engineering, and biology that I still catch myself wondering how I managed to find my way into.

I would like to first thank my mentors, Doug DeSimone and Shayn Peirce-Cottler. Thank you both for taking the chance on a medical student who hoped to spend a year learning basic and computational science. I felt so fortunate to be accepted into two supportive and exciting labs each with their own vibrant lab cultures. I felt more fortunate still to receive your support and encouragement to continue my work under your guidance as an MD/PhD student. You were both there to support and encourage me at every step of the way on my road to being a researcher. I am grateful for the endless support and enthusiasm you have shown me towards my work and my wildest science ideas. You have both encouraged me to be a lifelong learner and I could not have been more excited to learn science in both of your labs and at courses and conferences both domestic and abroad.

This dissertation would not have come to be without the support of the DeSimone lab. Our "emergency" lab meetings and fresh frog memes made me excited to come into lab every day. The endless enthusiasm for my naïve suggestions for experiments and demos of in-progress code that came together just in time for lab meeting was infectious and kept me motivated through the ebbs and flows of my PhD. I want to thank Gustavo, Bette, Dave, and Ben for the long hours discussing experiments, gathering imaging, and sharing research dreams.

I want to thank the Peirce-Cottler lab and my community in BME. I'll never forget how our spooky roller coaster rides during Halloween, dramatic white elephants, sudden basketball outings, and late-night walks at conferences always left us with exciting memories to look back on year after year. Thank you to all the Peirce Pirates: Anthony, Rachel, Julie, Ramon, Kareem, David, Lilly, Dori, Lily, Yash, and Christian for allowing me to take part in our wonderful lab culture. I also want to thank Emily, Chris Highley, and the rest of the Highley lab for allowing me to bring sticks on glass to life. And I have to thank my conference crew: Megan, Lexi and Alexis for keeping research fun. I couldn't imagine exploring mathematical biology and agent-based modeling with anyone else.

Finally, I am beyond grateful for the members of my committee. I must thank Silvia Blemker and Jason Kerrigan for setting aside the time to guide me through continuum mechanics and engineering concepts I'd never thought I'd feel comfortable with. I am grateful to James Glazier and T.J. Sego for the near weekly meetings over the years to guide me through building a virtual embryo and discussions on medical digital twins.

My PhD work has been so exciting and fulfilling and I owe it all to everyone I have worked with these past few years. Thank you all and thank you UVA.

-Tien Comlekoglu

Contents

ABSTRACT

The coordinated migration of cells in a collective is a feature of many important biological processes including wound healing, cancer invasion, tissue regeneration, and morphogenesis during development. During collective migration, multiple distinct behaviors of individual cells emerge and can be analyzed. At the cellular length scale, motile cells within collectively migrating tissues typically arrange into leader and follower rows with distinct adhesive properties and protrusive behaviors. Migratory cells at the leading edge polarize and exhibit persistent directed migration in a process termed cohesotaxis. Follower cells intercalate, or rearrange relative to one another, resulting in spreading of the tissue mass. Additionally, intercellular adhesion along with contractility of the cortical cytoskeleton of individual cells results in a fluid-like surface tension across the tissue resulting in tissue reorganization. These cell- and tissue- scale mechanisms driving collective cell migration and tissue reorganization have been characterized experimentally using *ex vivo* tissue preparations from biological systems such as the *Xenopus laevis* embryo. However, these explants are limited in that they lack the context of the *in vivo* environment from which they were removed. Moreover, many of these cellular and tissue-scale processes are difficult to perturb in isolation or *in vivo*. This dissertation explores the development of computational methods to investigate these phenomena *in silico* through multicellular agent-based computational models. I develop and describe Cellular-Potts models to understand the effect of cohesotaxis, intercalation, and tissue geometry on the rate of collective migration of tissue in the developing embryo. I create Cellular-Potts and vertex models to investigate the influence of tissue surface tension in explant tissues. Finally, I describe a novel DLP bioprinted platform for quantifying the micronewton-scale biomechanical forces generated in these explants in representative *in vivo* geometries. In doing so, I explore relative roles of multiple cell- and tissue- scale effectors of collective migration with respect to the gastrula stage *Xenopus laevis* embryo. This work represents progress toward the long-term goal of developing a virtual gastrula-stage embryo.

LIST OF FIGURES AND TABLES

CHAPTER 1: Introduction

Collective cell migration and experimental investigation

Collective cell migration is the coordinated movement of motile cells. The coordinated migration of cells in a collective is a feature of many important biological processes including wound healing, tissue regeneration, cancer invasion, and tissue morphogenesis during development (Friedl and Gilmour, 2009; Li et al., 2013; Mayor and Etienne-Manneville, 2016; Scarpa and Mayor, 2016; Spatarelu et al., 2019; Yang et al., 2019). Collectively migrating groups of cells are distinguished from motile single cells by the coordinated polarization and directed migration of separate but distinct cell populations (termed leader and follower cells) connected via cadherin-based cell-to-cell cell adhesions.(Gov, 2007; Omelchenko et al., 2003; Qin et al., 2021; Rørth, 2012; Shellard and Mayor, 2019). Leader cells exhibit polarized protrusive behavior in the direction of migration. In many cases, follower cells are pulled along due to traction forces generated upon the substrate by leader cells. Leader-follower cell behavior is developed and reinforced through differential Rac- and Rho-mediated signaling cascades in these two populations(De Pascalis et al., 2018; Khalil and de Rooij, 2019; Sonavane et al., 2017; Weber et al., 2012; Zhou et al., 2022). A more complete understanding of the cellular and subcellular mechanisms underlying the regulation of collective cell migration *in vitro* remains a focus of active investigation.

Multiple collective migration movements are required for the proper formation of tissues and organs during early development. Developmental systems have long been models for the *in vitro* and *in vivo* investigation of the biological processes that give rise to the coordination and direction of cells migrating in a collective (Scarpa and Mayor, 2016). *Drosophila melanogaster* trachea and mouse retina are classic examples of collective migration resulting in branching and sprouting morphogenesis of blood vessels(Barbacena et al., 2022; Hayashi and Kondo, 2018; Jeong et al., 2017; Lebreton and Casanova, 2014). Cells of the neural crest that arise during the neurulation stage of development, migrate as a collective to form melanocytes, bone, cartilage, and nerves in vertebrates and are often studied in the frog *Xenopus laevis* and Zebrafish *Danio rerio*(Alfandari et al., 1997; Alfandari et al., 2001; Alfandari et al.,

2003; Szabó and Mayor, 2018; Wei et al., 2010). The multiple collective cell movements of gastrulation are critical to the proper development of the embryo and are classically studied using *Xenopus laevis* as an experimentally tractable model system (Barua et al., 2021; Huang and Winklbauer, 2018; Wacker et al., 1998; Winklbauer, 2020).

During gastrulation in the amphibian *Xenopus laevis*, a coextensive population of mesoderm and endoderm, collectively termed "mesendoderm", involutes at the inferior aspect (or vegetal pole) of the embryo and spreads across the underside of the overlying blastocoel roof (BCR) in the superior direction (toward the animal pole) as a circular mantle of tissue. The advancing, circular leading edge of the mantle of mesendoderm tissue spreads and migrates to a close beneath the BCR at the animal pole of the embryo at the end of gastrulation(Keller, 1976; Keller, 1991; Keller and Jansa, 1992; Keller and Tibbetts, 1989). Leader cells in mesendoderm migrate across the BCR via predominantly α5β1 integrin-dependent adhesions to their fibronectin (FN) rich extracellular matrix, which is assembled by ectoderm tissue along the inner surface of the BCR (Davidson et al., 2002; Davidson et al., 2004; Rozario et al., 2009; Smith et al., 1990; Sonavane et al., 2017; Winklbauer, 1990). Several mechanisms have been reported to influence this migration, such as a chemotactic gradient of platelet derived growth factor (PDGF) in the BCR, (Ataliotis et al., 1995; Nagel et al., 2004; Scarpa and Mayor, 2016; Symes and Mercola, 1996) and a force-dependent process termed cohesotaxis(Weber et al., 2012). Both mechanisms result in polarized protrusions in the forward direction of travel. Cohesotaxis involves the tugging of cells on one another due to integrin-dependent traction forces balanced by rearward cell-cell adhesions and the recruitment of a mechanosensitive cadherin-keratin complex to sites of cell-cell contact[12]. Under these conditions Rac activity and protrusions are inhibited at the rear of leading row cells but increased at the cell front(De Pascalis et al., 2018; Helfand et al., 2011; Sonavane et al., 2017). A similar mechanism termed plithotaxis, involves the orientation of collective cell migratory behavior in culture along the axis of first principal stress(Roca-Cusachs et al., 2013; Tambe et al., 2011). In cohesotaxis, the mechanical coordination of cells within the collective results in high traction stresses concentrated primarily at the

leading edge(Sonavane et al., 2017). These forces are balanced by inter- and intra-cellular stresses in following rows. Additionally, *Xenopus* mesendoderm cells often rearrange relative to one another during closure of the tissue mantle. These cell intercalations can occur in both radial and medio-lateral directions(Davidson et al., 2002) and may affect the speed of mantle closure. Ultimately, factors driven by behaviors of single cells that result in tissue deformations required for vertebrate morphogenesis such as mesendodermal mantle closure include: (1.) individual cell protrusive and migratory behaviors that are self-driven and (2.) cell protrusive and migratory behaviors that are influenced by connections to neighboring cells (e.g., cohesotaxis and intercalation). Studying these processes together, and comparing their relative contributions to one another, is significant because morphogenesis of the tissue *in vivo* is thought to result from the combined action of these processes.

Multiple emergent properties of the tissue have also been described and hypothesized to act to influence closure of the mesendoderm mantle at the end of gastrulation. Differential interfacial tension between planes of distinct cell populations of mesoderm and endoderm towards the end of gastrulation act as a force generating mechanism to produce tissue movements such as convergent thickening and convergent extension(Shook et al., 2022; Zajac et al., 2003). Additionally, specific cell layers in the closing mesendoderm mantle form a supracellular, dense networks of actin in a purse-string formation reminiscent of *in vitro* systems modeling epithelial gap closure (unpublished). Studying these emergent properties is required to yield understanding of how tissues are organized, deform, and migrate which has implications for wound healing, tissue engineering, and cancer metastasis.

A variety of tissue explant preparations have been used to investigate the multiple mechanisms driving collective cell movements of *Xenopus* mesendoderm. These include the dorsal marginal zone (DMZ) explant, the toroid or “donut” explant composed of the bulk of the mesendodermal mantle, and the “In the Round” explant prepared with four juxtaposed DMZ to approximate the toroidal geometry of the mesendoderm(Davidson et al., 2002). Additional explants currently being developed to investigate the emergent property of tissue surface tension to migration include the blastocoel roof (BCR) explant

consisting of a section of the ectodermal BCR at the animal pole of the embryo that mesendoderm has not migrated over, and a roof-less explant consisting of the remainder of the embryo after creation of the BCR explant. The BCR exhibits rapid curling behavior after removal from the embryo, and the roof-less explant exhibits a "flowering" or eversion behavior. Experimental investigation of both of these explants are currently used to investigate the in-vivo behavior and modulation of surface tension in the native collective migration movements during gastrulation (Shook and Dzamba, unpublished observations).

In-silico investigation

Despite the utility of these explant preparations for studies of collective cell migratory behaviors, the mechanism and relative influence to which cell- and tissue- scale behaviors contribute to mesendoderm mantle closure remains difficult to address via experiment alone. Dissection and removal of this tissue from the embryo disturbs features of its native geometry and association with neighboring embryonic tissues (e.g., the BCR and ventral mesoderm and endoderm) resulting in the destruction of biologic structures of interest. Moreover, individual cell rearrangements and intercalation behaviors at tissue-length scales (e.g., in the embryo and/or some explants) are either difficult or currently not possible to image live. Additionally, ongoing work (see Chapter 3) suggests that removal of these tissues from their native environment significantly alters the tissue surface tension. Therefore, in silico models may be an appropriate avenue both for further investigation that is currently not possible through experiment alone and assisting in deriving mechanistic insights from ongoing experimental efforts.

The multiple tissue migration behaviors that characterize mesendoderm mantle closure on the BCR arise in large part from the individual actions of leader and follower cells, and can be considered emergent properties of the tissue. Computational methods such as agent-based modeling are often applied to investigate emergent behaviors that may otherwise be resistant to experimental observation and manipulation (An et al., 2009; Chan et al., 2010; Glen et al., 2019; Yu and Bagheri, 2020). The Cellular-Potts model, also known as the Glazier-Graner-Hogeweg model, is a mathematical framework that allows for agent-based modeling while effectively capturing the inherent stochasticity of cell and tissue

properties including differential adhesion between cells and tissues, and forces exerted by cells upon one another and their extracellular environments. Additionally, the Cellular-Potts model framework has been successfully applied to investigate multiple collective cell movements of interest, such as convergent-extension in *Xenopus laevis* making it a promising choice for investigating tissue emergent behaviors that drive morphogenesis (Belmonte et al., 2016; Graner and Glazier, 1992; Swat et al., 2012; Zajac et al., 2003).

Tissue-scale movements and deformations common in development such as bending or invagination may occur due to asymmetric behaviors at one end of a cell compared to the other due to processes affecting polarity of that cell, or one side of a tissue compared to another(St Johnston and Sanson, 2011). Modeling these processes *in silico* requires detailed manipulation and control of individual cellular shapes and is difficult to perform using the Cellular-Potts model methodology. The Vertex Model methodology is a common model framework that has been developed and used to investigate these phenomena in multicellular tissues(Alt et al., 2017; Fletcher et al., 2014). In the vertex model framework, individual model objects, often representing cells in a tissue, are represented by polygons in a two-dimensional simulation, or polyhedrons in a three-dimensional simulation. Tissues are simulated by connecting these cells into a mesh network of polygons or polyhedrons where vertices, edges, faces, or volumes of the model move and deform subject to forces upon the vertices of the mesh network that approximate mechanical interactions between cells in the tissue(Sego et al., 2023b). The vertex model method has been used to investigate multiple tissue movements in developmental systems such as ventral furrow formation, convergent extension, and neurulation in multiple experimental developmental animal models(Inoue et al., 2016; Spahn and Reuter, 2013; Wang et al., 2020).

Thesis Goals

This dissertation summarizes work undertaken to fulfill the following two goals related to understanding collective cell migration through the development of novel computational modeling tools deployed in conjunction with experiments.

Goal 1: Develop and validate an agent-based computational model of cellular-scale behaviors in mesendoderm tissue

The individual behaviors of migratory mesendoderm cells such as intercalation within the tissue and cohesotaxis to direct polarized migration ultimately give rise to the unique in-vivo geometry and mantle closure dynamics that occur during gastrulation. These mechanisms are difficult to analyze in isolation in *in vitro* preparations and efforts described towards the goals of this aim have resulted in a modular, extendable, agent-based computational model that describes novel implementations of each of these mechanisms alongside biological experimentation to validate model predictions. This work has been published in the journal *Biology Open* with the title "Modeling the roles of cohesotaxis, cell-intercalation, and tissue geometry in collective cell migration of Xenopus mesendoderm"(Comlekoglu et al., 2024). This chapter will additionally describe the currently unpublished work extending this model and the cohesotaxis algorithm to recapitulate native *in vivo* geometry. A description of the methods required to apply the model at physiologic scale to interpret these mechanisms *in silico* using true *in vivo* geometry and cell counts will be provided in the chapter's conclusion.

Goal 2: Characterize tissue-scale mechanical behaviors that affect collective migration in mesendoderm tissue

The *ex vivo* tissue preparations display dramatic tissue movements even when not adhered to a substrate. For example, the toroidal explant not only closes in the absence of crawling, but also demonstrates bulk rotation. Roof-less explants demonstrate an eversion or a "flowering" behavior. All these observed behaviors are thought to be due to the action of tissue surface tension when the tissue is removed from its native environment. Currently, the magnitude of migratory force generated by this tissue in the absence of cell crawling is currently unknown, and the way in which this mechanism is active or is modulated *in vivo* is unclear. In Chapter 3, I will describe the *in silico* Cellular-Potts and vertex models that I have

developed to assist in the investigation of surface tension in the migration of this tissue. In Chapter 4, I will describe the design process of a novel printed biomaterial construct designed to measure the magnitude of forces generated in this migratory process and discuss the implications of these findings for the migration *in vivo*.

In summary, my work results in multiple computational models that allow for the simulation of mesendoderm tissue in the *Xenopus laevis* gastrula that yields predictions that are readily compared to experimental explants. The work in Chapter 2 regarding mesendoderm migration demonstrates unique and novel methods to encode the behaviors of cohesotaxis and intercalation in an agent-based Cellular-Potts model. This model is conveniently extendable to replicate *in vivo* geometry. Work in Chapter 3 establishes tissue surface tension as a possible mechanism that explains dramatic tissue reorganization behaviors of experimental explants in the absence of mesendoderm leader-follower cell crawling dynamics. Finally, Chapter 4 demonstrates that this tissue surface tension likely generates forces on the scale of micronewtons to drive tissue movements, suggesting that there may be an endogenous modulator of tissue surface tension that allows mesendoderm migration through crawling to drive tissue movements *in vivo* as previously described. Ultimately, the multiple Cellular-Potts and Vertex models developed in this dissertation represents progress towards the long-term goal of a virtual gastrula-stage *Xenopus laevis* embryo.

CHAPTER 2: Modeling the roles of cohesotaxis, cell-intercalation, and tissue geometry in collective cell migration of Xenopus mesendoderm

The text in this chapter has been published in Open Biology at the following reference:

Comlekoglu, T., Dzamba, B.J., Pacheco, G.G., Shook, D.R., Sego, T.J., Glazier, J.A., Peirce, S.M., and DeSimone, D.W. (2024). Modeling the roles of cohesotaxis, cell-intercalation, and tissue geometry in collective cell migration of Xenopus mesendoderm. Biol Open *13*, bio060615. https://doi.org/10.1242/bio.060615.

ABSTRACT

Collectively migrating Xenopus mesendoderm cells are arranged into leader and follower rows with distinct adhesive properties and protrusive behaviors. In vivo, leading row mesendoderm cells extend polarized protrusions and migrate along a fibronectin matrix assembled by blastocoel roof cells. Traction stresses generated at the leading row result in the pulling forward of attached follower row cells. Mesendoderm explants removed from embryos provide an experimentally tractable system for characterizing collective cell movements and behaviors, yet the cellular mechanisms responsible for this mode of migration remain elusive. We introduce a novel agent-based computational model of migrating mesendoderm in the Cellular-Potts computational framework to investigate the respective contributions of multiple parameters specific to the behaviors of leader and follower row cells. Sensitivity analyses identify cohesotaxis, tissue geometry, and cell intercalation as key parameters affecting the migration velocity of collectively migrating cells. The model predicts that cohesotaxis and tissue geometry in combination promote cooperative migration of leader cells resulting in increased migration velocity of the collective. Radial intercalation of cells towards the substrate is an additional mechanism contributing to an increase in migratory speed of the tissue. Model outcomes are validated experimentally using mesendoderm tissue explants.

INTRODUCTION

The collective migration of cells is a feature of many biological processes including wound healing, tissue regeneration, cancer invasion, and embryo and tissue morphogenesis (Friedl and Gilmour, 2009; Li et al., 2013; Mayor and Etienne-Manneville, 2016; Scarpa and Mayor, 2016; Spatarelu et al., 2019; Yang et al., 2019). Collectively migrating groups of cells are distinguished from motile single cells by the coordinated polarization and directed migration of distinct leader- and follower-cell populations connected via cadherin-based cell-cell adhesions.(Gov, 2007; Omelchenko et al., 2003; Qin et al., 2021; Rørth, 2012; Shellard and Mayor, 2019). Leader cells exhibit polarized protrusive behavior in the direction of the collectively migrating front. In many cases, follower cells are pulled along as a result of substrate traction forces generated by leader cells. Leader-follower behavior is developed and reinforced largely through differential Rac- and Rho-mediated signaling cascades in these two populations (De Pascalis et al., 2018; Khalil and de Rooij, 2019; Sonavane et al., 2017; Weber et al., 2012; Zhou et al., 2022). A more complete understanding of the cellular and subcellular mechanisms underlying the regulation of collective cell migration *in vitro* remains a focus of active investigation. In addition, there is a need to identify the critical factors governing collective cell movements *in vivo* where more complex tissue geometries (e.g. circularly arranged tissue) and increased length scales play a role (Davidson et al., 2002; Keller and Shook, 2008; Keller et al., 2003; Shook and Keller, 2008).

During gastrulation in the amphibian *Xenopus laevis*, a coextensive population of mesoderm and endoderm, collectively termed “mesendoderm”, involutes and spreads across the underside of the overlying blastocoel roof (BCR) as a circular mantle of tissue. The advancing 360^{o} leading edge of the mesendoderm mantle ultimately meets and fuses to form a layer of contiguous tissue beneath the BCR by the end of gastrulation (Keller, 1976; Keller, 1991; Keller and Jansa, 1992; Keller and Tibbetts, 1989). The assembly and arrangement of these tissues are regulated through multiple mechanisms including the initiation of mesendoderm involution, the coordination of single cell protrusive activity and collective cell

movement, and the directionality and velocity of migration. Leading edge mesendoderm migrates across the BCR using integrin-dependent adhesions to fibronectin (FN) fibrils, which are assembled along the inner surface of the BCR (Davidson et al., 2002; Davidson et al., 2004; Rozario et al., 2009; Smith et al., 1990; Sonavane et al., 2017; Winklbauer, 1990). Several mechanisms have been reported to influence this migration. These include a chemotactic gradient of platelet derived growth factor (PDGF) in the BCR (Ataliotis et al., 1995; Nagel et al., 2004; Scarpa and Mayor, 2016; Symes and Mercola, 1996) and a force-dependent process termed cohesotaxis (Weber et al., 2012). Both of these mechanisms result in polarized protrusions in the forward direction of travel. Cohesotaxis involves the tugging of cells on one another as a result of integrin-dependent traction forces generated at the front and balanced by rearward cell-cell adhesions and the recruitment of a mechanosensitive cadherin-keratin complex to sites of cell-cell contact (Weber et al., 2012). Under these conditions Rac activity and protrusions are inhibited at the rear of leading row cells but increased at the cell front (De Pascalis et al., 2018; Helfand et al., 2011; Sonavane et al., 2017). A similar mechanism termed plithotaxis, involves the orientation of collective cell migratory behavior in culture along the axis of maximal principal stress (Roca-Cusachs et al., 2013; Tambe et al., 2011). In cohesotaxis, the mechanical coordination of cells within the collective results in high traction stresses concentrated primarily at the leading edge (Sonavane et al., 2017). These forces are balanced by inter- and intra-cellular stresses in following rows. Additionally, *Xenopus* mesendoderm cells often rearrange relative to one another during closure of the tissue mantle. These cell intercalation movements can occur in both radial and medio-lateral directions (Davidson et al., 2002) and may affect the speed of mantle closure. Ultimately, factors that drive tissue deformations required for vertebrate morphogenesis such as mesendodermal mantle closure include: (1.) individual cell protrusive and migratory behaviors that are self-driven, (2.) cell protrusive and migratory behaviors that are influenced by connections to neighboring cells (e.g., cohesotaxis and intercalation), and (3.) tissue-level geometries (e.g., a circular multi-cell layered mantle of tissue) that provide physical boundary constraints.

A variety of tissue explant preparations have been used to investigate the collective cell movements of *Xenopus* mesendoderm (Fig 2-1A). These include the dorsal marginal zone (DMZ) explant, the toroid or "donut" explant composed of the bulk of the mesendodermal mantle, and the "In the Round" (ITR) explant prepared with four juxtaposed DMZ explants to approximate the toroidal geometry of the mesendoderm (Davidson et al., 2002). Despite the utility of these explant preparations for studies of collective cell migratory behaviors, how cell and tissue geometry contribute to mesendoderm mantle closure remains difficult to address via experiment alone. Dissection and removal of this tissue from the embryo disturbs features of its native geometry and association with neighboring embryonic tissues (e.g., the BCR and ventral mesoderm and endoderm). Moreover, individual cell rearrangements and intercalation behaviors at tissue-length scales (e.g., in the embryo and/or some explants) are either difficult or currently not possible to image live, or perturb in isolation in the *in vitro* setting.

The three-dimensional tissue geometry and migration behaviors that characterize mesendoderm mantle closure on the BCR arise in large part from the individual actions of leader and follower cells, and can be considered emergent properties of the tissue. Computational methods such as agent-based modeling are often applied to investigate emergent behaviors that may otherwise be resistant to experimental observation and manipulation (An et al., 2009; Chan et al., 2010; Glen et al., 2019; Yu and Bagheri, 2020). The Cellular-Potts model, also known as the Glazier-Graner-Hogeweg model, is a mathematical framework that allows for agent-based modeling while effectively capturing the inherent stochasticity of cell and tissue properties including differential adhesion between cells and tissues, and forces exerted by cells upon one another and their extracellular environments. Additionally, the Cellular-Potts model framework has been successfully applied to investigate multiple collective cell movements of interest, such as convergent-extension in *Xenopus laevis* making it a promising choice for investigating tissue emergent behaviors that drive morphogenesis (Belmonte et al., 2016; Graner and Glazier, 1992; Swat et al., 2012; Zajac et al., 2003).

We present a novel computational model in the Cellular-Potts framework of a DMZ explant of collectively migrating mesendoderm. This model can be used as a methodological examination of collective cell migration, and we apply it here to investigate mesendoderm movements in the Xenopus laevis gastrula. The model replicates the behaviors of a single DMZ biological explant with leader and follower cell agents. We use the model to simulate more complex geometries representative of those in the embryo (Fig 2-1B), and we conduct sensitivity analyses and run *in* silico experiments to investigate how collective cell migration dynamics emerge as a function of cell intercalation, tissue geometry, and cohesotaxis. Our model suggests how cohesotaxis, cell intercalation, and circular tissue geometry each contribute to affect cell migration speed during morphogenesis.

RESULTS

Model Construction

Data from (Davidson et al., 2002), compared the leading-edge migration speeds of "linear" DMZ explants with toroid-shaped "donut" explants. The migration speeds of the toroid explants, which are representative of the tissue geometry *in situ* were over double that of the linear DMZ explants (107 μm/hr vs 237μm/hr, Figure 2-1A). However, arranging four linear DMZ explants in a juxtaposed configuration to create the ITR configuration after collision, resembles the circular toroid explant (Fig. 2-1A), and exhibits migration speed similar to that of the toroid (236μm/hr).

We hypothesize that the circular geometry of the explant tissue in the ITR and toroid configurations directs migratory behavior towards the cell-free opening in the center. Further, the circular tissue geometry enforces a physical boundary on collective cell migration that enables the speed of mesendoderm mantle closure to surpass the rate of collective cell migration when the cells are unbounded on either side, as they are in the single DMZ explant. To address this, we constructed a computational model of the single DMZ explant displayed in Fig. 2-1B. Cells were represented as leader and follower cell agents, two populations of cells with distinct behaviors as described for many examples of collective cell migration. We constructed the *in silico* representation of the DMZ explant using leader and follower cell agents with behaviors described in the Methods. Timelapse images of live DMZ explants (representative example: Movie 1, see *Movie Links and Legends*) were used to guide computational model construction. Representative images of the computational model with a schematic indicating critical model parameters are displayed in Fig. 2-1B, and video of the DMZ model migration is included in Movie 2.

Parameter sensitivity analysis reveals that leading-edge cell lamellipodia parameters drive migration speed of the DMZ explant

As described in the methods, 6 key parameters were built into the model to control migratory behavior in the computational explant (see schematic in Fig. 2-1B). These were queried to determine

which parameters had the greatest effect upon migration speed of the explant (i.e., those parameters most sensitive for migration speed). We performed a one-dimensional sensitivity analysis to measure the effect of each of these parameters on forward migration speed. The analysis was performed by sequentially increasing and decreasing each parameter, while holding all other parameters constant. Parameters were varied in increments of +/- 10% until +/- 50% variation from calibrated baseline levels was reached, with 10 simulated replicates performed for each parameter variation and the percent change in migration speed from reference was observed. The parameters varied included: stiffness of cell-cell connections between cells in the tissue (λ_{Tissue}), cell-substrate connections for leader cell agents ($\lambda_{Lamellipodia}$) and follower cell agents ($\lambda_{FollowerSubstrate}$), the probability of forming new connections for cells to their substrate ($\zeta_{Lamellipodia}$ for leader cell agents, and $\zeta_{Substrate}$ for follower cell agents), and the distance away from a leader cell that a link is formed to reproduce a lamellipodial extension ($\chi_{Lamellipodia}$), as shown in Fig. 2-2 and diagrammed in Fig. 2-1B. An exhaustive list of parameters and their descriptions are included in the Methods.

Our sensitivity analysis revealed that migration speed was significantly affected by the parameters $\chi_{Lamellipodia}$, λ_{Tissue}, and $\lambda_{Lamellipodia}$ according to one-way ANOVA. We fitted a line of best fit through the means of these data, the slope of which corresponds to sensitivity of the output to change in the parameter. Migration speed in the DMZ Explant model was most sensitive to the two parameters $\chi_{Lamellipodia}$, and $\lambda_{Lamellipodia}$. These two parameters are specific to the leading-edge agents (i.e., cells in the leading row), suggesting that the actions of the leading edge cells have a greater effect on the migration speed of the DMZ explant than behaviors of the follower cells. Increasing and decreasing $\lambda_{Lamellipodia}$ was expected to significantly affect migration speed because it represents the magnitude of force exerted by a leading edge cell's lamellipodial protrusion. However, the explanation for why altering the parameter $\chi_{Lamellipodia}$, affects migration speed is not as obvious. While this parameter does not affect the force exerted upon leader cell agents, when this parameter is increased the Cellular-Potts link object is created farther away from a cell agent. In the simulation, leader cell agents migrate forward until they reach their lamellipodia link target, at which point they stop migrating. Link formation is a stochastic process, such

that a longer link allows for more time for a new link to form, and thus fewer interruptions in migration. This may allow the DMZ explant to achieve a greater migration speed due to decreased interruptions in migration on a single cell basis.

Simulating cohesotaxis reveals that polarized migratory activity of leader cells increases explant migration speed

To investigate the effect of a migratory bias on the migration speed of the computational explant, we encoded a mechanism by which leading edge cells are more likely to form lamellipodial protrusions in the direction of migration rather than randomly towards areas of free space. A directional and persistent migratory bias of leader cells along their substrate can be explained by cohesotaxis, a mechanism by which migratory cells in a tissue coordinate mechanically resulting in directed polarized protrusive activity at the leading edge in the direction of migration where cells remain in contact with their neighbors (Weber et al., 2012). To represent cohesotaxis in the model of the DMZ explant, we created a rule for the leader cells such that they preferentially extend lamellipodia away from sites of end-to-end cell-cell adhesion resulting in lamellipodial extension in the direction of migration rather than towards any free edge, thus representing polarized protrusive activity in leader cell agents (Fig. 2-3A). Leading edge cells select a voxel through which a new link's direction is established preferentially from those with the lowest cumulative distance to cell-cell borders in the explant, resulting in creation of lamellipodia away from cell-cell connections in the tissue and towards the direction of migration to maintain persistent migration. The voxel is selected with a probability as displayed in Fig. 2-3B, where parameter κ approximates a kurtosis to modulate the extent to which migratory bias is applied during the simulation. When κ is smaller, there is less migratory bias in the direction of migration, and when κ is larger, there is a greater migratory bias. For further explanation of this parameter, please see Methods.

In silico experiments were performed to investigate the effects of the migratory bias on the migration speed of the explant. The cohesotaxis parameter κ was tuned from a value of -6, representing zero migratory bias, to +6, representing maximal migratory bias. The model was run for n=10 simulations

for each parameter value κ (Fig. 2-3C). Imposing a stronger directional migratory bias by increasing the cohesotaxis parameter resulted in a significant increase in migration speed ($p<0.05$ by independent sample t-test).

Simulating "In The Round" geometry increases migration speed independent of cohesotaxis

We next investigated whether the ITR geometry would increase migration speed. The ITR configuration was simulated by placing four DMZ explants opposed to one another in the simulation environment, just as was performed with biological explants (Movie 3). Migration speed in the ITR configuration was significantly greater than the DMZ explant with cohesotaxis parameter, κ, equal to 6 ($p<0.05$, independent samples t-test, Fig. 2-4B).

To determine whether the ITR geometry provided a directional migratory bias to affect migration speed, we varied the cohesotaxis parameter, κ, throughout the range of 6 to -6 (Fig. 2-3). There were no significant differences between the measured migration speeds across the range of κ values ($n=10$, $p>0.05$ by one-way ANOVA, Fig.4C). The ITR geometry results in the same migration speed regardless of the cohesotaxis parameter. Thus, we suggest that a similar directional bias on cell migration emerges from the ITR geometry. The ITR geometry restricts the direction of migration to the free area bounded by leading edge mesendoderm biasing the direction of migration entirely towards the center of the free area. This contrasts with a single DMZ explant, where the free area in front of the leading edge remains unbounded resulting in a "fanning out" of the leading edge which slows migration as can be observed in biological explant behavior (i.e. both convex morphology and speed of migration). The migrational bias that emerges from the tissue geometry may be a factor assisting mesendoderm mantle closure *in vivo*.

ITR experiments using live explants were repeated to confirm the findings reported in (Davidson et al., 2002)., and to further investigate whether the migratory behavior of DMZ explants was affected by tissue geometry. The migration speed of a single experimental DMZ explant ($N=1$, $n=4$) was compared with the measured speed of five sets of four DMZ explants each placed ITR ($N=2$, $n=10$) (Fig.

2-4E). A movie of a representative ITR experiment is included in Movie 4. A zoomed-in view of one corner highlighting the interface between two colliding explants in the ITR configuration both *in vitro* and *in silico* is included in Movie 5. Before the adjacent *in vitro* DMZ explants made contact with one other at their respective edges, there were no significant differences in migration speeds of the DMZ explants as compared with a single explant *in vitro*. However, after the adjacent DMZ explants made contact with one another at their respective edges, there was a significant increase in migration speed (Fig 4E).

Simulating intercalation allows for increased migration speed

Davidson and colleagues (Davidson et al., 2002) previously reported intercalation behaviors in the DMZ explant, with cells leaving and entering the substrate level, as well as leaving the leading edge. These behaviors were absent in the model as described through Fig. 2-4. To investigate the role of these cellular rearrangement behaviors, we added an additional rule to our model where cell-to-cell link objects that orient cells in fixed locations relative to one another were allowed to break probabilistically based on the parameter ζ_{Tissue}, as described in the Methods section. This behavior allowed for passive cellular rearrangements to occur within the *in silico* tissue, resulting in a different appearance during ITR tissue closure in Fig. 2-5A as compared with Fig. 2-4A due to cell intercalation events within the tissue. A representative simulation time course is shown in Movie 6. While the simulations without intercalation (Fig. 2-4A) retained their rigid bi-layer structure, the simulations with intercalation behaviors (Fig. 2-5A) were observed to flatten to a monolayer over the time course of tissue closure.

Along with the observation that cellular rearrangement via radial intercalation occurs during the ITR closure, previous studies suggested that intercalation may contribute to increased migration speed in the ITR and toroid mesendoderm geometries (Davidson et al., 2002). To test this hypothesis, we performed an *in silico* experiment to compare the ITR model with a ITR model that includes intercalation behavior (parameter $\zeta_{\text{Tissue}} = 0.1$). A significant increase in explant migration speed ($n=10$, $p<0.05$, via independent sample t-test) was observed with the inclusion of this parameter (Fig. 2-5B). The probability of the behavior that allowed for cell rearrangement to occur was then progressively reduced, from the

ζ_{Tissue} value of 0.1 where cellular rearrangement is observed, to ζ_{Tissue} = 0.0001 where cellular rearrangement events become rare and migration speed of closure was approximately equivalent to the model without intercalation. We observed a monotonic decrease in the migration speed with decreasing probability of intercalation behaviors in the tissue (Fig. 2-5C). To validate this prediction *in vitro*, we sought to increase cell intercalation by reducing Ca^{++} present in the DFA media in order to "loosen-up" cadherin-based cell-cell adhesions, allowing for greater cell-cell rearrangement within the tissue. We measured mesendoderm explant migration rates on FN in standard DFA media (1.0 mM Ca++) vs. DFA media containing 0.8 mM Ca++ (i.e., a 20% reduction in Ca++), to weaken cadherin-based cell-cell adhesion. Explants migrated significantly faster in 0.8mM Ca++ DFA than in standard DFA, over an hour of migration (Table S1), consistent with *in silico* model predictions from Fig. 2-5B,C. The migration rate is highest over the first hour (Table 1), which may reflect the limited number of mesendodermal cell layers (2-3 layers) that are available to intercalate onto the fibronectin substrate, such that the frequency of intercalation events decreases over time.

Cellular rearrangement resulted in a flattening of the *in silico* explant, as cells from the layer above shifted down onto the substrate level. We quantified the number of cells on the substrate level for different values of parameter ζ_{Tissue} and observed an increase in the number of cells at the substrate level over the time course of the ITR simulation, as well as in a single DMZ explant simulation, with larger values of ζ_{Tissue} (Fig. 2-5D). This confirms that the top-down intercalation behavior occurs and with greater frequency in both the ITR model and in the single DMZ model with increasing ζ_{Tissue}.

We then confirmed by experiment the model prediction that cell intercalation towards the substrate occurs in the DMZ explant. Fluorescent Dextran-labeled mesendoderm cells were added to the top of an unlabeled DMZ explant migrating on a fibronectin substrate. Over the 30-minute time course of the experiment, labeled cells intercalated in a downward or radial direction toward the substrate to become visible in the bottom layer of cells (Fig. 2-5E, Movie 7). In control DMZ explants lacking any additional labeled cells, cells initially residing in layers above the bottom-most layer of the DMZ explant

gradually appeared in the bottom layer over the time course of the experiment, providing further evidence of intercalation towards the substrate (Movie 8).

DISCUSSION

In this study, we present an agent-based computational model of migrating layers of mesendoderm cells. Our model simulates multiple aspects of collectively migrating cells, including leader and follower cell dynamics, mechanical coordination of cells within the collective in the form of cohesotaxis, and stochastic cell-cell adhesion dynamics that allow for intercalation behaviors to emerge in the model.

This model allows us to investigate the respective roles of cohesotaxis, circular *in vivo* tissue geometry, and intercalation in driving tissue closure in the mesendoderm mantle. The migration speed of a single DMZ explant was sensitive to the directional bias provided by the computational representation of cohesotaxis that we developed and implemented in this work. At the demonstrated ranges, migration rates in our model were sensitive to the stiffness of cell-cell adhesion, leading edge cell-substrate adhesion and lamellipodial extension distance, but robust to cell-substrate link reformation rates and the stiffness of follower cell-substrate adhesion. Future work may explore these parameters over greater ranges. Cohesotaxis allowed cells to migrate synchronously, increasing the measured speed of migration. The method with which we encode cohesotaxis in our agent-based model is directionally agnostic, meaning it works no matter which direction the explant is migrating. This allowed us to perform the ITR experiments *in* silico, as 4 different explants would be migrating towards each other. Additionally, to our knowledge, this method of mathematically encoding cohesotaxis behavior has not yet been described in the literature. When the model was placed ITR, it exhibited migration speed that exceeded the migration speed of a single DMZ explant model even when synchronous migration through cohesotaxis was added. Additionally, this finding was true for all tested values of the cohesotaxis parameter. This suggests that the circular geometry of the tissue also allows for synchronous cell migration to occur, likely because it

restricts the area towards which leader cells may migrate, resulting in cooperative cell migration. Finally, adding additional rules to allow for cell rearrangement behaviors in the explant resulted in a further increase in migration speed as well as the observation that cells intercalated radially (i.e., in the direction of the substrate). This radial intercalation is a model prediction that was validated biologically with the introduction of single labeled mesendoderm cells onto the top of an unlabeled DMZ explant, as well as in control explants. An increase in migration speed in response to intercalation was not reported in earlier studies (Davidson et al., 2002).

Additional validation of model predictions was carried out experimentally by lowering extracellular Ca++ concentration in order to reduce cadherin adhesion and promote radial intercalation. Migration rates are increased in DMZ explants under these conditions as predicted by the model. This change in rate is consistent with an increase in top-down (radial) intercalation brought about by a shift in the balance between cell-cell and cell-matrix adhesion in 0.8 mM Ca++. The likely consequence of additional cells moving to substrate level is more rapid spreading of the explant, thus contributing to the increased rate of migration observed and predicted by the model. Although Ca++ levels in these experiments were reduced by only 20% (standard DFA media contains 1.0 mM Ca++), even modest reductions in Ca++ concentration might affect cellular processes in addition to cadherin-based cell-cell adhesion. However, the 0.8 mM Ca++ used in these experiments is well within the physiological range for interstitial Ca++ levels at gastrulation in *Xenopus*. (Gillespie, 1983)) reported that blastocoel fluid contains 0.5 mM Ca++ at gastrula stages when multiple tissues including the mesendoderm begin to move. Interestingly, interstitial Ca++ concentrations exceed 1.0 mM prior to and after gastrulation (Gillespie, 1983), suggesting that a developmentally regulated drop in [Ca++] may trigger the onset of gastrulation movements by “loosening-up” cells to promote cellular rearrangement and tissue morphogenesis, as first suggested by (Holtfreter, 1944)). We and others have proposed previously that there is a decrease in cell-cell adhesion at gastrulation (Brieher and Gumbiner, 1994) coincident with an increase in cell-ECM adhesion (e.g., (Ramos et al., 1996). Regulation of these stage-dependent

differences in Ca++ concentration may provide a mechanism to promote the dramatic cell and tissue movements that occur at gastrulation. These observations contribute important context for our CPM model and its experimental validation. Moreover, while we altered intercellular adhesion through changes in cell-cell link parameters to produce intercalation in this study, future work could explore replicating intercalation through altered interfacial tension between discrete cells in the CPM framework.

While our model is designed to provide insight into mechanisms driving collective cell migration during mesendoderm mantle closure in *Xenopus* gastrulation, the cell agent behaviors are not specific or particular to this system. Therefore, our model may be extended to other systems known to exhibit collective cell migration, such as cell crawling mechanisms involved in neural crest migration or epithelial gap closure for wound healing or cancer metastasis (Shellard et al., 2018; Spatarelu et al., 2019; Staddon et al., 2018). Our model is specified in the accessible open-source CompuCell3D modeling framework and the behaviors of cohesotaxis and intercalation are specified in Python, allowing users to modify, extend, or re-use model mechanisms in a modular fashion(Sego et al., 2020). Many computational models of cell migration focus on single cell migration in detail (Fortuna et al., 2020; Kumar et al., 2018; Scianna et al., 2013) or collective migration in two-dimensional epithelial cell monolayers(Harrison et al., 2011; Khataee et al., 2020; Nguyen Edalgo et al., 2019; Pan et al., 2021; Staddon et al., 2018; Tetley et al., 2019; Zhao et al., 2017). However, agent-based models built to understand the emergent role of complex three-dimensional tissue geometries have yet to be widely employed. Three dimensional models are better suited to studying tissue morphogenesis because they can capture the mechanics and behaviors of multiple layers of cells.

Our initial model recapitulates many general behaviors prevalent in collectively migrating mesendoderm tissue. At present, it offers limited insight into environmental drivers of migration, such as chemotaxis through PDGF or other biochemical gradients, haptotaxis, or durotaxis. Additionally, the simulated cells in the model's current formulation have limited capacity to deform and are unable to demonstrate dramatic cell shape elongation known to be present in mesendoderm mantle closure

(Sonavane et al., 2017; Weber et al., 2012). These limitations will be addressed in future model iterations by applying the agent behaviors developed in this work to other modeling methodologies, such as vertex model or finite element methods which are able to represent forces and stresses more explicitly present in the tissue during morphogenesis. In addition, the current CPM can be extended to capture the more representative geometry of the toroid explant, which has been investigated in prior experimental work (Davidson et al., 2002; Sonavane et al., 2017). Further interrogation of this model in the context of representative *in vivo* tissue geometry will be pursued in future work. The CPM model adapted to represent more complex geometry would allow for the testing of additional hypotheses for mesendoderm mantle closure *in vivo*, such as the effects of tissue surface tension throughout the mesendoderm (Shook et al., 2022).

In conclusion, we have developed and interrogated a model of collectively migrating cells in a tissue to elucidate the roles of cohesotaxis, circular geometry, and intercalation in modulating tissue migration speed. We describe how cohesotaxis is an important mechanism for enabling cell migration, however the circular geometry of the tissue results in greater migration speed of the explant relative to cohesotaxis. Thus, while cohesotaxis is important for the polarized protrusive behavior of migratory cells, it does not affect the speed of migration in situations of constrained tissue geometry such as ITR. Top-down (radial) cell intercalation behavior provides an additional mechanism contributing to migrating mesendoderm but is not required for mantle closure. Our model predicts previously undescribed contributions of cell intercalation to collective cell migration. 3-D computational models such as the one developed in this study represent a promising tool for the thorough investigation of interdependent mechanisms of tissue morphogenesis. This work has described the development, validation, and application of a novel Cellular-Potts model of collective cell migration to investigate the respective roles of cohesotaxis, cell intercalation, and tissue geometry during tissue morphogenesis of the *Xenopus laevis* gastrula.

METHODS

(1) Computational Methods:

Cellular Potts Model

The *in silico* model representing collectively migrating mesendoderm was constructed in the Cellular Potts (Glazier-Graner-Hogeweg) model framework (abbreviated CPM) using the open-source simulation environment CompuCell3D (Swat et al., 2012). Individual cells in the CPM framework are represented as a collection of voxels on a regular, three-dimensional lattice and are given properties of predefined volume, contact energy with surrounding cells, substrate, and medium, and Hookean spring-like mechanical objects to represent cell-cell adhesion and formation of lamellipodia. These biological properties are represented mathematically in an effective energy functional *H* shown in (1), which is evaluated on a cell-by-cell basis during each computational timestep,

$$H = \sum_{i,j,neighbors} \quad J\left(\tau_{(\sigma(i))}, \tau_{(\sigma(j))}\right)\left(1 - \delta_{\sigma(i),\sigma(j)}\right) + \lambda_{volume}\left(V_{cell} - V_{target}\right)^2 + \left(\sum_{i,j,cell\ neighbors} \quad \lambda_{ij}\left(l_{ij} - L_{ij}\right)^2\right), \qquad (1)$$

where the first term models cell contact energy for neighboring cells with a contact coefficient *J* where *i, j*, denote neighboring lattice sites, $\sigma(i)$ denotes individual cell ID occupying site i and $\tau(\sigma)$ denotes the type of cell σ in the model. The second term describes a volume constraint λ_{volume} applied to each cell where V_{cell} represents the current volume of a cell at a given simulation state and V_{target} is the volume assigned to that cell via the V_{target} parameter. The third term implements an elastic force to represent junctional cell-cell adhesion within the simulated tissue, where λ_{ij} represents the Hookean spring constant of a link object that mediates the elastic force between neighboring cells *i* and *j*, *l* represents the distance between the centers of mass of neighboring cells, and *L* is the target length of the link object. In addition to cell-cell adhesion, elastic links also model attachments that follower cells form with their substrate. Cell-cell adhesion and follower cell-substrate adhesion is appropriately modeled via this elastic term in the CPM which reflects the influence of the cellular cytoskeleton in this integrin-based

attachment(Adhyapok et al., 2021). Leading edge cells have an additional term detailed in equation (2) to represent the constant-tension traction force between the cell's lamellipodium and the substrate; as the stalling force for such cellular processes is likely length-independent and appropriately modeled in a CPM by elements exerting length-independent tension(Belmonte et al., 2016; Bornschlögl et al., 2013; Romero et al., 2012). Attachment to the substrate is defined as the elastic model object directed from the center of mass of a cell agent to a voxel representing the substrate.

$$H = \lambda_{Lamellipodia} * l \quad (2)$$

Extension-retraction behaviors of leading edge lamellipodia and follower cell-substrate attachments are modeled as Poisson processes whereby the probability P_τ of an extension-retraction event occurring per computational timestep is defined by equation (3). Extension-retraction behaviors are represented by the removal and subsequent formation of a new elastic model objects.

$$P_\tau = 1 - e^{\zeta * \Delta t} \quad (3)$$

Poisson parameter ζ was calibrated for leader and follower cell agents to allow the model to reflect observed mesendoderm cell-substrate attachment and single-cell movement behavior replicated from video data collected for the development of the model. Representative video of a live DMZ explant with leader and follower cells is included in Movie 1**.** Parameter values selected to reproduce observed biological explant behavior are displayed in Table 1. Units for CPM parameters are given when possible, however exact units for certain parameters in the CPM methodology is often difficult to determine given the method's reliance on statistical minimization of the abstract effective energy functional to reproduce stochastic cellular behaviors.

The CPM model recreates cell movement using principles defined in equations 1-3 by randomly selecting pairs of neighboring voxels (y, y') and evaluating whether one voxel located at y may copy itself to its neighboring pair at y'. This voxel copy attempt, denoted $\sigma(y,t) \rightarrow \sigma(y',t)$, occurs with the

probability defined by a Boltzmann acceptance function (equation 4) of the change in the effective energy of the system *H* as defined in equation 1.

$$\Pr\left(\sigma(y,t) \to \sigma(y',t)\right) = e^{-\max\left\{0,\frac{\Delta\mathcal{H}}{\mathcal{H}^*}\right\}} \quad (4)$$

The CPM temperature parameter $\mathcal{H}^*$ affects likelihood of accepting voxel copy attempt if system effective energy is increased, whereas voxel copy attempts that decrease system effective energy are always accepted. $\Delta\mathcal{H}$ is the change in system effective energy after a voxel copy attempt.

Model Initialization and simulation:

The geometry of a biological DMZ explant was approximated by simulating a tissue 8 cells in width, 4 cells in length, and 2 cells in height where each cell occupies 5x5x5 voxels to represent cells approximately 30x30x30 μm in size. The explant is placed upon a flat substrate for the simulated cells to form mechanical link attachments in order to represent cell-substrate adhesion.

During model initialization and generation of explant geometry, 8 cells at an assumed leading edge of the explant model are assigned to be leader cell agents and the remaining cells are assigned to be follower cell agents. Cells do not change type during the simulation. Leader cell agents extend mechanical link objects of constant tension from their cell centroids out to the substrate in the direction of a randomly chosen voxel along the cell border with its medium to establish an initial forward direction for the explant to begin migration. Follower cells bordering the substrate similarly extend Hookean spring-like mechanical link objects to their substrate to simulate their cell-substrate adhesion behaviors. All cells establish Hookean spring-like mechanical links to their neighbors at the start of the simulation to recreate cell-cell adhesion.

Each timestep, leader cell agents delete and form new cell-substrate links to create lamellipodial extension and retraction behavior with a frequency governed by their defined probability (Eqn. 3). New links are established in a direction decided by sampling randomly from a location along the leader cell

agent bordering the medium, that is, the free-edge of a leader cell agent. Should the leader cell be surrounded by other cells such that it does not have a free edge as can be seen in representative screenshots of the ITR experiments (Figures 4A, 5A), leader cells do not extend links representative of lamellipodia, thus behaving effectively as follower cells. Follower cell agent cell-substrate adhesion similarly deletes and re-forms according to its defined probability during each computational timestep. A computational timestep was selected to represent 5 seconds of real-world time. Representative video of a DMZ explant migration along a simulated substrate is demonstrated in Movie 2.

Model Validation:

To validate the model, the CPM model was applied to reproduce an experiment previously performed in (Davidson et al., 2002). The model was simulated to migrate for approximately 17 minutes to reach a steady state of migratory behavior before stopping all further leading edge lamellipodial link objects from being formed. The remaining links at this timepoint and beyond were allowed to disappear as a function of their probabilistic lifetime in the model, which resulted in a retraction event comparable to an experiment introducing a function-blocking monocolonal antibody (mAB) to fibronectin preventing any further lamellipodial connections (Fig. 2-6A-D). The baseline or reference parameterization that was chosen initially to match migratory behavior from movies of the biological explant was able to reproduce comparable mean retraction distances to those reported in (Davidson et al., 2002) from n=10 simulations (Fig. 2-6E). This demonstrates that the chosen reference parameterization and resulting model agent-based behaviors are able to reproduce a similar directional tension known to be present in the biological explant and that these mechanical properties produce model events on a spatial scale that can be compared to experimental conditions.

Simulating Cohesotaxis

Cohesotaxis is a mechanism by which adherent cells coordinate mechanically to establish a persistent direction of migratory behavior (Weber et. al. 2012). We have encoded a bias to the direction to

which leader cell agents in our computational model migrate to represent cohesotaxis along with a tunable parameter to modulate the extent to which this bias is applied. To allow for investigation of the ITR geometry, our method of simulating cohesotaxis must be agnostic to the direction the tissue faces. To implement this mechanism, when leader cell agents form new cell-substrate mechanical links to represent lamellipodial cycling behavior during model evaluation, leader cell agents must select preferentially from free-edge voxels in the direction most opposed to sites of cell-cell adhesion rather than selecting a random voxel from the list of eligible free-edge voxels. Free-edge voxels are defined as voxels belonging to a cell agent that exist in contact with medium as opposed to in contact with other cells. Therefore, during formation of a new mechanical link object, the list of eligible free-edge voxels is sorted by cumulative distance to all cell border voxels. The free edge voxel through which a new link's direction is established is selected preferentially from those in the direction of migration, or most opposite from cell-cell contacts. This behavior was created in the model by selecting with greater weight given to voxels with the lowest cumulative distance to the list of cell border voxels. The voxel is selected by the probability defined in Fig. 2-7B, where cohesotaxis parameter κ approximates a kurtosis of the probability distribution function to tune the extent to which the migratory bias is applied during the simulation.

To ensure that our algorithm is consistently applied regardless of how many free-edge voxels an individual cell may have at a given moment, we define a bias probability function evaluated at the time of a new leading edge lamellipodia link formation. This is established by defining a sigmoid-like function as described in equation (5) within a consistent viewing window of -5,5 with a length that corresponds to the number of free edge voxels for the individual leading cell agent. Multiple example functions are displayed in Fig. 2-7A, for different values of κ within the consistent, window of x = (-5,5).

$$f(x) = \frac{1}{1+e^{-(-x-\kappa)}} \quad (5)$$

Values of $f(x)$ for each function were normalized by the sum of the function within the viewing window to convert the vector $f(x)$ into a vector of probability weights that sum to 1 such that a list of an arbitrary number of sorted voxel objects could be selected using the vector of probabilities and

subsequently used to encode agent-based behaviors in the CompuCell3D simulation software. Normalized probability functions for different values of κ are shown in Fig 7B. The direction of a link object representing lamellipodia is defined by the selecting free-edge voxels through this algorithm, whereas the distance away from the selected voxel to which a link object is created is defined by parameter $\chi_{\text{Lamellipodia}}$

Simulating the In The Round (ITR) configuration

We simulated the ITR configuration by placing 4 DMZ explants orthogonal to one another in the same simulation space. We did not change other parameters intrinsic to the model or CPM framework to recreate the in-the-round configuration, and allowed the single DMZ explant model behaviors drive the ITR simulation.

Allowing cell intercalation in the computational model

Cell rearrangement behaviors that result in cell intercalation were enabled in the model by deleting and re-forming mechanical link objects that represent cell-cell adhesion within the tissue. When mechanical link objects are removed and re-formed, the CPM Potts algorithm causes cells to shift and rearrange in the tissue encouraged by link formation to new cell neighbors. Link objects were defined to have a lifetime modeled as a Poisson process as described by equation (3), where Poisson parameter ζ_{Tissue} represents a parameter to allow for variable frequency to which cell-cell adhesion links break and re-form. During model simulation, if a cell-cell adhesion link has been determined to break based on evaluating this probability, then the cell will form a new cell-cell adhesion link with a random neighbor to which it does not currently have a cell-cell adhesion link until a maximum of 4 neighbors is reached. This allows cell intercalation behaviors to emerge within the model. The maximum number of neighbors remains a tunable parameter in the model code, however we have observed that parameter values of 3 or lower, or 6 and greater, result in unrealistic tissue behavior. This value allows the tissue to be fluid enough to rearrange but connected enough to prevent it from falling apart at a range of ζ_{Tissue} values.

Migration speed measurements:

Single DMZ *in silico* experiments were performed by allowing the DMZ model to run for a period of 2 hours while sampling leading edge centroid locations approximately every 17 minutes (every 200 timesteps). The average distance traversed by the center four leading edge cells of the explant were then calculated. Migration speed was determined to be the average speed of these cells of the explant in the direction of migration over the 2 hours.

Closure speed in the ITR experiments was determined by measuring the free area towards which the explants migrated during simulation of closure of the mesendoderm mantle. The area of the cell-free space in the center of the ITR configuration was measured and the rate of change of the length of one side ($\sqrt{Free\ Area}$) was used to determine the migration speed of the tissue.

(2) Experimental Methods

Animal Models

Gametes were obtained from adult *Xenopus laevis*, eggs fertilized and embryos reared to gastrula stages using standard methods(Sive et al., 2000). Animal housing and care protocols were approved by the Animal Care and Use Committee (ACUC) at the University of Virginia.

Migration speed measurements

DMZs were dissected from stage 10.5 embryos and placed on glass bottomed dishes coated overnight with 10 ug/ml Fibronectin (Sigma F1141) at 4 degrees C. For ITR measurements four DMZs were arranged orthogonally as described in (Davidson et al., 2002). Images were acquired every 5 minutes for 3 hours. The distance migrated by the free edge over 40 minutes was calculated before and after adjacent DMZs contacted one another. Single DMZs were allowed to migrate for at least one hour then imaged for 30 minutes. The average distance migrated by 4 leading edge cells per DMZ was calculated.

Confocal imaging of DMZs ITR

DMZs ITR were fixed for 10 minutes with 3.7% formaldehyde, .1% glutaraldehyde in 20 mMTris 150 mM NaCL pH7.4 containing 0.1% Tween20. The explants were then incubated overnight with a 1:100 dilution of Alexa488 Acti-stain (Cytoskeleton PHDG1) and imaged using a Nikon AX confocal microscope and a10x objective.

Observing substrate-level intercalation in the biological DMZ explant

DMZ explants were dissected from stage 11 embryos and placed on glass bottomed dishes coated with FN. Mesendoderm tissue was dissected from embryos that were injected with Alexa488 dextran and dissociated in calcium and magnesium free MBS to obtain single cells. After 30 minutes of migration dissociated cells were "sprinkled" on the migrating DMZ explants. Beginning 90 minutes after the cells were added Confocal z stacks (13 x 2 um sections) were obtained at one minute intervals with a Nikon AX confocal.

Measuring migration in calcium-reduced media

For data displayed in Table S1, ME was explanted from embryos at St 10.5 to 11.5 and cultured in DFA (Sater et al., 1993) or DFA made with 0.8 mM Ca++ and Mg++ (i.e., 20% less Ca++ and Mg++ than standard DFA with 1.0 mM Ca++ and Mg++). Petri dish surfaces were coated with 10 or 20 mg/ml FN for 30' at 37°C.

Images were captured every 2 minutes on a Zeiss AxioZoom dissecting microscope. One to three points across the leading edge of the migrating ME were tracked every 10 minutes using the ObjectJ plugin in ImageJ(Schindelin et al., 2012). Displacement of each point over time for the first 1 and 2 hours of migration was determined and the point with maximum velocity was used for the analysis of each explant. Explants which showed a great deal of slippage (tendency to snap back) or failure to migrate over the first two hours were not included in data analysis. Migration rates were subjected to two-way ANOVA, to account for differences in rate between clutches, differences in stages, and FN amount.

(3) Statistical Analysis

For pairwise comparisons, unpaired, two-tailed, Student's *t*-tests were used to determine P values. For multiple-group comparisons, we used one-way ANOVA to determine whether multiple groups had a common mean. We did not perform post-hoc testing following an ANOVA because the presence or absence of a difference in the means of the multiple groups were sufficient for our analysis. *P* values are as follows: P>0.05 (not significant, ns), * P<0.05, *** P<0.001. All error bars represent standard deviation (s.d.) except Figure 6, which shows standard error of the mean (s.e.m) to remain consistent with data reported in (Davidson et al., 2002).

SUPPLEMENTARY DATA

Mesendoderm migration in standard DFA with 1.0 mM Ca++ vs. DFA with 0.8 mM Ca++

Table 1 DMZ explant migration in reduced Ca++ media

	DFA with 1.0 mM Ca++ (um/hr; n = 12, from 4 clutches)	DFA with 0.8 mM Ca++ (um/hr; n = 11, from 4 clutches)
1 hr	113	139*
2 hr	110	126

Mean rate of migration over first 1 hour or first 2 hours in standard DFA media vs. DFA with 0.8 mM Ca++ and Mg++. Migration rate during the first hour was significantly different (* p = 0.044) between standard Ca++ reduced DFA by two-way ANOVA. See *Methods* for further details. Experiments performed by David Shook.

MOVIE LINKS AND LEGENDS

Movie 1: **Timelapse movie of single DMZ explant on fibronectin.** Actin (magenta) and Keratin (green) were labeled by injection of mRNA transcript encoding LifeAct-RFP (actin) and XCK-GFP (cytokeratin filaments). Confocal Z-stacks were collected at 2 minute intervals (15 frames). URL: https://movie.biologists.com/video/10.1242/bio.060615/video-1

Movie 2: **Timelapse sequence of a simulated single DMZ explant migrating on a substrate.** URL: https://movie.biologists.com/video/10.1242/bio.060615/video-2

Movie 3: **Timelapse sequence of four simulated DMZ explants in the ITR configuration.** URL: https://movie.biologists.com/video/10.1242/bio.060615/video-3

Movie 4: **Four DMZs migrating on a fibronectin coated substrate in the round (ITR).** Actin (greyscale) was labeled by injection of mRNA encoding LifeAct-RFP. Two of the four DMZs were labeled with Alexa 488 dextran (magenta-left panel) to identify individual DMZs. Confocal Z-stacks were collected at 2 minute intervals (25 frames). The debris in the center of the 4 DMZs is yolk granules released from the cells during microdissection. URL: https://movie.biologists.com/video/10.1242/bio.060615/video-4

Movie 5: **Interface between two DMZs *in vitro* (left) and *in silico* (right) migrating from 4 DMZs placed ITR.** Left: Actin (greyscale) was labeled by injection of mRNA encoding LifeAct-RFP. Two of the four DMZs were labeled with Alexa 488 dextran (magenta-left panel) to identify individual DMZs.

Confocal Z-stacks were collected at 3 minute intervals (11 frames). Representative frames from a ITR simulation are shown on the right. URL: https://movie.biologists.com/video/10.1242/bio.060615/video-5

Movie 6: **Timelapse sequence of four simulated DMZ explants in the ITR configuration with cell intercalation allowed.** URL: https://movie.biologists.com/video/10.1242/bio.060615/video-6

Movie 7: **Timelapse movie showing integration of single dextran Alexa488-labeled cells applied onto an unlabeled DMZ explant migrating on fibronectin substrate.** Mesendoderm cells, labeled by injection of Alexa488 dextran (green), were dissociated from sibling embryos and placed on top of an unlabeled DMZ migrating on a fibronectin substrate. Confocal Z-stacks were collected at 1 minute intervals (32 frames). URL: https://movie.biologists.com/video/10.1242/bio.060615/video-7

Movie 8: **Timelapse movie of single DMZ explant on fibronectin with intercalating cell.** Actin (greyscale) was labeled by injection of mRNA encoding LIfeAct-RFP. An intercalating cell is indicated by the yellow arrow. Confocal Z-stacks were collected at 2 minute intervals (17 frames). URL: https://movie.biologists.com/video/10.1242/bio.060615/video-8

FIGURES AND TABLES FOR CHAPTER 2

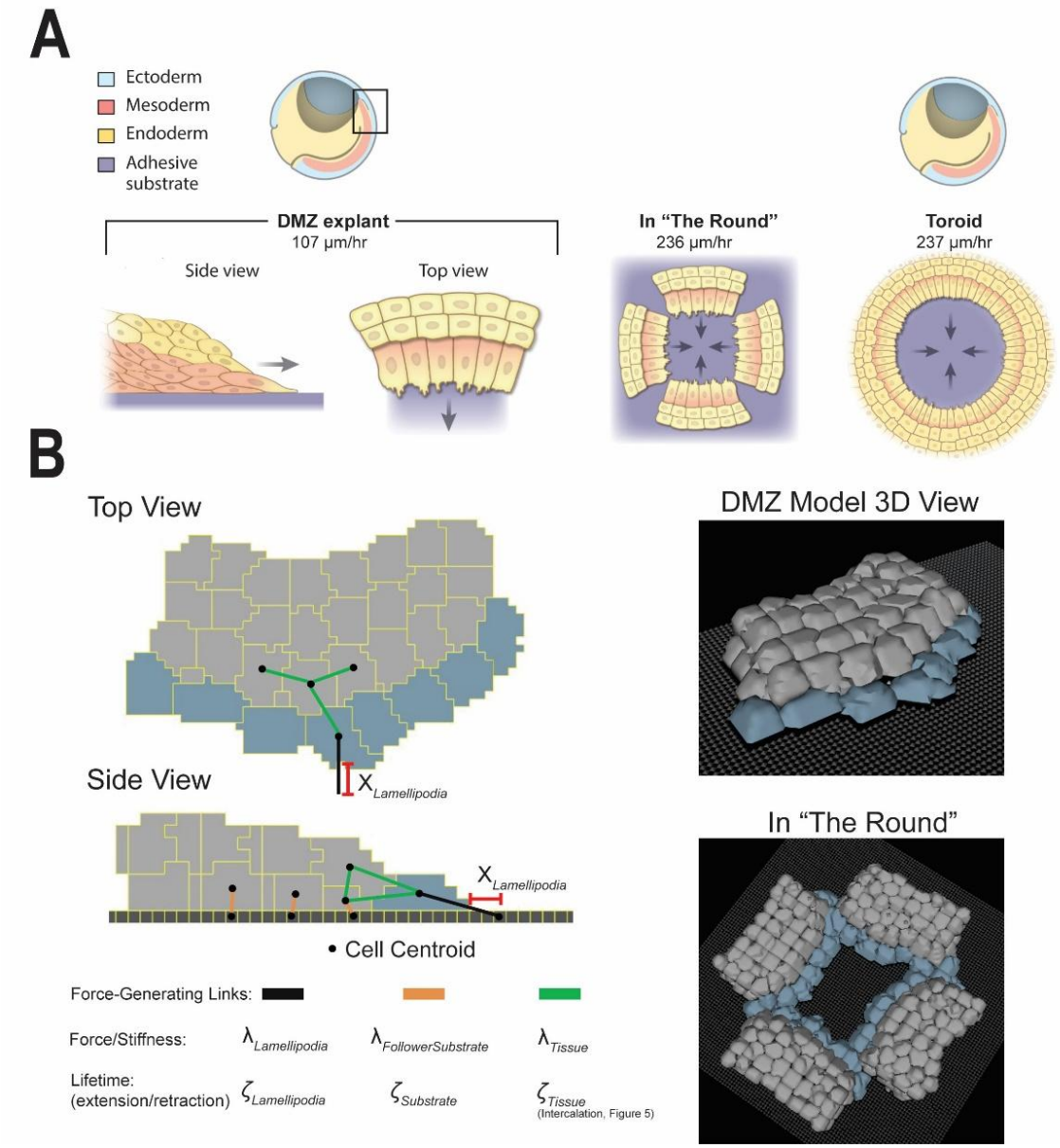

Figure 2- 1 ***Modeling Xenopus Mesendoderm Tissue.*** (A) cartoon of gastrula stage embryos and explants. Hemisected embryo at top, box indicates approximate location of dorsal marginal zone (DMZ) tissue explant dissected from the embryo and placed on an adhesive substrate; side and top views of adherent explant illustrate cellular organization of mesendoderm. Four separate DMZ explants are arranged as shown in order to generate the "In the Round" (ITR) geometry. The ITR approximates a single "toroid" or "donut" explant comprised of the entire mesendodermal mantle. Arrows indicate the

direction of travel of the leading row cells in each preparation. Migration speeds taken from (Davidson et al., 2002) are shown for each explant configuration. (B) Representative DMZ computational model images and schematic of critical parameters are shown. See Methods for the exhaustive parameter table and description of all parameters. Additional figures illustrating Xenopus laevis gastrulation and explant preparation procedures can be found in Sonavane et. al, 2017, and Davidson et. al, 2002(Davidson et al., 2002; Sonavane et al., 2017).

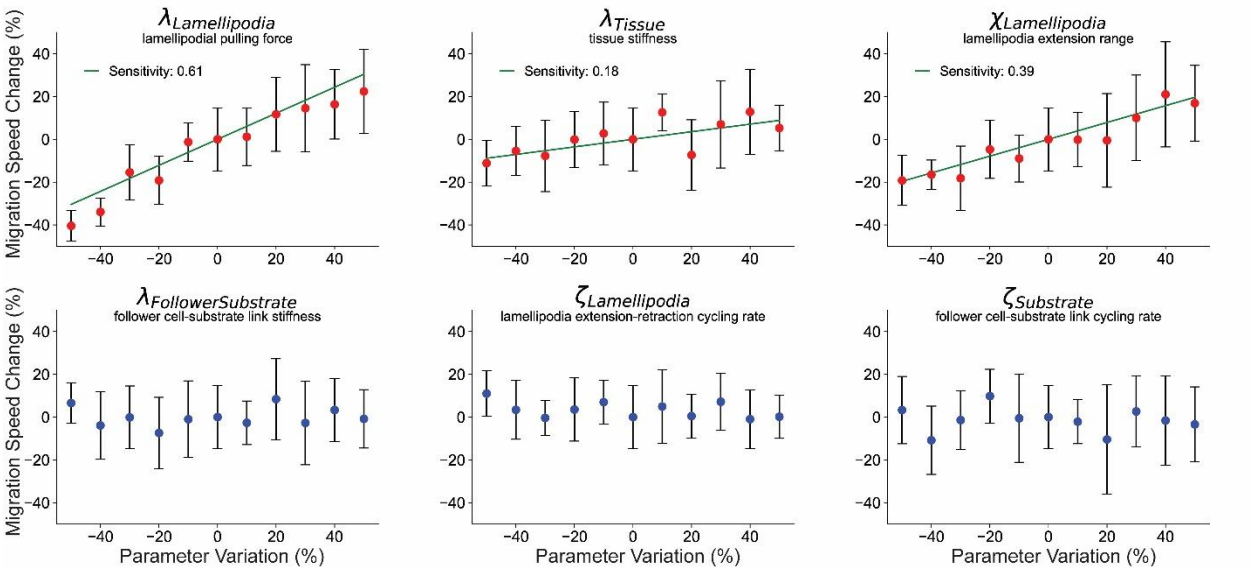

Figure 2- 2 Leading edge parameters drive migration speed of the DMZ explant. 1-Dimensional sensitivity analysis of selected key parameters responsible for the migratory behavior of the explant: ($l_{Lamellipodia}$) Lamellipodial pulling force, (l_{Tissue}) tissue stiffness, ($\chi_{Lamellipodia}$) lamellipodial extension distance, ($l_{FollowerSubstrate}$) follower cell-substrate attachment stiffness, ($\zeta_{Lamellipodia}$) lamellipodial extension-retraction rate, and ($\zeta_{Substrate}$) follower cell-substrate attachment cycling rate. Parameter values ranged from -50% to +50% from baseline by equation reference +/- %*reference, n=10, markers show mean +/- s.d. Red markers indicate $p<0.05$ by one-way ANOVA. Sensitivity given as slope of linear regression line (green) through parameters identified as significant via one-way ANOVA. See Methods for additional parameter details.

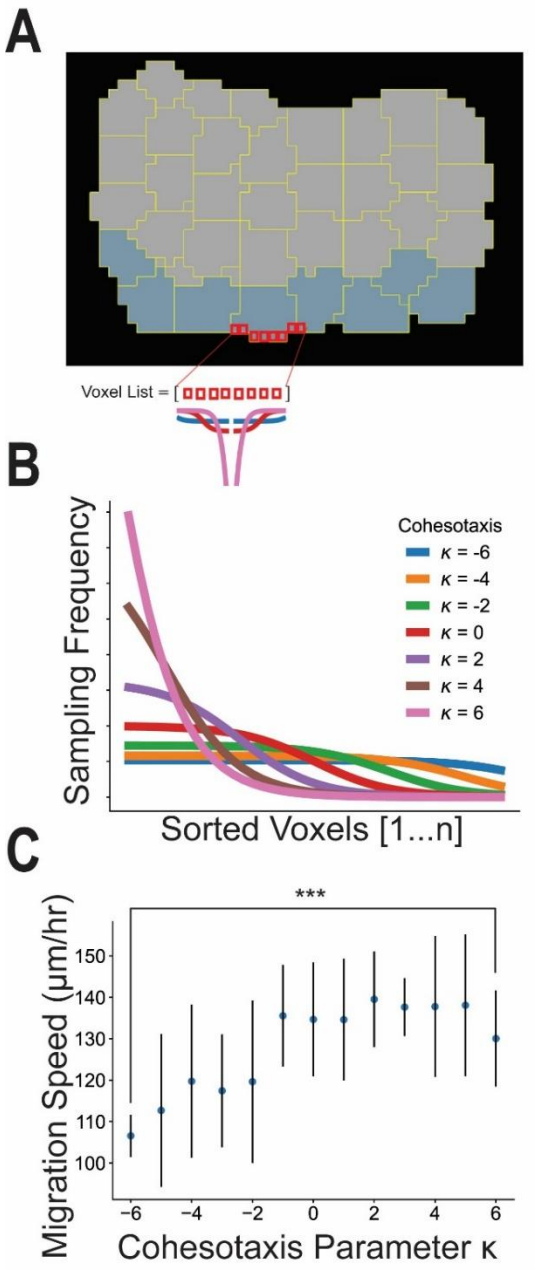

Figure 2- 3 Cohesotaxis increases the speed of migration. Cohesotaxis representation as a directional migratory bias for convex cells. (A) Preferential selection of voxels to establish a persistent direction of migration is described. (B) Probability of selecting from the sorted list of free voxels to produce the bias described in (A) and derived in Methods. (C) Measure of migration speed for different values of cohesotaxis parameter κ applied (n=10 per κ value, *** denotes significance at $p<0.001$ by independent samples t-test)

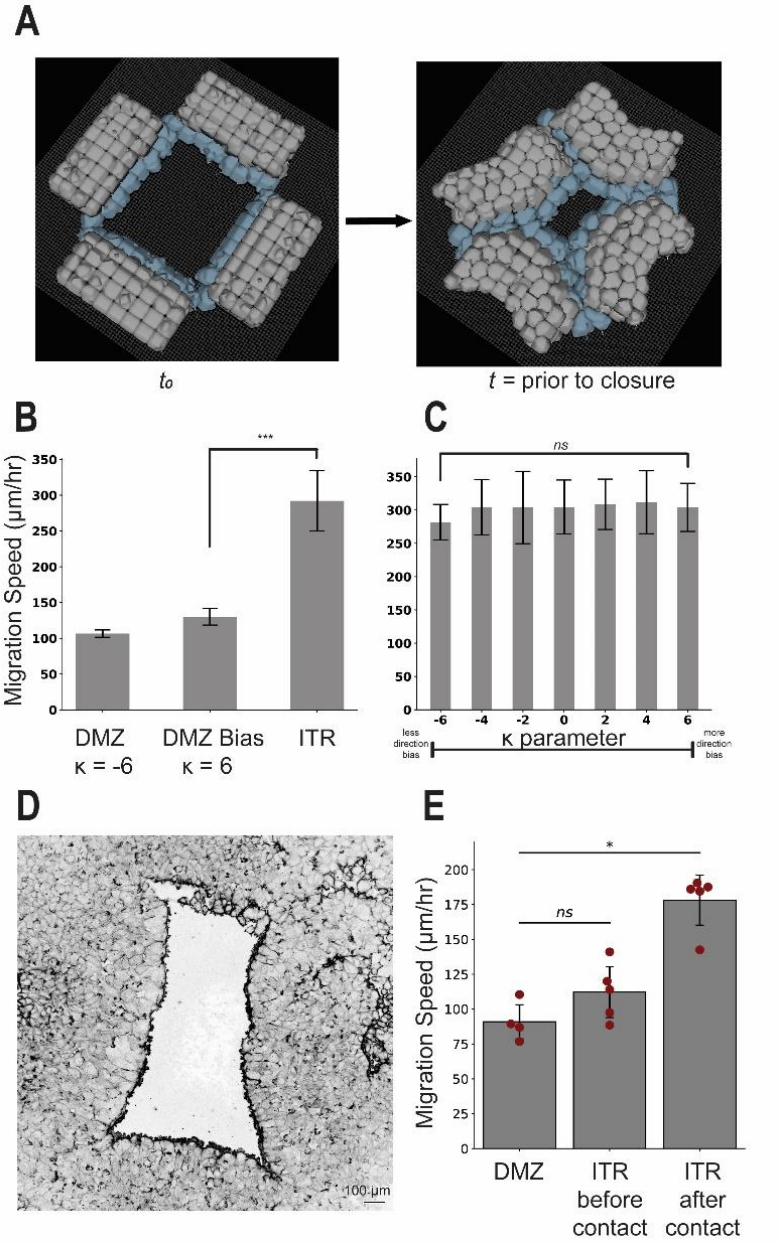

Figure 2- 4 "In The Round" Geometry increases migration speed of the DMZ explant. In The Round experiment configuration. (A) Representative images displaying model initialization at t_0 and time to closure. (B) Migration speed comparison with the DMZ explant with and without bias (K = -6,6), *** indicates $p<0.001$ by independent samples t-test. (C) Effects of modulating the cohesotaxis parameter upon tissue migration speed in the ITR configuration, ns indicates $p>0.05$ by one-way ANOVA.

Simulations results in (B) and (C) include n=10, mean+/- s.d.(D) Representative image from a biological ITR experiment, before time to closure. (E) Experiments comparing migration speed of a single linear DMZ explant and the explants in an ITR configuration before and after collision as performed in Davidson et. al, 2002(Davidson et al., 2002), n=4 for the DMZ, n=5 for the ITR groups, mean +/- s.d., significance at $p<0.05$ by independent samples t-test.

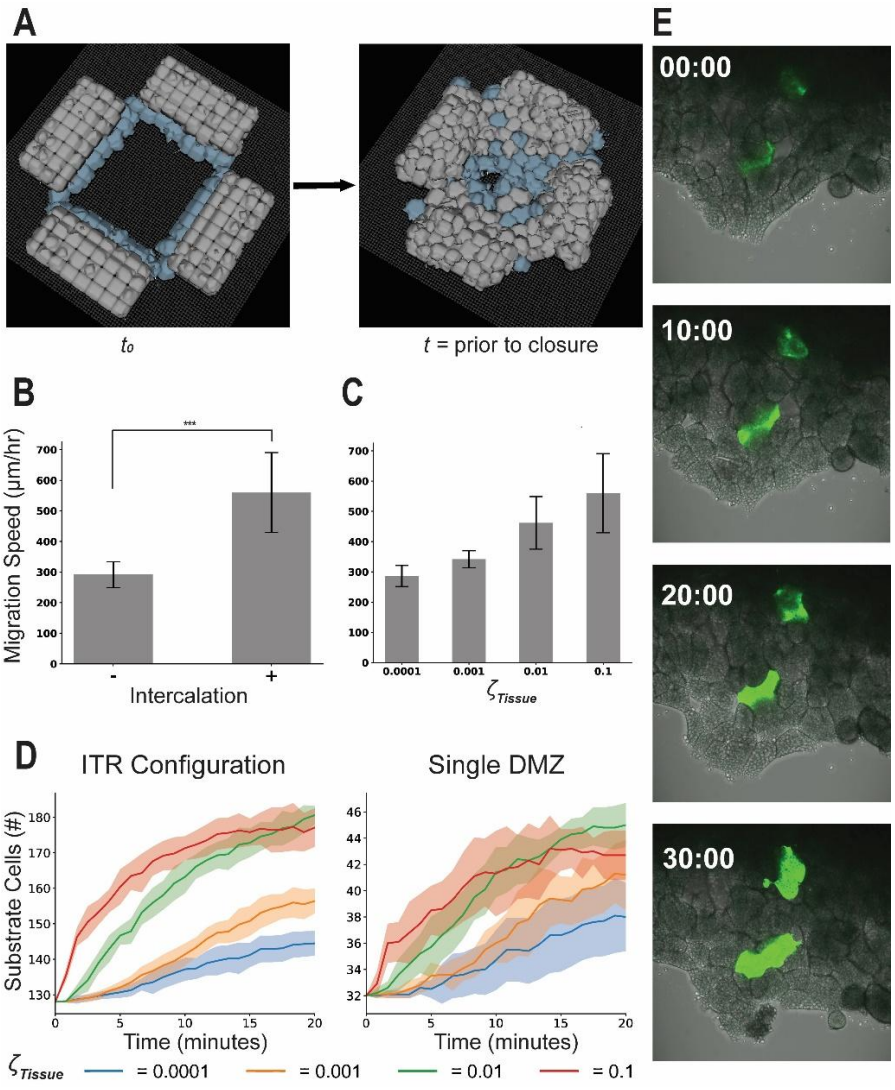

Figure 2- 5 Top-down Intercalation increases migration speed in the DMZ explant. (A) Representative image of the ITR experiment after addition of rules to allow for passive intercalation. (B) Comparison of migration speed of closure with and without the addition of passive intercalation (n=10, mean +/- s.d., *** denotes significance at $p<0.001$ by independent samples t-test), and (C) migration speed measurements with different probabilities of cell-cell rearrangement per timestep, which correspond with likelihood of observed cell intercalation n=10, mean+/- s.d., for all parameterizations. Quantified number of cells (mean +/- s.d.) on the substrate throughout a 20 minute simulated time course for all values of ζ_{Tissue} for both the single DMZ and ITR in-silico configurations in (D), n=10 for all parameterizations. (E) Fluorescent dextran labeled mesendoderm cells sprinkled on top of an unlabelled

DMZ explant reveal cell intercalation toward the substrate level over a 30 minute time course confirming model intercalation behavior.

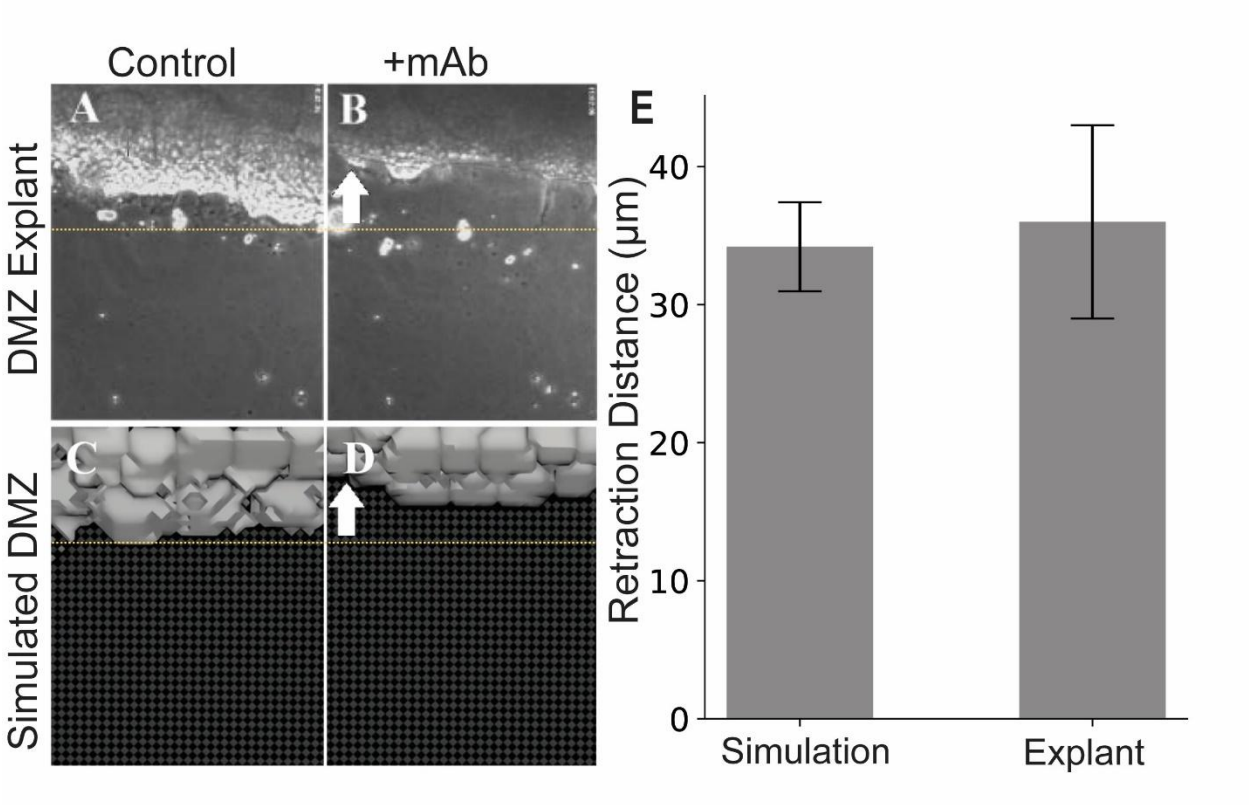

Figure 2- 6 In-silico disruption of cell-substrate binding results in comparable behavior to biological experiments. (A,B) Top-down (*en face*) images from the experiment in (Davidson et al., 2002) (A) before and (B) after disruption of cell-substrate binding following addition of integrin a5b1 function-blocking mAB P8D4. Similar top-down images from a representative simulation (C) before and (D) after disruption of leader cell-substrate binding. White arrows represent the (B) experimentally observed and (D) simulated retraction direction. Yellow dashed lines in panels A-D are included as a visual guide to DMZ retraction limit. (E) Quantitative comparison of measured retraction distances (mean +/- s.e.m) from 10 experiments each are shown. Panels A and B are reproduced from Davidson et al. (2002) with permission from the publisher, Elsevier.

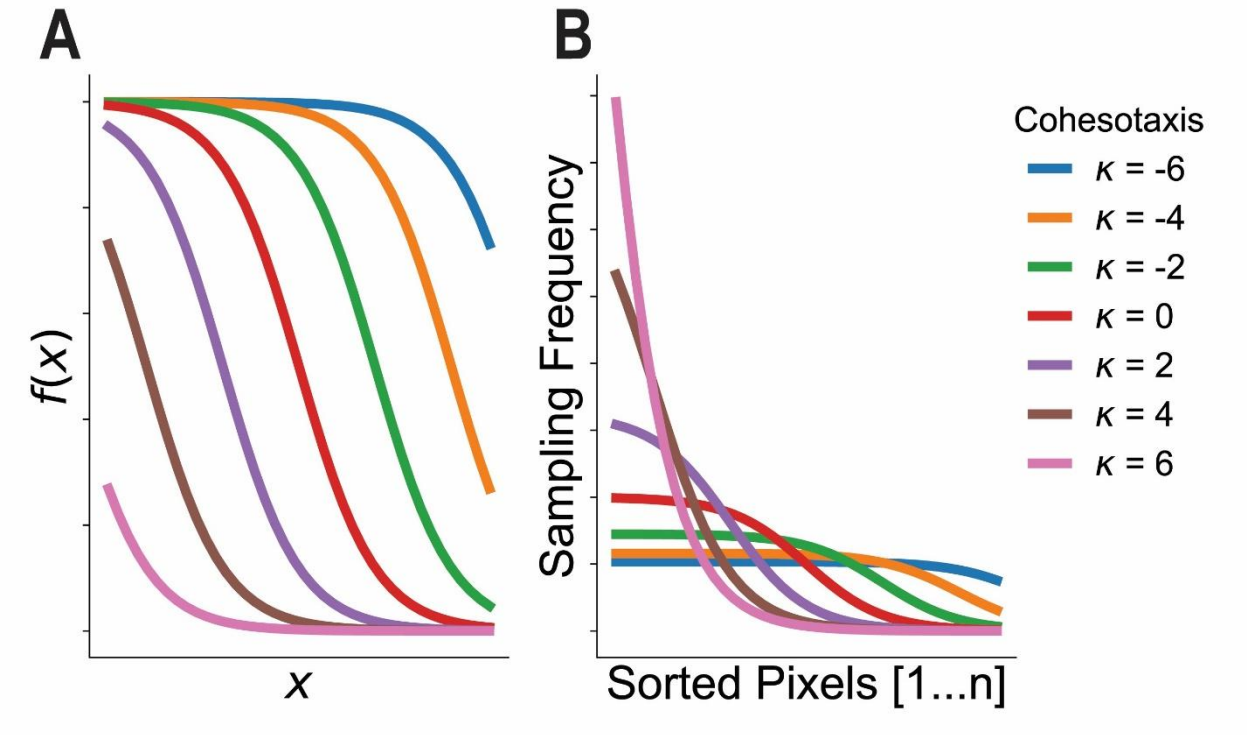

Figure 2- 7 Development of the cohesotaxis voxel selection probability function. . (A) Plotted Sigmoid functions from equation [4]. (B) Sorted voxels are selected to establish migratory bias by sampling with frequency defined by normalized sigmoid functions in (B).

Table 2 DMZ Explant Parameters

Parameter Name	Parameter Description	Parameter Value	Justification
Leader cell agent specific parameters			
$\lambda_{Lamellipodia}$	Force exerted by a link object on a leading edge cell to create a lamellipodium	800	Chosen to reproduce video data of cell migratory behavior
$\chi_{Lamellipodia}$	Distance from the edge of a cell that a link is formed to create a new lamellipodium	12 μm	Chosen to reproduce video data of lamellipodial extension
LLMaxDist	Maximum distance a lamellipodial link object may occupy	90 μm	Chosen to prevent lamellipodial link objects from breaking during the simulation due to exceeding a maximum length
$\zeta_{\text{Lamellipodia}}$	Poisson parameter ζ representing Lamellipodial cycling events occurring per timestep	5/72	Chosen to reproduce video data of leader cell lamellipodial extension/retraction
Follower cell agent specific parameters			
$\lambda_{FollowerSubstrate}$	Stiffness of a Hookean elastic link between follower cells and their substrate, units of force per distance	10	Chosen to reproduce video data of follower cell migratory behavior
$L_{FollowerSubstrate}$	Target distance of a cell-substrate elastic link object	6 μm	Chosen to recreate elastic cell-substrate attachment behavior and reproduce video data
SLinkMaxDist	Maximum distance a follower cell-substrate link object may occupy	30 μm	Chosen to reproduce video data of follower cell migratory behavior
$\zeta_{\text{Substrate}}$	Poisson parameter ζ representing follower cell-substrate events occurring per timestep	1/72	Chosen to reproduce video data of follower cell lamellipodial extension/retraction
Cell-Cell adhesion parameters			
λ_{Tissue}	Stiffness of a Hookean elastic link between cells within the tissue, units of force per distance	600	Chosen to reproduce video data of collective cell migration in the DMZ explant

L_{Tissue}	Target distance of a cell-cell elastic link object	30 μm	Selected to maintain cell-cell adhesion between cells
Tmax_distance	Maximum distance a follower cell-substrate link object may occupy before breaking	90 μm	Selected to maintain cell-cell adhesion during explant migration
ζ_{Tissue}	Poisson parameter ζ representing cell-cell adhesion link cycling events per timestep (For Intercalation ITR model only, Figure 5)	0.001-0.1	Visible passive intercalation behaviors visible at 0.1. Behaviors rare enough at 0.001 as to reproduce closure behavior of the ITR model without intercalation
Parameters for all cell types			
J	Cellular Potts contact energy coefficient	10 for all cell types	Referenced from literature to define uniform contact affinity between agent types(Swat et al., 2012)
λ_{volume}	Cellular Potts volume constraint	1 for all cell types	Chosen to allow cell deformation during explant migration in the CPM framework
V_{target}	Target volume for all explant cells in the CPM framework	27,000 μm^3	Chosen to allow cells to occupy 5x5x5 voxels in volume
$\mathcal{H}^*$	Temperature parameter for the CPM simulation	10	Chosen as a default as referenced from literature(Swat et al., 2012)

CHAPTER 3: Multicellular Cellular-Potts and Vertex models of tissue surface tension in explants of the *Xenopus laevis* gastrula

The text in this chapter is in preparation for submission as part of a larger manuscript on the role of fibronectin in modulating tissue surface tension in the *Xenopus laevis* gastrula

ABSTRACT

Many processes in developmental biology have been explained by the fluid-like nature of tissues to adopt a surface tension. Tissue sorting, spreading, and migration during embryogenesis have all been described to arise due to the surface tension of constituent tissues within the developing embryo. The *Xenopus laevis* gastrula is one model system where these behaviors have been investigated and documented. Current explants of the gastrula stage *Xenopus laevis* embryo exhibit multiple dramatic, spontaneous, tissue-reorganization behaviors when excised from the intact embryo. The ectodermal blastocoel roof rapidly curls when isolated from the embryo, and the remainder of the embryo exhibits an eversion or flowering behavior. Migratory mesoderm and endoderm tissue contracts in the absence of cellular crawling processes. In this work, we develop multiple Cellular-Potts and vertex computational models to investigate the potential for tissue surface tension to provide an appropriate driving force to produce these behaviors. We find that tissue surface tension alone, expressed through differential adhesion of cells and tissues as well as cortical tension of individual cells, can replicate observed tissue reorganization.

INTRODUCTION

The behavior of tissues as liquids with an intrinsic surface tension has been observed in many biological processes. This surface tension has, in part, explained observed self-organization of tissues and organs in multiple developmental systems(Foty and Steinberg, 2013) and the invasive tendency of carcinomas and sarcomas(Foty and Steinberg, 1997; Foty et al., 1998; Hegedüs et al., 2006). In developmental systems, surface tension is a mechanism behind the sorting, spreading, and migration of different populations of tissues during gastrulation(Davis et al., 1997; Schötz et al., 2008). The original observations by Townes and Holtfreter found that dissociated gastrula-stage cells dissociated from mesoderm, endoderm, and ectoderm aggregate and sort based on differential adhesivity of cells to cells of the same type compared to cells of other tissue types(Townes and Holtfreter, 1955). This behavior has been confirmed to depend on differential adhesivity *in silico* using the Cellular-Potts modeling method by Graner and Glazier (Graner and Glazier, 1992; Zhang et al., 2011).

Tissue surface tension (TST) arises due to adhesion of cells to one another, and the contractility of each cell's cortical cytoskeleton. The adhesion component is termed the differential adhesion hypothesis, which describes a fluid-like surface tension that arises in tissues as a result of varying adhesivity of cells to each other through changes in the expression, binding activity, and/or specificity, of cell-cell adhesion molecules (e.g., cadherins). The contractility of actin and myosin proteins in the thin cytoskeletal layer that underlies each cell's membrane also contributes to the surface tension of a tissue(Manning et al., 2010). During embryogenesis, changes in surface tension promote multiple tissue movements that organize tissues to ensure the proper development of the embryo. During gastrulation in particular, multiple collective cell migration movements occur, some of which have been explained by the actions of tissue surface tension. Radial intercalation events of cells that allow for spreading and migration of mesoderm and endoderm tissues towards the animal pole of embryo has been described as a surface tension driven process(Marsden and DeSimone, 2001; Shook et al., 2018). During the process of epiboly, the outer ectodermal tissue of the blastocoel roof in *Xenopus laevis* or blastoderm in Zebrafish, thins and spreads from the animal pole (or the 'north' pole, or the top of the embryo) to the vegetal pole (the 'south'

pole or bottom of the embryo) due in part to a gradient of cortical tension that arises in this tissue(Hernández-Vega et al., 2017; Marsden and DeSimone, 2001). The blastopore of the *Xenopus laevis* embryo is driven to a close in part by forces generated in converging and thickening tissue that arises due to the surface tension of the tissues(Shook et al., 2018; Shook et al., 2022).

These movements are studied using explant preparations excised from the developing *laevis* embryo at different stages. These include the dorsal marginal zone explant and the toroidal explant used to study migratory mesendoderm(Comlekoglu et al., 2024; Davidson et al., 2002; Sonavane et al., 2017), and the giant sandwich explant used to study convergent thickening behaviors towards the vegetal pole of the *Xenopus laevis* embryo(Shook et al., 2018; Shook et al., 2022). However, the act of removing the tissue from its native environment *in situ* results in altered cellular and tissue organization and behavior not easily observed in live or fixed and sectioned embryos. Computational modeling efforts have been effective in assisting in the investigation of these phenomena of tissue organization that have proven difficult to study through wet lab experimentation alone(Comlekoglu et al., 2024). Both Cellular-Potts and vertex model formalisms have been applied to study the effects of both differential adhesion and cellular cortical tension and therefore are an ideal choice to model the influence of surface tension on observed explanted tissue movements(Alt et al., 2017; Comlekoglu et al., 2024; Manning et al., 2010; Osborne et al., 2017; Sego et al., 2023a; Swat et al., 2012).

Prior investigation into the toroidal explant of mesendoderm revealed that the leading edge migrates to a close even in the absence of cell-substrate adhesion, and cellular crawling(Sonavane et al., 2017). When first explanted and plated on a bovine serum albumin (BSA) coated plate to prevent adhesion, the explant can be observed to “roll” outward prior to closing in the absence of cell crawling on fibronectin assembled by the blastocoel roof. This rolling behavior can be observed as an eversion or “flowering” when the blastocoel roof is removed from the embryo but the mesendoderm is left intact. The excised blastocoel roof also curls rapidly when removed from the embryo. In the intact embryo these bulk tissue movements are constrained by the spherical geometry of the embryo. In this work, I hypothesize that

these observed explant behaviors are the result of alterations in tissue surface tension due to excision and removal of the tissue from its native geometry and extracellular matrix *in situ*. I explore the potential for surface tension and tissue geometry to promote these behaviors in a computational framework through the development and exploration of Cellular-Potts and vertex models. This hypothesis is motivated by current, unpublished observations by staff scientists Bette Dzamba and Dave Shook in the DeSimone lab who have observed a rapid loss of fibronectin along the deep cells of the blastocoel roof (the cells that face the inside of the embryo). We expect that this loss of fibronectin post-explantation results in concomitant loss of fibronectin-integrin signaling. We expect this loss of signaling to result in an increased actomyosin-mediated contractility of the cortical cytoskeleton of mesendoderm cells, thus increasing the tissue surface tension of tissue *ex vivo*.

RESULTS

TST drives curling behaviors in the Blastocoel Roof

The ectodermal blastocoel roof at stage 11.5 rapidly and spontaneously curls when explanted from the embryo. The explant consistently curls towards the vegetal-facing surface of the roof, or away from the superficial layer of cells of the blastocoel roof over a relatively short time scale of 20 minutes (Figure 3-1A). We expect the surface tension of the cells along this face, also known as the deep cells of the roof, to increase, either because of the tissue's new exposure to the media outside the embryo, or because of the tissue's separation from endogenous mediators of tissue surface tension such as the fibrillar fibronectin-rich extracellular matrix that exists along the blastocoel roof in the *in vivo* embryo. We therefore expect the increase in surface tension to result in a contraction of the surface of deep cells of the explant resulting in a decreased surface area of that face, and a concomitant curling of the bulk tissue of the explant.

To investigate the potential for tissue surface tension to result in this curling, we construct representative geometry of a sagittal cross-section of the multi-layered tissue explant as a vertex model that curls over the course of 50 simulated timesteps (Figure 3-1B). We model the contraction of the surface of deep ectoderm cells of the explant as a contractile line tension of the edges that correspond to the deep surface of cells (highlighted in red, Figure 3-1B, see Methods for details of the numerical implementation). We quantify the curling behavior of the computational model of the explant at different degrees of edge contractility by tracking both the radius of curvature of the deep cells of the explant and the end-to-end length of the explant (black circles in Figure 1B) to find that decreased contractility of the deep face corresponds to slower curling, and lesser degrees of curling with low enough contractility (Figure 3-1C). In this manner, we demonstrate how tissue surface tension is sufficient to produce the curling behavior of the blastocoel roof explant because the only mechanism for movement or deformation of the *in silico* explant is tissue surface tension.

Tissue surface tension drives tissue eversion or "flowering" of mesendoderm tissue in the roof-less embryo

After removal of the blastocoel roof, the remainder of the embryo (termed the roof-less explant) exhibits an eversion or "flowering" phenotype driven by movements of the mesendoderm tissue oriented near the animal pole of the embryo (Figure 3-2). This mesendoderm tissue is newly exposed to media just like the surface of the deep cells of the blastocoel roof explant. Similar to our investigation of the blastocoel roof explant, we hypothesize that the sudden exposure of the mesendoderm to media following roof-less explant creation results in an increase in the tissue surface tension of this newly exposed surface. We proceed to investigate the potential for tissue surface tension to produce these movements in both Cellular-Potts and vertex models of representative geometry of the roof-less explant.

The everting mesendoderm of the roof-less explant at stage 11.5 will have sorted roughly into distinct layers of endoderm and mesoderm consistent with the appearance of a roofless explant *ex vivo*. Endoderm makes up the inner cell mass of the migratory mesendoderm, and the mesoderm makes up the outer cell mass normally in contact with the blastocoel roof. As previously discussed, tissue surface tension is a function of differential adhesion and cortical tension. Cellular-Potts (CPM) can model tissue surface tension that arises from differential adhesion among multiple cell types in a three-dimensional context. We construct a representative cup-like geometry of the roof-less mesendoderm in the CPM framework with both mesoderm and endoderm cells. In this model, eversion behavior is similar to that observed in the biological explant (Figure 3-3A).

After tuning parameters to allow for eversion, we perform a parameter exploration to represent increasing or decreasing the effect of surface tension. We perform this by altering the adhesion energies governing the interfacial tensions of mesoderm and endoderm, mesoderm and media, and endoderm and media. We report representative simulation states at MCS=500 after positively and negatively incrementing the parameter governing the adhesion energy associated with each cell-cell and cell-media interface by 2 to illustrate how eversion may differ with alterations in interfacial tension (Figure 3-3B).

Quantified interface areas of mesoderm and media and endoderm and media for n=10 replicates for each area of the parameter space are reported in Figure 3-3C. In all explored areas of the parameter space, interface area between mesoderm and media decreases and the interface area between endoderm and media increases to allow for eversion of the model. This suggests that contraction of the mesoderm and expansion of the endoderm results in eversion driven by tissue surface tension as hypothesized. When adhesion energy associated with the mesoderm-endoderm interface is low ($J_{mesoderm,endoderm} = 5$), contraction of the exposed mesodermal surface occurs through intercalation into the endodermal cell mass. When $J_{endoderm,medium}$ is low ($J_{endoderm,medium} = 6$), eversion occurs through expansion of the endoderm over the mesoderm.

The CPM model of eversion represents tissue surface tension purely through differential adhesion between cell types and the media. Tissue surface tension can also be explained through cortical tension of cells, and this view of tissue surface tension is able to be represented through the use of the vertex model methodology. We have therefore created a vertex model of representative roof-less explant geometry and model the surface-tension mediated contraction of the mesoderm-medium interface as an edge contractility. The strength of the contractility is a tunable parameter to allow us to observe how explant shape changes over simulated time as contractility increases or decreases, which corresponds to increased or decreased tissue surface tension. A representative simulation time course is displayed in Figure 3-4A. As contractility increases, both the left and right edges of the simulated explant (highlighted in red in Figure 3-4A) curl and the radius of curvature at these areas decrease over time. We observe an increased degree of eversion with greater contractility (Figure 3-4B). Simulation configurations at a consistent simulation time of t=40 for different strengths of contractility are shown in Figure 3-4C, where increased contractility (corresponding to increased tissue surface tension) allows for a more dramatic eversion.

Mesendoderm mantle closure in the absence of crawling, tissue surface tension in the toroidal explant

Migratory mesendoderm can be removed from the remainder of the embryo to create a toroidal shaped tissue explant with an intact migratory leading edge. This explant is commonly used to investigate

the migratory behaviors of the tissue on various substrates. However, when the tissue explant is prevented from adhering to a substrate, the leading edge still converges resulting in the closing of the inner free area of the toroidal shaped tissue in the absence of cell crawling. This suggests that an additional mechanism for cell migration may contribute to migration of this tissue when explanted, and this mechanism may be active *in vivo* as well. Given that surface tension explains the dramatic tissue deformation and reorganization that results in eversion of this same mesendoderm tissue in the roof-less explant, we may expect that tissue surface tension could be a contributing mechanism to toroidal closure in the absence of crawling. To this end, we constructed a toroidal explant *in silico* using the CPM method to investigate whether tissue surface tension alone may allow for convergence or closure of a toroidal tissue geometry.

Biological toroidal explants converge over a 1 hour and 20 minute time course (Figure 3-5A). We replicate a toroidal shaped geometry *in silico* that similarly converges over the time course of a simulation (Figure 3-5B). In this model, the only mechanism driving cell motility and resulting tissue reorganization is differential adhesion of cells to each other and exposure to the media. Increasing surface tension in this manner results in more rapid convergence, and decreasing surface tension below the value of 5.5 prevents closure entirely (Figure 3-5C,D). Our model suggests that tissue surface tension alone is sufficient to reproduce the toroidal convergence behavior observed in the corresponding biological explant.

DISCUSSION

In this work, I investigate whether it is possible for mechanisms of tissue surface tension to produce the dramatic tissue self-reorganization behaviors we observe from explanted *Xenopus laevis* gastrula stage tissues. I find that with representative geometry reconstructed *in silico* and the computational models driven only by hypothesized mechanisms of tissue surface tension, I can generally recapitulate the tissue self-organization behaviors of the explants.

Beginning with the blastocoel roof explant consisting of ectoderm tissue removed from the embryo, we observe a dramatic curling effect over the relatively short timescale of 20 minutes. This curling was hypothesized to be due to an increase in surface tension of the tissue face that was facing towards the blastocoel cavity of the embryo *in situ* and is newly exposed to the media when explanted. The increase in surface tension of that face would be expected to result in a decrease in cell surface are exposed to the medium while cell-cell adhesion is maintained. Our model recapitulates this, and further demonstrates that an increased contractility, analogous to an increased degree of hypothesized surface tension, results in an increased amount of curvature given the same amount of simulation time. Our simulation suggests that decreasing tissue surface tension would be expected to slow the curling of this explant. Preliminary experimental data (unpublished) generated by the DeSimone lab confirms this prediction. Adding soluble plasma fibronectin, which is normally present in abundance in the blastocoel cavity along the contractile face *in vivo* slows explant curling behavior. Similar behavior is observed in explants in reduced Ca++ and Mg++ media.

The toroidal explant represents mesendoderm tissue isolated from the ectodermal blastocoel roof and the remainder of the embryo. In this explant, we observe migratory behavior of the leading edge of a toroidal explant in the absence of cell crawling. We recapitulate toroid closure in our Cellular-Potts toroid model, where cell motility is driven only by tissue surface tension created through differential adhesion between cells and the media. This suggests that tissue surface tension may be a potential driving force for these tissue movements. Just as we observed with the blastocoel roof explant computational simulation,

decreasing surface tension slowed toroid closure. These findings confirm that surface tension alone may result in toroid closure.

Finally, we find with both Cellular-Potts and vertex model formalisms that tissue surface tension may produce the flowering or eversion behavior observed in the roof-less explant. Producing a comparable finding with two model formalisms is rigorous and supportive of our conclusion that tissue surface tension may be sufficient to produce eversion and therefore could be a likely mechanism biologically to cause eversion of biological explants. Both Vertex and Cellular-Potts models demonstrated eversion through tissue surface tension. In both models, eversion resulted from decreasing the area of the cell-medium interface of mesoderm tissue. Exploration of the Cellular-Potts model suggested that this could occur through either intercalation behaviors of mesoderm into endoderm to result in the reduction of the cell-medium interface, or through expansion of the endoderm over the mesoderm. Thus the vertex model similarly predicted expansion of the endoderm over the mesoderm to reduce the area of the mesoderm-medium contact interface.

Existing studies of migratory mesendoderm tissue do not currently consider tissue surface tension to be an important factor influencing the behaviors of the explants *ex vivo*(Davidson et al., 2002; Sonavane et al., 2017). Surface tension alone is a driving force capable of resulting closure of the toroid explant. We would expect the increase in surface tension of the tissue after removal from the *in vivo* environment to increase the rate of mesendoderm toroid closure possibly by contributing to crawling-mediated migration. Prior work observed that the mesendoderm leading edge in the toroidal tissue migrates more quickly than in planar tissue geometries(Comlekoglu et al., 2024; Davidson et al., 2002). This was thought to be due in part to radial intercalation behaviors observed in the tissue explants. Cellular intercalation behaviors may themselves be the result of the surface tension of the tissue as suggested by the areas of the parameter space where mesoderm intercalated into the endoderm to result in the eversion behavior.

It is unclear the extent to which these behaviors exist *in vivo.* Blastocoel roof curling, mesendoderm toroidal closure, and roofless explant eversion occur only when the tissue is removed from the *in vivo* environment. This could be because the environment within the gastrula may contain factors that result in decreased tissue surface tension of the tissue such as fibronectin, or that the spherical geometry of the embryo constrains the tissue such that these movements cannot occur. Recent work by S.F. Gabriel Krens et. al(Krens et al., 2017) demonstrate within the Zebrafish gastrula that osmolarity of the tissue interstitial fluid of the *in vivo* embryo influences tissue surface tension *in vivo*, and that media used for cell culture differs from that of the interstitial fluid thus resulting in differential tissue surface tension in explanted tissues. Additionally, the cell-matrix or cell-cell interface of the blastocoel roof that mesendoderm tissue migrate along in the *Xenopus* gastrula may permit a lower tension interface that contributes to spreading by epiboly compared to a higher tension cell-medium interface as suggested by a recent review(Wu et al., 2023). While examples of this in Xenopus are difficult to find, preferential cell-matrix adhesion as compared to cell-cell adhesion has been observed to drive budding and branching morphogenesis of epithelial tissue in the murine embryonic salivary gland(Wang et al., 2021). Explantation of the tissue would result in the absence of this matrix and subsequent exposure to media. This new cell-media interface would be expected to have a different interfacial tension than the cell-matrix interface. Thus, this difference in interfacial tension would be expected to drive tissue organization behaviors that do not occur *in vivo*. Ongoing efforts are investigating how components of the ECM may modulate the surface tension of the tissue. Unpublished work by Bette Dzamba and Dave Shook in the DeSimone lab have revealed that the extracellular matrix on the deep cells of the BCR roof rapidly loses fibronectin after removal from the embryo. Both BCR and migratory mesendoderm cells are in contact with this matrix during gastrulation, suggesting that fibronectin may be an effector of tissue surface tension. Further unpublished work demonstrates that knocking down expression of fibronectin in the developing embryo with antisense morpholino results in BCR explants that curl more rapidly, and roof-less explants that evert more rapidly, than those of control embryos. Ongoing and future work are currently investigating how intracellular integrin-fibronectin signaling may increase actomyosin

contractility of the cortical cytoskeleton. Additionally, the DeSimone lab has observed these same explant movements when constraining the tissue under glass cover slips to approximate the constraints of the spherical embryo. All this suggests that the surface tension of the tissue is likely different *ex vivo* compared to *in vivo*.

While my models demonstrate that it is possible for the mechanism of surface tension to produce observed tissue organization behaviors in multiple *Xenopus* gastrula tissue explants, we cannot conclude from this work that tissue surface tension is the only mechanism that explains these behaviors. Our models assume that only the specified mechanisms of surface tension are active to modify the geometry of the tissue. At the stage of development where these tissues are explanted, other tissue organization behaviors, often referred to as morphogenic machines, may drive tissue movements and affect organization of the explanted tissues. At this stage of development, the blastocoel roof thins and spreads in the process termed epiboly(Keller, 1980; Longo et al., 2004; Marsden and DeSimone, 2001). Migratory mesendoderm is influenced by the force-generating events of convergent extension and convergent thickening(Shook et al., 2018), vegetal tissue rotation movements(Winklbauer and Schürfeld, 1999), as well as vertical shearing and vertical telescoping of the mesendoderm towards the leading edge(Nagel et al., 2021). All of these are active processes that occur natively in these tissues and would be expected to be active or modified when explanted and contribute to observed tissue reorganization. Future work is needed to build upon the existing models to explore the addition of these mechanisms and the roles they may play in tissue reorganization of both explanted and *in vivo* tissues.

In conclusion, we have developed and applied computational models that have allowed us to suggest a role for tissue surface tension as a driving force for the native tissue organization of explanted tissues from the *Xenopus laevis* gastrula. These models assist in the ongoing investigation of the role of surface tension and its modulation in tissue morphogenesis.

METHODS

Cellular Potts Models

The *in silico* model representing both the toroidal shaped mesendoderm explant and the roof-less explant were constructed in the Cellular Potts (Glazier-Graner-Hogeweg) model framework (abbreviated CPM) using the open-source simulation environment CompuCell3D(Swat et al., 2012). Individual cells in the CPM framework are represented as a collection of voxels on a regular, three-dimensional lattice and are given properties of predefined volume and contact energy with surrounding cells. These biological properties are represented mathematically in an effective energy functional *H* shown in (1), which is evaluated on a cell-by-cell basis during each computational timestep,

$$H = \sum_{i,j,neighbors} \quad J\left(\tau_{(\sigma(i))}, \tau_{(\sigma(j))}\right)\left(1 - \delta_{\sigma(i),\sigma(j)}\right) + \lambda_{volume}\left(V_{cell} - V_{target}\right)^2 \qquad (1)$$

where the first term models cell contact energy for neighboring cells with a contact coefficient *J* where *i*, *j*, denote neighboring lattice sites, $\sigma(i)$ denotes individual cell ID occupying site i and $\tau(\sigma)$ denotes the type of cell σ in the model.

Units for CPM parameters are given when possible, however exact units for certain parameters in the CPM methodology is often difficult to determine given the method's reliance on statistical minimization of the abstract effective energy functional to reproduce stochastic cellular behaviors. Parameter values for the CPM models are provided in Table 1. Additional contact energy parameters for the CPM model of the roof-less explant are provided in Table 2.

The CPM model recreates cell movement using principles defined in equations 1 by randomly selecting pairs of neighboring voxels (y, y') and evaluating whether one voxel located at y may copy itself to its neighboring pair at y'. This voxel copy attempt, denoted $\sigma(y,t) \rightarrow \sigma(y',t)$, occurs with the probability defined by a Boltzmann acceptance function (equation 2) of the change in the effective energy of the system *H* as defined in equation 1.

$$\Pr\left(\sigma(y,t) \rightarrow \sigma(y',t)\right) = e^{-\max\left\{0,\frac{\Delta\mathcal{H}}{\mathcal{H}\cdot}\right\}} \qquad (2)$$

The CPM temperature parameter $\mathcal{H}^*$ affects likelihood of accepting voxel copy attempt if system effective energy is increased, whereas voxel copy attempts that decrease system effective energy are always accepted. $\Delta\mathcal{H}$ is the change in system effective energy after a voxel copy attempt. Parameters for the CPM models are displayed in Tables 3 and 4.

CPM Model Initialization:

The geometry of the toroidal mesendoderm explant was constructed *in silico* by arranging 756 mesendoderm cells in an approximately toroidal shape within a 120x120x35 voxel simulation domain. The computational reconstruction of the explant was placed on a substrate made of 1x1x1 voxels across the bottom of the simulation domain. The substrate voxels were frozen and contact energy parameters between cell and medium and cell and substrate were set to be equivalent, making them effectively the same as medium in the simulation. Substrate voxels were created for the purpose of reporting the closure dynamics of the mesendoderm explant over the course of the simulation.

The geometry of the roof-less explant was constructed *in silico* by arranging 257 mesendoderm cells in a cup-like formation to approximate the geometry of the exposed mesendoderm tissue after creation of the biological explant. Of the 257 cells, the inner 115 cells were assigned to be endoderm cells with the rest assigned to be mesoderm cells.

Modeling Surface Tension in the CPM formalism:

Surface tension in the CPM model formalism is described by equation 3 below(Belmonte et al., 2016; Glazier and Graner, 1993):

$$\gamma = J_{c,m} - J_{c,c}/2 \quad (3)$$

Where γ is surface tension, and the two different *J* parameters are the contact energies associated with the interface between two different cell types or with the media. For example, in the CPM model of toroidal closure, $J_{c,m}$ is the contact energy between mesendoderm cells in the simulation domain and the medium or substrate that surrounds the mesendoderm cells, and $J_{c,c}$ is the contact energy between mesendoderm

cells in the simulation domain. Given that the only mechanism for motility in the CPM models as specified is contact energy, all cellular movements observed by the model can be attributed to differential-adhesion driven surface tension.

Measuring closure dynamics

The toroidal geometry in the CPM model was allowed to close driven by differential adhesion dynamics applied by the CPM algorithm. Toroidal free area was measured by counting the number of substrate voxels that were located within the free area of the toroid explant and were not in contact with mesendoderm cells. The free area of the toroid was approximated as a which is valid due to the circular geometry of the toroid. Thus, the radius of the free area could be calculated as $\sqrt{\frac{Free\ Area}{\pi}}$ and reported over the time course of the simulation. *In silico* toroidal explants were considered closed when the toroid free area was less than 60 voxels, or less than 3 cells in inner free area.

Vertex Models

The *in silico* models representing the BCR explant and the roof-less explant were built in the vertex model formalism using the open-source software Tissue Forge(Sego et al., 2023b). In these vertex models, cells are represented by hexagonal surfaces that move and deform based on forces directed upon their constituent vertices. Vertex positions ($r_i(V)$) are updated per unit time ($\frac{dr_i(V)}{dt}$) in accordance with overdamped dynamics, where a total force $f_i^V(V)$ acts vertex (V) with a drag coefficient for that vertex of $M^V(V)$ as described in equation 4 below:

$$f_i^V(V) = M^V(V) * \frac{dr_i(V)}{dt} \quad (4)$$

Each cell's mechanical properties can be expressed as an effective energy functional described in equation 5 below:

$$H(S) = \lambda^{area}(A^S(S) - A^o)^2 + \lambda^{tension}\Sigma_{<i,j>}\left(l_{ij} - l_{ij}^0\right)^2 \quad (5)$$

This energy functional consists of an area constraint and an edge tension. For the area constraint, $A^S(S)$ is the area of a hexagonal cell, A^o is the target or preferred area of a cell, λ^{area} is the strength of the area constraint. For the tension of edges not explicitly set to be contractile for *in silico* experiments, the $\lambda^{tension}$ represents the strength of the edge tension, l_{ij} is the length of vertices *i* and *j*, and l_{ij}^0 is the target or preferred length of vertices *i* and *j*. For contracting edges representing surface tension mediated contraction of the specified area of the tissue, the edge tension is instead given by the contribution to the energy functional described in equation 6:

$$\lambda^{contractility} \Sigma_{<i,j>} \left(l_{ij}\right)^2 \quad (6)$$

Which produces a constant, length-independent tension along the specified edges. Model parameters are specified in Table 5.

Vertex model geometry construction and initialization

The vertex model geometries were specified in the open-source computer graphics software Blender 3d(blender.org - Home of the Blender project - Free and Open 3D Creation Software). Vertex model mesh objects consisting of vertices, edges, and faces in 3D space were exported as the standard Wavefront OBJ (.obj) files and imported into tissue forge for simulation. Vertices in the .obj mesh file were assigned to be vertices in the vertex models, and faces in the .obj mesh file were assigned to be surfaces representing cells in the vertex model.

Quantifying eversion and curling

The BCR end-end length was calculated as the Euclidean distance between the vertices at the ends of the contractile edges as circled in Figure 3-1B. Radius of curvature for both BCR and roof-less explant vertex models was quantified by performing a least squares fit of a circle through the centroids of the cells attached to the contractile edges. The radius of the circle corresponded to the radius of curvature of the contractile boundary of the vertex model.

FIGURES AND TABLES FOR CHAPTER 3

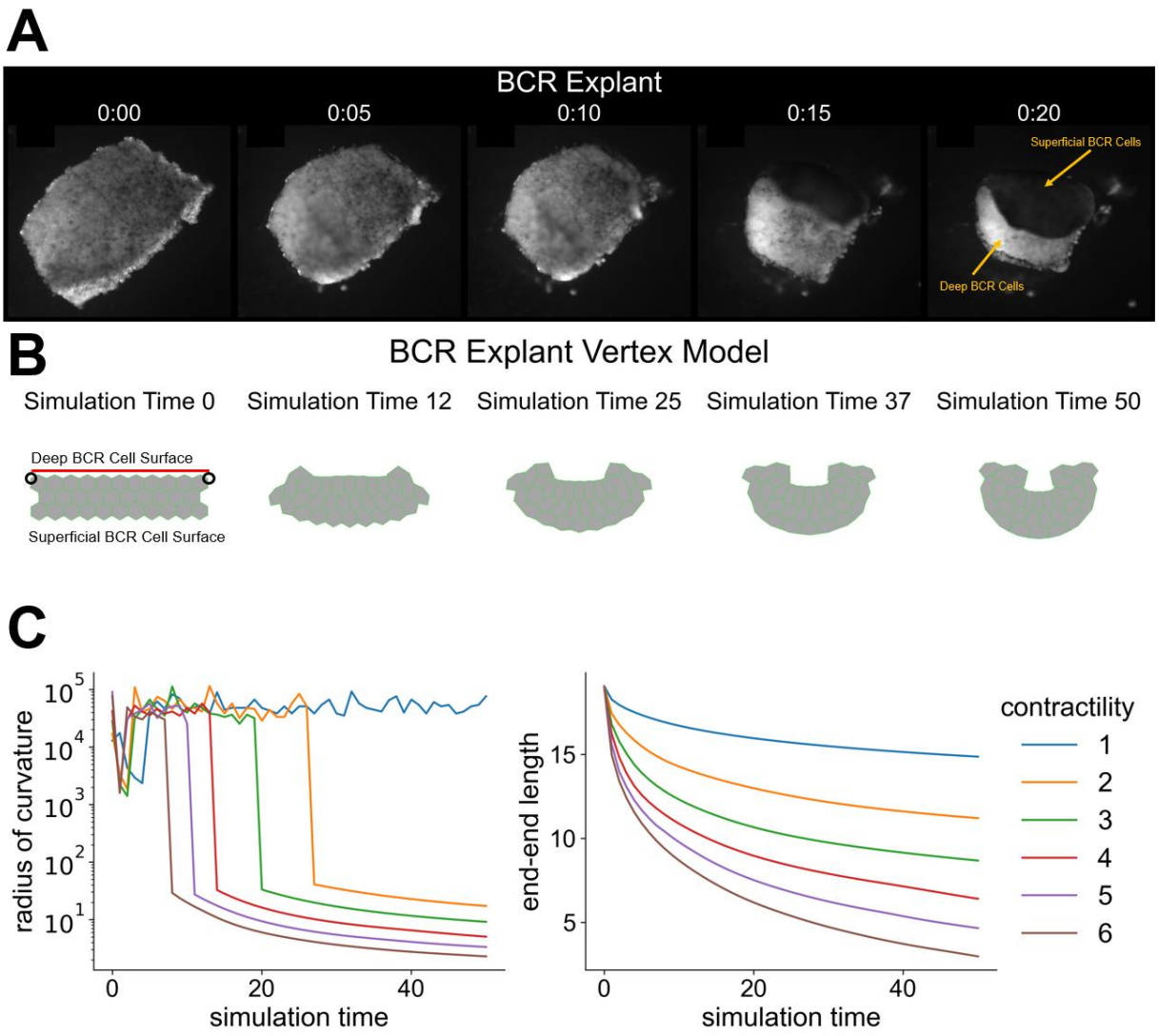

Figure 3- 1 Curling of the explanted blastocoel roof may be explained by tissue surface tension. (A) explanted *Xenopus laevis* blastocoel roof exhibits curling behaviors over 20 minutes after excision from the embryo. The "deep" surface as oriented within the embryo is lighter in color and facing the viewer in the panel marked 0:00 minutes. The "superficial" surface that would anatomically be facing outside the embryo *in vivo* is darker in color and faces the viewer only after curling occurs in 0:15 and 0:20 minutes. Both superficial and deep cells are labeled in the panel marked 0:20 minutes (B) Representative geometry constructed *in silico* as a vertex model with contractile edges along one end to simulate increased tissue surface tension of the face newly exposed to cell culture media (Deep cells of the BCR, highlighted in red

at time 0). (C) Increased tissue surface tension represented by model edge contractility increases rate of curling. Curling is quantified both through radius of curvature and end-to-end length defined as the distance from one end of the explant to the other along the contractile face (black circles in (B) at simulation time 0).

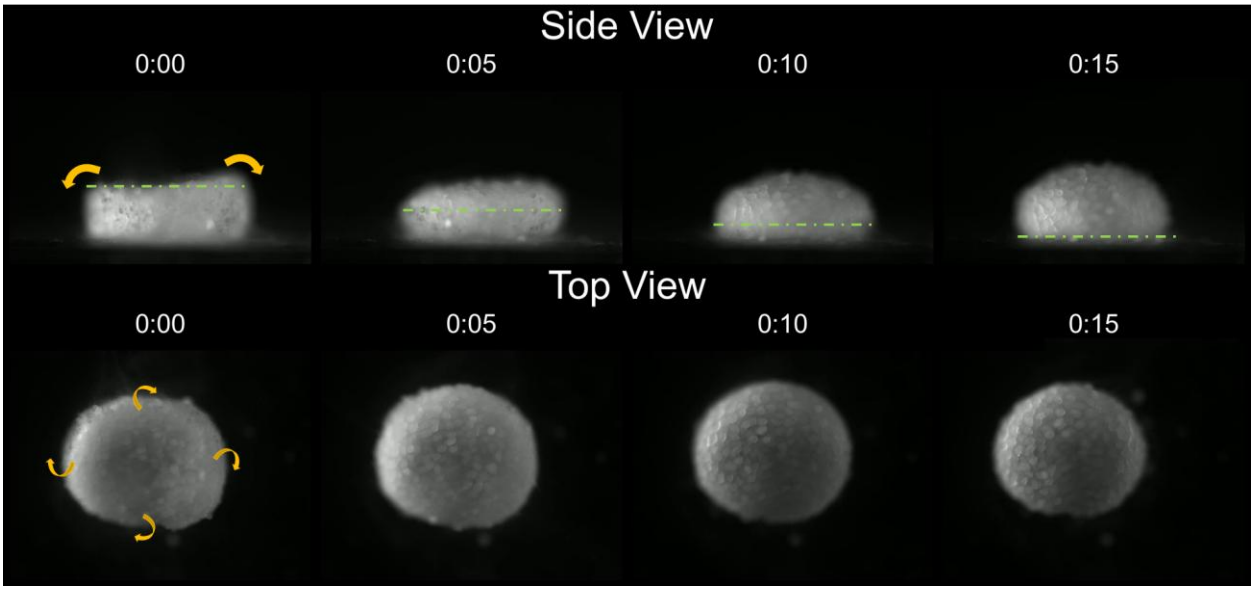

Figure 3- 2 Mesendoderm tissue everts in the roof-less explant. Side and top views of the remainder of the embryo after removing the blastocoel roof; referred to as the roof-less explant. Direction of the tissue eversion is indicated by the yellow arrows in the panels at time 0:00. The green line in the side view indicates the movement of the former leading edge during this spontaneous eversion behavior over a 15 minute time course.

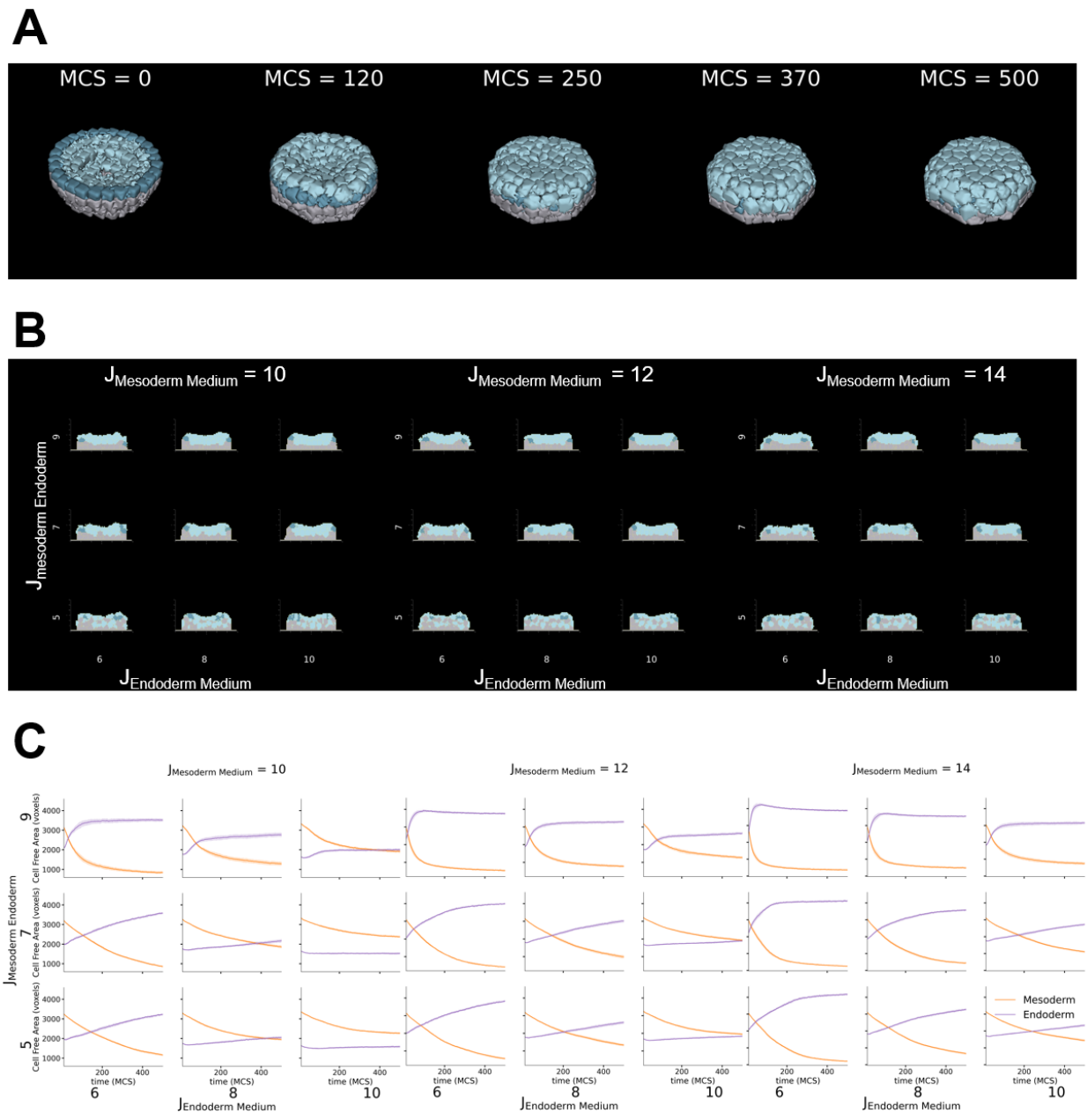

Figure 3- 3 3-Dimensional Cellular-Potts model of the roof-less explant eversion driven by differential adhesion. Representative cup-like geometry of the roof-less explant simulated in the CPM framework with endoderm (light blue), mesoderm (gray), and leading-edge mesoderm (dark blue, colored only as a fiduciary marker and otherwise behaves as mesoderm). (A) Eversion behavior in a representative simulation can be observed over a time course of 500 Monte-Carlo steps (MCS). (B) representative cross-sections of model configurations at MCS=500 of a parameter sweep over contact energy parameters

governing differential adhesion between mesoderm, endoderm, and medium cell types. (C) quantified interface area between mesoderm and medium and endoderm and medium during eversion for corresponding areas of the parameter study in (B). Data in (C) represent mean +/- std. for n=10 simulation replicates.

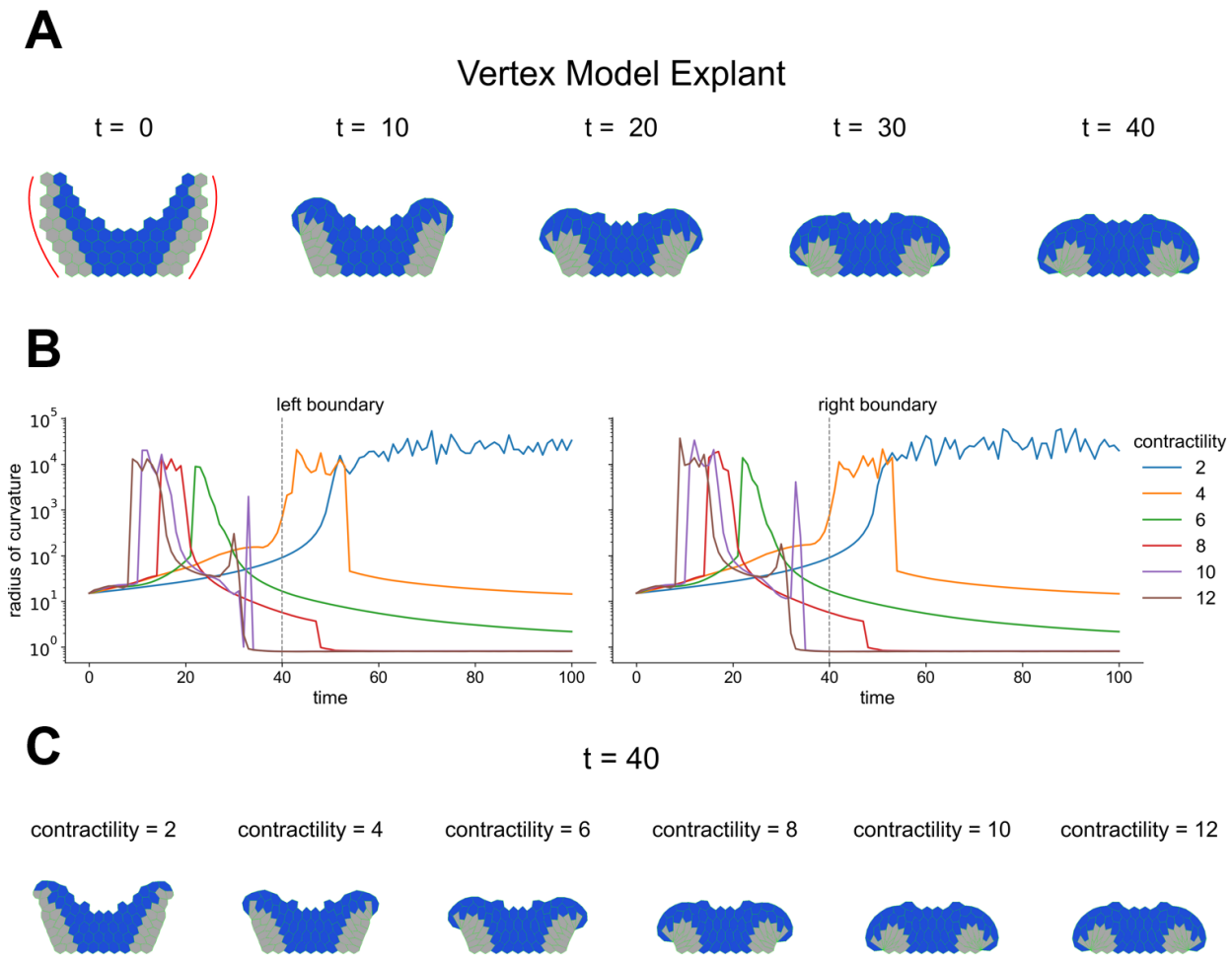

Figure 3- 4 Vertex model recapitulates eversion behavior driven by cortical tension. (A) Representative simulation of a 2-dimensional vertex model exhibiting eversion of approximate roof-less explant mesoderm (gray) and endoderm (blue) geometry due to increased cortical tension of the exposed face of the mesoderm. (A) Time series of eversion of a representative simulation, contractility = 10 in the example. Surface tension on the left and right boundaries of the model is implemented as contractile edges highlighted with red lines in A. (B) Eversion is quantified as a function of simulation time as the radius of curvature of the left and right contractile boundaries of the model for different degrees of contractility. (C) Model configurations at t=40 for each value of contractility, also indicated by the vertical gray line at t=40 in B.

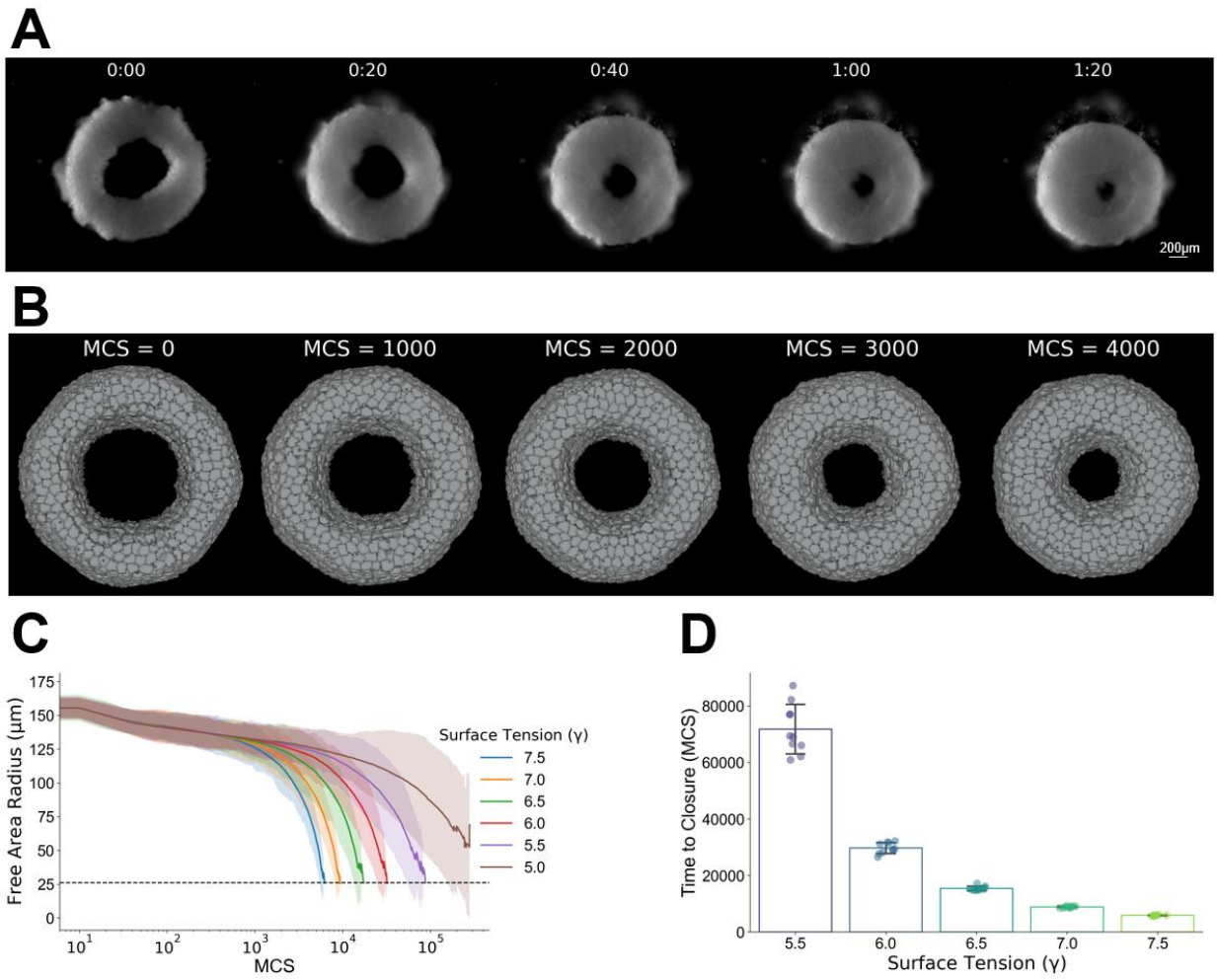

Figure 3- 5 Tissue surface tension in a CPM model replicates toroidal closure. (A) Biological toroidal explant closure over a 1hr 20min time course. (B) Simulated toroidal explant closure over 4000 monte-carlo steps (MCS). (C) Time course of toroidal explant closure with different values of tissue surface tension. (D) Mean time of toroidal closure. Mean and std is shown for n=10 simulation replicates per value of surface tension for simulations in panels C and D.

Table 3 CPM Model Parameters

CPM Model Parameters			
Parameter Name	**Parameter Description**	**Parameter Value**	**Justification**
$J_{c,c}$	Cellular Potts contact energy coefficient between two mesendoderm cells	Ranged from 5-10 in simulation for the toroidal explant	Referenced from literature to define uniform contact affinity between agent types(Swat et al., 2012)
$J_{c,m}$	Cellular Potts contact energy coefficient for the interface between a mesendoderm cell and the medium, and a mesendoderm cell and the substrate	10 for the toroidal explant	Referenced from literature to define uniform contact affinity between cell-substrate and cell-medium types(Swat et al., 2012). Cell-substrate is intended to be effectively the same as cell-medium, and is only used for reporting toroidal inner free area during the simulation
λ_{volume}	Cellular Potts volume constraint	1 for all cell types	Chosen to allow cell deformation during explant migration in the CPM framework
V_{target}	Target volume for all explant cells in the CPM framework	27,000 μm^3	Chosen to allow cells to occupy 5x5x5 voxels in volume, where a 5 voxel distance is approximately 30μm to adequately approximate the size of a mesendoderm cell(Comlekoglu et al., 2024; Longo et al., 2004).
$\mathcal{H}^*$	Temperature parameter for the CPM simulation	20	Chosen to allow for simulation in the CPM formalism

Table 4 Roof-less explant Cellular-Potts model contact parameters.

All other CPM parameters for this model are the same as described in Table 3.

Roof-less explant CPM contact energy parameters			
Parameter Description	**Parameter Name**	**Parameter Value**	**Justification**
Cellular Potts contact energy coefficient for the interface between a one cell type to another or a cell type and the medium	$J_{mesoderm,mesoderm}$	5	Set to allow mesoderm cells to adhere to one another
	$J_{mesoderm,endoderm}$	9	Set to allow endoderm and mesoderm to adhere to one another but still allow endoderm to expand and spread relative to the mesoderm to produce an eversion behavior
	$J_{mesoderm,medium}$	16	Set to produce a high surface tension of mesoderm with the medium as was hypothesized
	$J_{endoderm,medium}$	10	Set to produce a relatively lower surface tension of endoderm with the medium as compared with mesoderm as was hypothesized

Table 5 Parameters for vertex models

BCR Vertex Model Parameters			
Parameter Name	**Parameter Description**	**Parameter Value**	**Justification**
λ^{area}	Cell area constraint strength	3	Set to maintain cell area and during simulation
$\lambda^{tension}$	Edge tension strength for non-contracting edges	3	Set to maintain edge tension between pairs of vertices during the simulation
$\lambda^{contractility}$	Edge tension strength for contracting edges	Ranged from 1-6	Range chosen to allow for quick and visually apparent curling (6), slower curling (3), and almost no curling (1).
A^o	Cell preferred area	2.6 for all cells	Chosen to construct tissue of a given geometry with hexagonal cells
l_{ij}^0	Preferred length for non contracting edges	1 for all edges	Chosen to construct tissue of the given geometry with hexagonal cells
Roof-less explant parameters			
λ^{area}	Cell area constraint strength	1	Set to maintain cell area and during simulation for both mesoderm and endoderm cells
$\lambda^{tension}$	Edge tension strength for non-contracting edges	2	Set to maintain edge tension between pairs of vertices during the simulation
$\lambda^{contractility}$	Edge tension strength for contracting edges	Ranged from 2-12	Range chosen to allow for quick and visually apparent eversion (12), slower eversion (6), and almost no curling (2).

A^o	Cell preferred area	2.6 for all cells	Chosen to construct tissue of a given geometry with hexagonal cells
l_{ij}^0	Preferred length for non contracting edges	1 for all edges	Chosen to construct tissue of the given geometry with hexagonal cells

CHAPTER 4: A flexible fabricated hydrogel platform for quantifying biomechanical forces

ABSTRACT

Quantifying the mechanical forces generated by cells and tissues with complex 3-dimensional geometries is important for understanding many biological and disease processes such as tissue morphogenesis, wound healing, tumorigenesis, and collective cell migration. Current methods for quantifying forces generated by tissues on their environments such as Traction Force Microscopy (TFM), support primarily planar tissue geometries. Existing fabricated constructs built to infer forces generated by natively contractile tissues may be repurposed for this use case, but they either do not support tissues at the 300-1000μm scale, or are too stiff to be sensitive to forces weaker than 10μN. I describe here a platform to infer weak biological forces generated by contractile toroidal-shaped tissue explants through the fabrication of a novel micropillar construct. In addition, this platform may be conjugated with proteins or other active biomimetic peptides to investigate or modulate the force-generating properties of complex biological tissues, such as the natively contractile annular-shaped tissues used in demonstration. The immediate intended application of our platform described here is to infer the magnitude of forces generated during surface-tension mediated contractility of an explanted amphibian embryonic tissue, the mesendoderm mantle.

INTRODUCTION

During development, cells and tissues move and often extend large distances where they ultimately settle into anatomical structures representative of each stage of embryonic development. These tissues deform significantly in three dimensions *in vivo* due to biomechanical forces generated natively within the tissue. Resolving the magnitude of these biomechanical forces can be useful for investigating the underlying biological mechanisms from whence these forces are derived(Davidson et al., 2009). Because multiple tissue movements occur at once during the morphogenesis of the *Xenopus laevis* gastrula, resolving the relative magnitudes of force-generating events would allow for understanding the relative roles of these mechanisms towards the proper development of the embryo.

The action of tissue surface tension is one such effector of cell migration that contributes to the large tissue deformations and tissue rearrangements observed during gastrulation. Tissue surface tension results in tissue self-organization in many tissues throughout the embryo. The surface tension of the different germ layers during gastrulation has been observed to result in their stratification and migration during the development of the zebrafish and the amphibian *Rania pipiens*(Davis et al., 1997; Schötz et al., 2008). During gastrulation of the *Xenopus laevis* embryo, surface tension has been implicated in multiple cell migratory movements. Surface tension has been reported to be involved in radial intercalation events that allow for spreading of mesendoderm during migration and eventual closure of the mesendoderm mantle(Marsden and DeSimone, 2001), force-generating convergent extension events that contribute to tissue movements originating in the involuting marginal zone of tissue(Keller et al., 2000; Shook et al., 2018), and convergent thickening, an additional convergence force that contributes to closure of the blastopore at the vegetal pole of the embryo(Shook et al., 2018; Shook et al., 2022).

The Differential Adhesion Hypothesis (DAH) posited by Malcom Steinberg explains the fluidlike behavior of embryonic tissues spreading upon one another. These include the wetting or spreading of cells and tissues upon their substrates, the sorting of different populations of embryonic cells *in vivo*, and the aggregation of cells into tissues(Steinberg, 2007). The DAH describes these behaviors as resulting from

differences in tension at the interfacial plane of one cell type to another, due to varying concentrations of cell adhesion molecules in different cell and tissue types, which results in varying adhesivity at the interface of one tissue type to another. In addition to differential adhesion, tissue surface tension has been observed to be affected by active actomyosin mediated contractility at the cellular cytoskeleton which, across many cells, affects the surface tension of cellular aggregates and large tissues(Manning et al., 2010).

Quantifying the force generated by surface tension mediated processes during development is challenging. Surface tension mediated processes appear to generate forces on the scale of micronewtons, requiring sensitive experimental setups to measure. In the *Xenopus laevis* embryo, Shook et. al, 2018(Shook et al., 2018) quantified tensile convergence forces at the marginal zone in the range of 1.5 - 4μN using a tractor pull assay designed to measure these forces of the involuting marginal zone tissue explants. Feroze et. al, 2015(Feroze et al., 2015) measured the force of blastopore lip closure at approximately 0.5μN using calibrated cantilevers inserted into the margins of the closing blastopore. While these processes occur in tissue on the opposite end of the embryo to the migrating mesendoderm mantle at the animal pole, because they are surface tension driven processes, we hypothesize that closure of a toroidal explant in the absence of cellular crawling would be due to forces of similar magnitude. Thus, to quantify the hypothesized surface tension driven process of closure of a toroidal (or donut) shaped explant of the migratory mesendoderm mantle, we must be able to measure contractility of <10μN in magnitude.

Open source and commercial solutions exist to quantify forces of cells and tissues upon their substrate and each other. These include solutions such as microneedle arrays or traction force microscopy to quantify traction forces of cellular crawling for collectively migrating mesendoderm(Sonavane et al., 2017; Tan et al., 2003), or millipillar constructs built for assessing engineered cardiac tissues(Tamargo et al., 2021). These constructs are currently insufficient for our investigation because they either accommodate mainly planar tissue geometries rather than the toroidal tissue geometry representative of

the *in vivo* mesendoderm, or they have been described to measure millinewton forces as in the case of the millipillars and may not be sensitive to the micronewton scale of force we expect from the explant. The individual assays previously cited used by Shook and Feroze were successful in part because they were developed specifically to accommodate the explant. In this work, we aim to develop a flexible platform that may be used to directly measure or infer the force of a natively contractile toroidal explant. Our construct must accommodate the toroidal tissue geometry with an inner diameter of 500μm.

Digital light processing (DLP) based 3D bioprinting technology presents a promising method for fabricating a measurement platform to accommodate the tissue explant because of its demonstrated uses in fabricating high-resolution, geometrically elaborate designs out of polymerized hydrogel(Li et al., 2023; Mo et al., 2022; Nam and Kim, 2024). Using DLP based bioprinting, we specify a design using computer-aided design (CAD) software that can accommodate the representative *in vivo* geometry of the toroidal explant and tune bioink composition to allow for a soft enough printed hydrogel material to be sensitive to measure the toroid's native contractility. In this work, we design, print, and apply a DLP printed hydrogel load cell for measuring the native contractility of the toroid explant.

RESULTS

Micropillar design and direct measurement

Measuring the toroid explant presents multiple challenges. Our explant generates weak contractile forces that may be <10 μN natively, the toroid is approximately 0.5mm tall and 1mm in diameter, and toroid explants must remain submerged in media and out of contact with an air water interface. To this end, we designed a micropillar construct to be printed in a standard 6-well glass-bottom plate using a commercial CELLINK BionovaX DLP printer. The designs are required to print on circular microscope coverslips in order to facilitate direct measurement with a mechanical testing device. Figure 4-1 demonstrates the fabrication process, whereby standard 6-well plates are acrylated to allow polymerized hydrogel to adhere to their surface when printed with the DLP printer. Designs are printed directly into the wells or onto coverslips, leaving enough room in each well for the explantation of tissue and positioning on the printed pillars. The pillar design is then imaged under a Zeiss AxioZoom fluorescence stereo microscope to observe and record explant behavior and any pillar deflection. Pillar designs are then directly measured using a micromechanical testing device (CellScale MicroSquisher) and the force generated by the explant may be inferred from the force-displacement relationship of the printed construct derived from micromechanical testing of the construct in isolation.

To quantify the forces generated by toroidal tissue geometries and leave enough working room within the well of a 6-well plate for tissue manipulation, we used the design detailed in Figure 4-2. Each selected pillar specification is 4,000μm in height, with a semicircular cross-section 70μm in radius. Each construct contains six sets of two pillars, where each pillar in a pair is separated by 375μm to accommodate the approximately 475μm inner radius of a toroidal explant. Pillars are placed in close proximity to blocks printed with the same material. The blocks increase the sensitivity of the design to detect weak contractile forces by elevating the tissue 1300μm above the base of the pillars to increase the moment arm at which contractile forces may deflect the pillar structure. The final pillar dimensions are small enough to be threaded through toroidal shaped explant tissue with an inner diameter of 475μm.

Micropillar fabrication and material characterization

Pillars were printed using a bioink that consisted of polyethylene-glycol diacrylate (PEG-DA) and four-arm polyethylene glycol acrylate(four-arm PEG-Ac) (see Methods). This mixture was chosen to obtain a pillar material soft enough to deflect given weak biomechanical forces yet stiff enough to retain its structure given its high aspect ratio of 4mm tall and 70 μm in cross-section diameter. PEG-Ac softens the material after polymerization. Rhodamine B fluorescent dye was also added to the bioink to label the pillars and view under the fluorescence microscope. Labeled pillars with a positioned biological explant are displayed in Figure 4-1. We also incubated printed designs with thiolated rhodamine-B and imaged them as shown in Figure 4-3B). This indicates that these prints may be patterned with bioactive peptides for the modulation of biological processes of interest. This modulation may potentially assist in the investigation of the biological mechanism to which biomechanical forces are generated and modulated *in vivo*. Representative prints are displayed in Figure 4-3, where Figure 4-3(B) displays a design incubated with thiolated rhodamine-B.

To infer forces applied by explants on the pillar constructs, we used a CellScale MicroSquisher to perform cyclic loading (Figure 4-4A) of progressively greater horizontal forces to deflect the pillars in an experimental setup (Figure 4-4C). Micromechanical testing revealed linear force-displacement curves in loading and unloading for multiple replicates (Figure 4-4B). To further characterize and understand the material response under mechanical loads, we performed dynamic mechanical testing to derive a stress-strain relationship of the material. We display the stress-strain relationship measured from tests in uniaxial tension and compression (Figure 4-4D), and find that the material is softer in compression than in tension. The hydrogel material appears brittle in tension. During bending of a pillar structure, we would expect the material to be experiencing both tension and compression stresses.

Experimental application

Experimental tests of a previous pillar design consisting of 2mm tall pairs of pillars at the same diameter are shown in Figure 4-5. These data consist of 16 experimental yielding deflection data from 34 pillars (16 pairs of pillars). Unfortunately, measured pillar diameters after fabrication were highly variable. Measured pillar deflections for different pillar replicates of this design were also variable. Some designs displayed a minor amount of oscillating movement in response to biomechanical forces generated by the contractile explant; however, these movements were minimal such that determining a specific measurement for deflection from microscopy was difficult. These replicates are labeled as “Minor movement” in Figure 4-5.

DISCUSSION

In this work, we define a hydrogel construct that may be fabricated with a DLP printer and characterize the mechanical properties of the fabricated construct. We demonstrate the use of the construct to infer the magnitude of force generated by a natively contractile toroidal tissues extirpated from *Xenopus laevis* gastrulae. Experimental measurements were performed with 2mm tall pillars which were insensitive to the forces generated by multiple toroidal explants. This motivated the current "final" design printed, patterned, and displayed in Figure 4-3. Increasing the height of the overall structure would further increase the moment arm at which biomechanical forces act to bend the pillar construct. This would allow the structure to be more sensitive to weaker forces. However, these 4mm pillar constructs are difficult to reproduce even with consistent bioink formulation and preparation, and consistent parameters used in the DLP print. Printing 4mm pillar designs yields a majority of prints that fail to polymerize pillar material at the intended height of 700μm above the 3.3mm tall blocks. This is likely because above the blocks, the size of the photomask applied by the printer is abruptly decreased. This may be due to a relative decrease in free radicals at the site of the smaller photomask resulting in greatly decreased print resolution. This results in shortened and tapered pillar structures above the blocks and may explain the tapered appearance of the pillars when viewed laterally in the micromechanical testing device as shown in Figure 4-4. Additionally, this may explain the high variability in pillar widths after attempting to print with a consistent pillar CAD design demonstrated in Figure 4-5. We have attempted to remedy this by introducing polyethylene oxide to significantly increase the viscosity of the bioink before polymerization in an effort to increase the concentration of free radicals in the area of the photomask by attempting to prevent local convection currents from forming in the bioink during polymerization. These attempts have yet to be successful, and future efforts may further iterate these approaches to increase the resolution and reproducibility of printed designs with DLP printers at this spatial scale.

The difficulty in measuring the more subtle pillar deflections labeled as "Minor movement" in Figure 4-5 is a significant limitation to the use of this method experimentally. The experimental replicates shown demonstrate the movement of unperturbed, control explants. Ideally, the method would be

sensitive to weaker biomechanical forces measured by experimentally perturbed explants with hypothesized biological mechanisms of contractility knocked down. Tissue surface tension is thought to be a function of both cortical tension and intercellular adhesion(Farhadifar et al., 2007; Krieg et al., 2008; Lecuit and Lenne, 2007). Alterations in cytoskeletal acto-myosin activity (affecting cortical tension) or intracellular signaling cascades that affect expression of cell adhesion molecules (resulting in differential intercellular adhesion) might alter and help explain the native physiological behavior of tissues in the context of their in-vivo environment. An applicable example of this is the observation that Lewis lung carcinoma cells demonstrate increased propensity for invasion associated with loss of E-cadherin(Foty and Steinberg, 1997). Authors Foty and Steinberg observe that invasive activity may be suppressed through increasing expression of either P or E-cadherin. They went on to find that treatment with the common corticosteroid dexamethasone increased expression of cadherin and decreased invasiveness of human fibrosarcoma cells in culture(Foty et al., 1998). An assay sensitive to decreases in contractility due to perturbations in the mechanisms of tissue surface tension would be useful to identify and investigate additional effectors of tissue surface tension.

While the demonstrated experimental application of the construct using toroid explants were imprecise, the explants did produce enough biomechanical force to deflect the fabricated pillars even if many deflections were difficult to explicitly measure. The force-displacement relationship derived through micromechanical testing implies that any observed movement of the pillars likely is the result of forces on the scale of micronewtons. Previously, the major driving force for mesendoderm mantle closure at the animal pole of the *Xenoopus laevis* embryo at this stage of gastrulation was thought to be due to lamellipodial protrusive behavior of migratory cells at the leading-edge of the tissue(Davidson et al., 2002). However, multiple studies quantifying the forces generated through lamellipodial extension suggest that the magnitude of these forces are in the range of 0-30piconewtons(Bornschlögl et al., 2013; Romero et al., 2012; Shahapure et al., 2010). Additionally, traction force microscopy experiments performed by Sonavane et. al.(Sonavane et al., 2017) on the migratory behavior of the mesendoderm

tissue at this stage of development reveal average traction stresses of approximately 200Pa at the leading edge, which resolves to 0.012μN of force when considering the 8μm x 8μm areas over which stresses were calculated. These findings suggest that the native contractility of the explant, thought to be due to tissue surface tension, results in forces of at least 2-orders of magnitude greater than that of crawling. Therefore, tissue surface tension is either a major driving mechanism of mesendoderm mantle closure, or is modulated *in vivo* during the native development of the embryo.

Finally, we have demonstrated the ability to pattern these hydrogel constructs with thiolated bioactive peptides. This may potentially allow for investigation of the modulation of the mechanisms responsible for the generation of biomechanical forces measured by the construct described in this chapter. In Chapter 3, we discuss how the native tissue surface tension properties of the explanted tissue may drive observed tissue reorganization behavior. In this chapter, we have discussed how the magnitudes of these forces may be orders of magnitude greater than cell crawling, which was previously understood as a primary mode of collective migration of this tissue *in vivo*. Current unpublished work in the DeSimone lab gathered by staff scientists David Shook and Bette Dzamba makes the case that fibronectin that exists within the embryo may reduce the surface tension of migratory mesendoderm tissue. The fabricated micropillar construct may potentially be patterned with fibronectin to investigate how explant adhesion to a fibronectin-rich substrate may alter the forces generated by the toroidal (or donut) explant. Currently, introducing fibronectin to these explants results in a decrease in tissue surface tension which we would expect to decrease the native contractility of the toroidal explant. Our constructs currently appear too stiff to reliably measure the native contractility of the explants. Unfortunately, these constructs are not yet sensitive enough to allow for reliable measurement of the reduced contractile forces that we would expect from patterning fibronectin or other bioactive molecules onto them. However, ongoing work in the DeSimone lab to investigate the downstream signaling mechanisms responsible for the modulation of tissue surface tension in these explants have observed that treating with a drug to inhibit focal adhesion kinase (FAK), a downstream effector of integrin-fibronectin signaling, results in

more dramatic explant behavior. We would expect that the micropillar constructs as currently described may be able to reliably measure forces generated explants treated with FAK inhibitor as they would likely demonstrate increased contractility.

In this chapter, I have described the development of a hydrogel construct used to infer the relative magnitude of a natively contractile mesendoderm explant that represents the native geometry of the tissue *in vivo*. In addition, we demonstrated the potential for our hydrogel explant to be patterned with bioactive peptides to assist in further investigation of factors that may modulate biomechanical forces. While the proposed geometry is specific to the tissue explant, the material characterization of the hydrogel material described in this study is applicable regardless of construct geometry. Additionally, using a hydrogel material polymerized through DLP technology allows for specification of arbitrary geometry that may be customized to be well suited to other experimental setups.

METHODS

Micropillar Construct Fabrication

While the method and system is flexible and may be realized with varying materials and printer technologies, the pillars used as example here were fabricated using a digital light processing (DLP) bioprinter and a hydrogel bioink synthesized by our group. DLP printer bioink was formulated using polyethylene glycol diacrylate (PEGDA, 12.5v%, 200Da), four-arm polyethylene glycol acrylate (PEG-Ac, 5w/v%, 10kDa), and a solution of 20mM lithium phenyl-2,4,6-trimethylbenzoylphosphinate (LAP) photoinitiator for use with the DLP printer. Designs were printed using 50μm vertical slices at 30% light intensity at 0.02mm/s printer probe velocity.

Glass bottom plates were acrylated to allow the structure to adhere to them during the printing process. Pillar designs were printed in standard 6 well glass bottom black plates with a 1.5 cover glass. The plates were plasma cleaned with air for two minutes then a drop of our 3-(Trimethoxysilyl)propyl acrylate was added to coat the bottom of each well. The plate is then placed under vacuum to dry for 60 hours covered from light. The plate was then stored at 4°C till used.

For characterizing the mechanics of the printed structures as described in the section titled Material Characterization, the structures were printed on 22mm glass coverslips acrylated via treatment with the same methods described for preparing the glass bottom plates above.

Tissue Explant Preparation

Toroidal tissue preparations were explanted through microsurgery of stage 11.5 *Xenopus laevis* embryos. Briefly, the vitelline membrane of the embryo was removed and a superficial incision was created along the equator of the spherical embryo. The epithelial tissue “cap” of the embryo superior to the incision was lifted without damaging the underlying mass of tissue underneath. A toroidal tissue structure was then created by bisecting the embryo at the initial equatorial incision to isolate a mantle of tissue that is revealed by lifting the epithelial cap from the developing embryo. This yielded a toroidal

shaped tissue explant that contracts natively. Further detail can be found in Davidson et al, 2002(Davidson et al., 2002).

Experimental Application

Toroidal explants of contractile tissue were prepared from *Xenopus laevis* embryos at stage 11.5 as described in subsection Tissue Explant Preparation, and the micropillar structure was threaded through the explant of initial inner diameter of approximately 500μm. The pillar structures were imaged continuously for 60 minutes using fluorescent stereo zoom microscopy (Figure 1B). To infer forces generated by the explant, we measured and reconstructed the force-displacement relationship through cycling horizontal loading of printed micropillar constructs

Material Characterization

(i) dynamic mechanical analysis

Rheological behavior of bulk PEG ink gel was characterized using a rheometer (DHR3, TA instruments), equipped with a 8 mm parallel plate geometry. A 8mm Poly(dimethyl)siloxane Sylgard 184 kit (Dow Corning) mold was used to fabricate a bulk gel. The gel was allowed to swell overnight in PBS at room temperature. Dynamical mechanical analysis (DMA) in compression was done at 5 μm/s until failure. DMA in tension was done at the same rate till failure but the rectangle tension fixture was used and the PEG ink was cured to form a slab that is 9 mm long.

(ii) printed structure deflection

The force-displacement relationship of the fabricated structures was determined using a micro-scale tension-compression device (MicroSquisher, CellScale). During testing, a cylindrical probe 100um in diameter was used to horizontally deflect printed pillar structures in a cyclic loading-unloading pattern. During loading cycles, the testing probe applied forces of 0.5, 1, 2, and 4μN of force from which resulting pillar displacement was measured.

Material Patterning

After printing a 1mM thiolated rhodamine B (GCDDD-rhodamineB) and 1mM LAP solution was added to the pillars and let sit at room temperature for 45 minutes to diffuse into the hydrogel pillars. After which each well was placed under UV light at 15mW/cm^2 (Omnicure 320-390) for 60s. The thiolated rhodamine B and LAP solution was removed, and PBS was added to the pillars. The pillars sat at 4°C overnight to allow unreacted thiolated rhodamine B to diffuse out before imaging.

FIGURES AND TABLES FOR CHAPTER 4

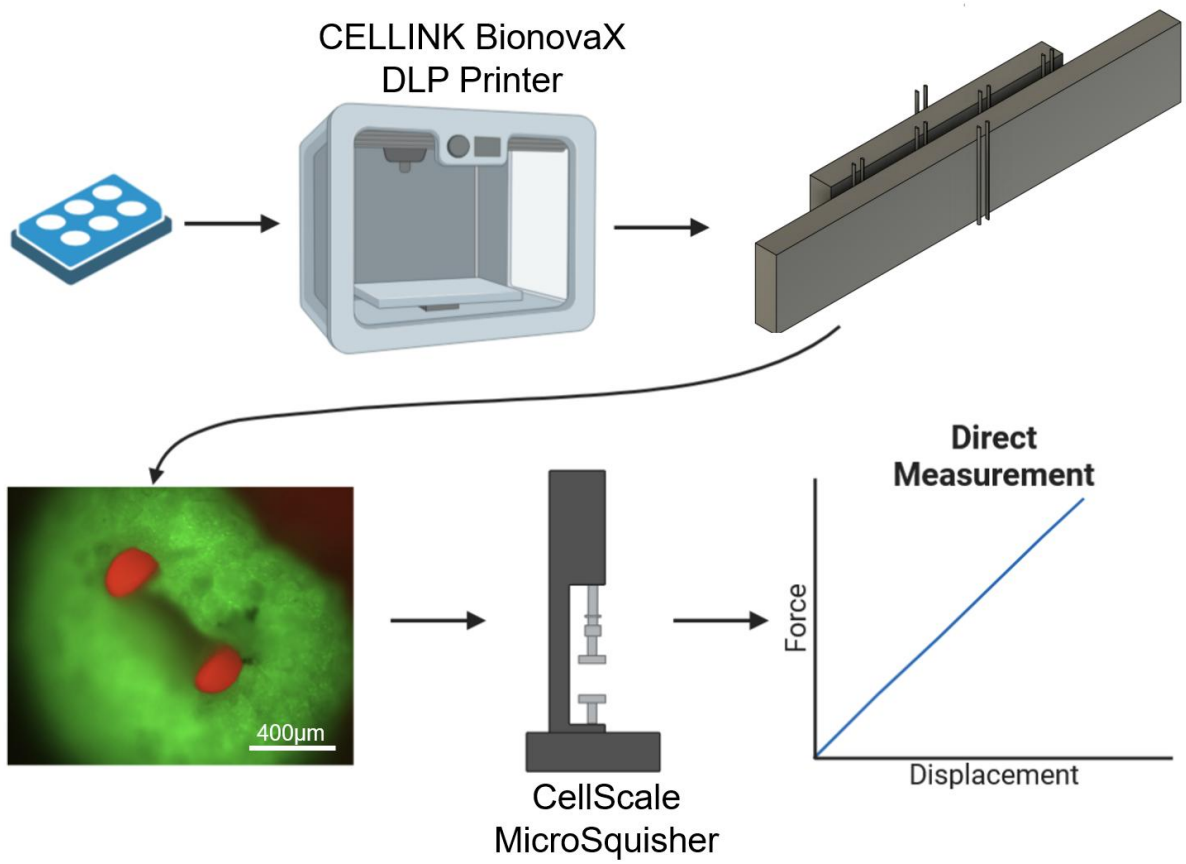

Figure 4- 1 Micropillar fabrication and force inference process. (Top row) Prepared bioink is pipetted into a standard 6-well glass bottom plate and placed into a CELLINK BionovaX DLP Printer. The DLP printer prints the specified design. (Bottom row) Printed designs may then be used in experiment, and observed deflections may be reproduced with a CellScale MicroSquisher micromechanical testing device to directly measure the force required to displace pillar structures to the degree observed in experiment.

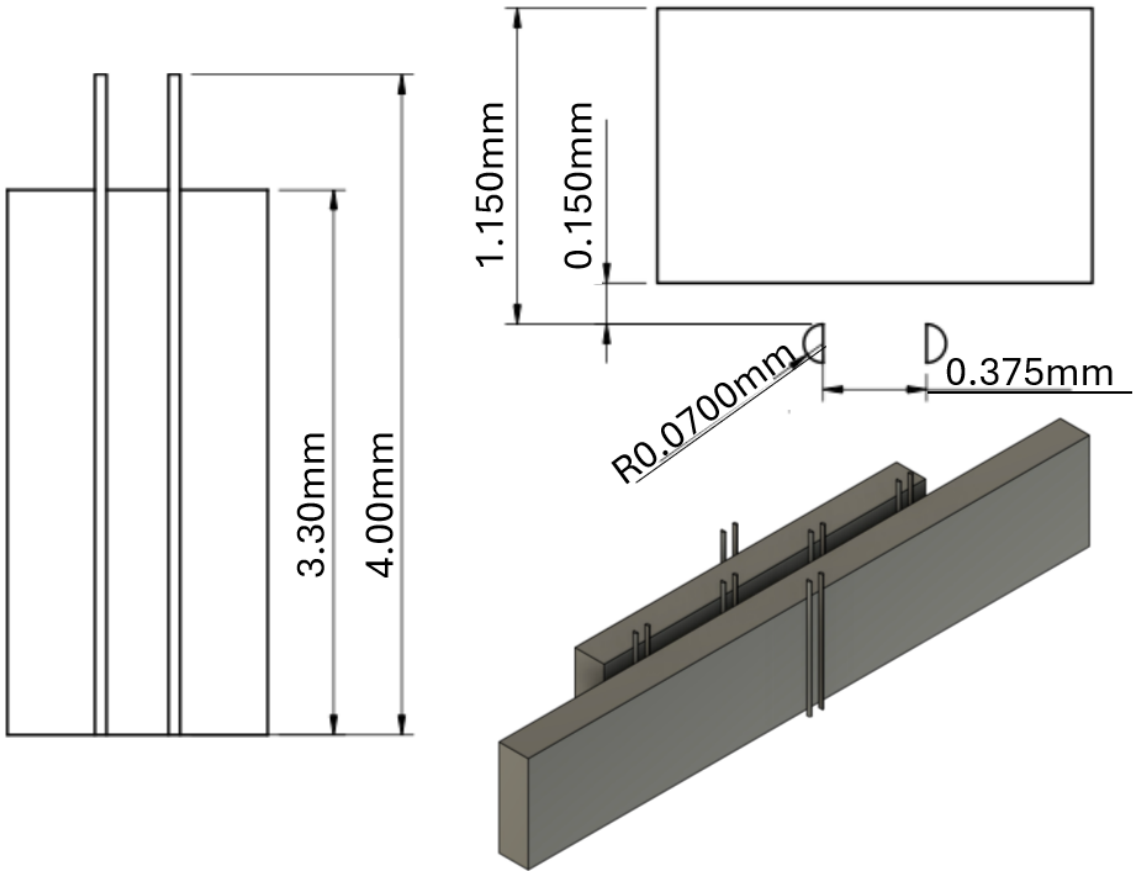

Figure 4- 2 Micropillar construct design schematic. Micropillar design for DLP printing. Designs were created using Autodesk Fusion 360 CAD software and exported as the standard stereolithography (.stl) file format for use with the CELLINK BionovaX DLP printer.

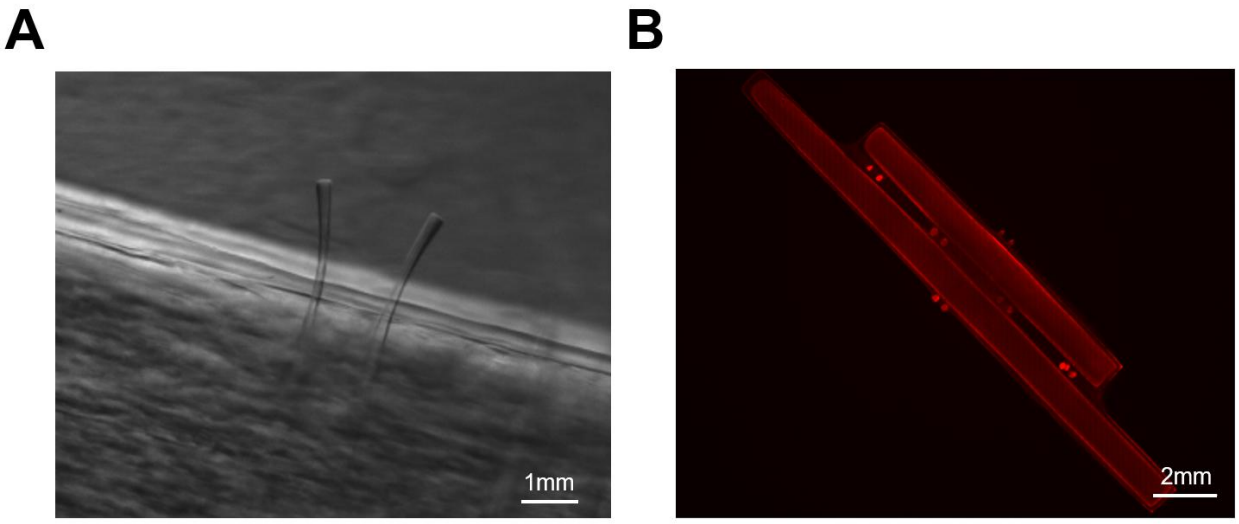

Figure 4- 3 Representative micropillar prints. (A) Lateral view of a printed pillar pair for use in biomechanical force measurement. (B) Stereo zoom imaging of the pillar construct, red fluorescence is the result of thiolated fluorophore conjugated to the pillar material, demonstrating potential as a flexible patterned microenvironment.

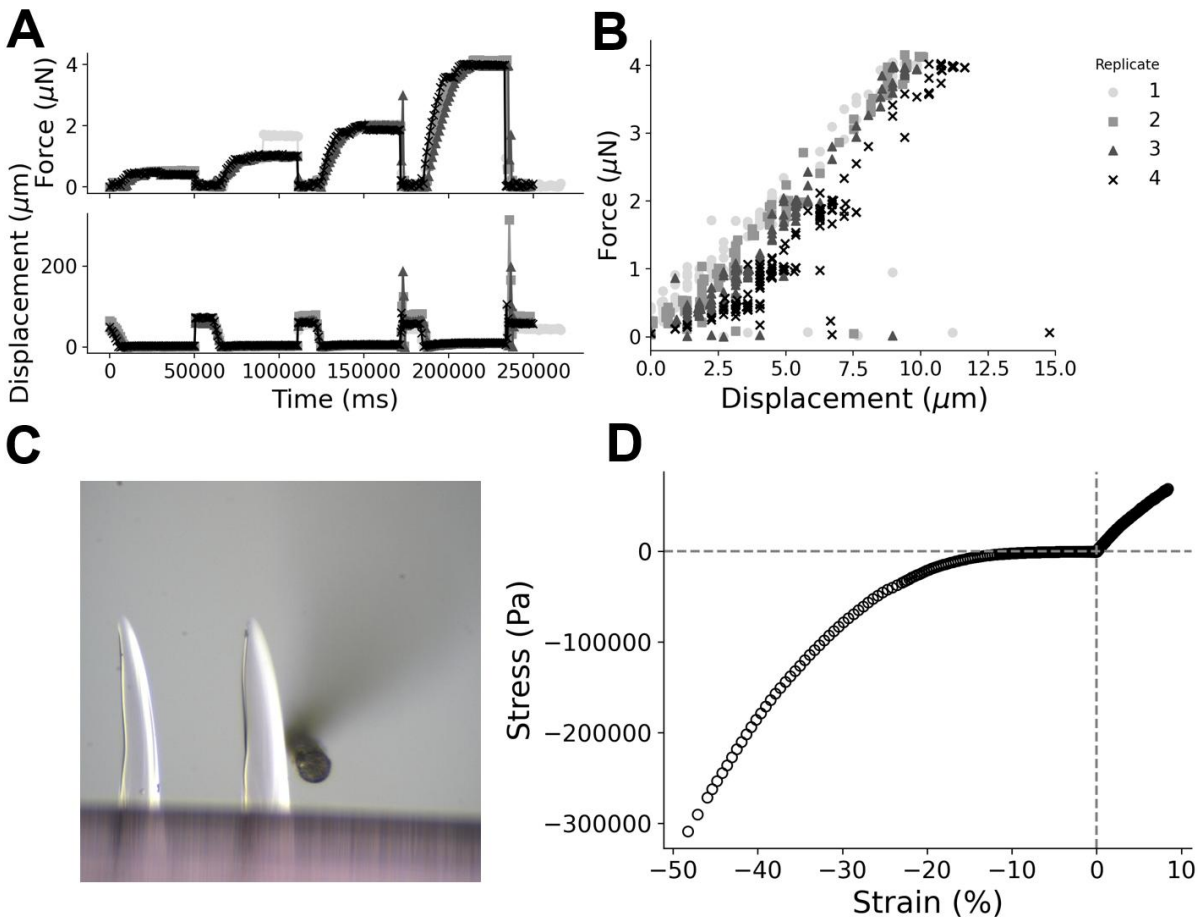

Figure 4- 4 Micromechanical testing reveals a linear force-displacement relationship. (A) Applied force and resulting pillar deflection measures during cyclic micromechanical testing for 4 experimental replicates with sample large prints approximately 150μm in semicircular cross section radius. (B) Loading and unloading data during micromechanical testing reveal a linear force-displacement relationship from which the relative contractile force can be inferred. (C) representative image of micromechanical testing setup. Measurement probe deflects the pillars horizontally and applied force and resulting displacement measurements over time are recorded. (D) The stress and strain response under both compressive and tensile loading is shown for a our selected bioink formulation. Data shown represents the mean of n=3 replicates in compression, n=2 replicates in tension prior to material failure.

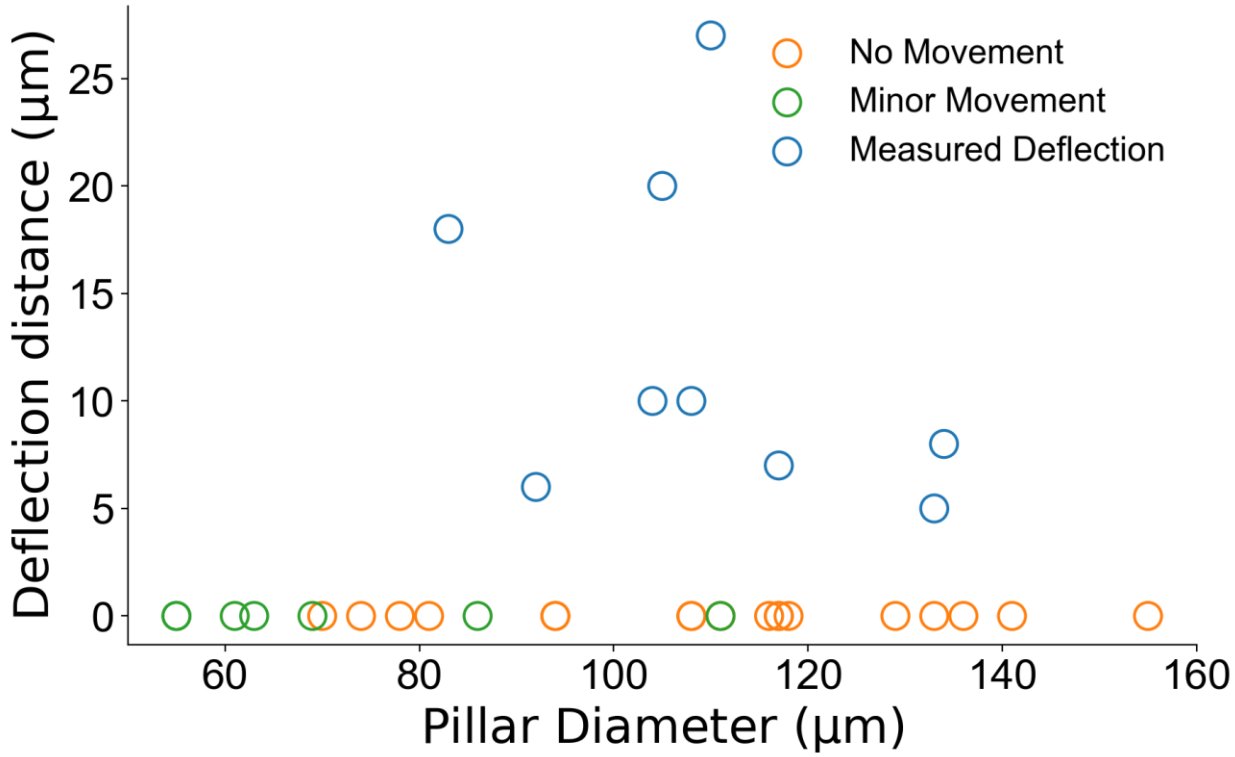

Figure 4- 5 Pillar deflections for various pillar diameters in experimental application. 2mm tall pillars with an intended pillar semicircular cross-sectional radius of 70µm were tested with contractile toroidal explants.

CHAPTER 5: Conclusions and future work

In this thesis, I discuss, model, and build tools to measure multiple biological processes that contribute to migration of a collective of cells, or self-reorganization of multicellular tissues. I develop computational models that allow for the representation of behaviors of single cells and observe how tissue-scale behaviors emerge from the modeled cellular processes. As discussed in the introduction, collective cell migration and tissue reorganization are fundamental processes that are conserved across model systems of wound healing, cancer metastasis, and tissue morphogenesis. In developing these models, I explore what the implications of these processes are for tissues adopting the complex geometries that exist in the developing *Xenopus laevis* embryo.

In Chapter 2, I describe and model the cellular behaviors of cohesotaxis and intercalation. I present a novel algorithm for representing cohesotaxis in a modular and extendable way that may be easily adapted and applied to other agent-based models consisting of motile cell agents. I additionally represent cell-cell and cell-substrate adhesion dynamics such that I allow for behaviors of intercalation to emerge. With these two cellular processes defined *in silico*, I am now able to investigate how these processes affect the speed of a migrating tissue. Applying my model, I define how intercalation and the native geometry of a tissue as it exists *in vivo* is supportive of an increased rate of tissue migration. My models are readily extendable to the elaborate 3-dimensional tissue geometries that exist in a developing embryo *in vivo*. The work in this chapter has highlighted the influence geometry has on cell migration as well as how it overrides the influence of directed migration provided by cohesotaxis. Applying these model mechanisms to more representative *in vivo* geometries would similarly allow for the investigation of how different migratory mechanisms cooperate or interfere with each other within the embryo.

In Chapter 3, I apply both Cellular-Potts and vertex modeling methods to investigate how mechanisms of tissue surface tension may act as a driving force for tissue self-organization behaviors of *Xenopus laevis* gastrula stage explants. These models represent the actions of tissue surface tension in isolation. Because of 1) the mathematical simplicity of these models and 2) the implementation of these models in the open-source modeling environments of CompuCell3D and Tissue Forge, they may be

combined with the work from Chapter 2 to build towards a representative virtual embryo at the gastrula stage.

At present, the modeling work presented here is limited in its ability to comprehensively represent the embryo. Most of the models developed in this thesis rely on the Cellular-Potts algorithm. This algorithm represents cellular behaviors in a statistical framework where representations of forces that encourage cellular and tissue movements in the simulation environment are difficult to correlate with explicit measures of forces and stresses. This presents a challenge for determining the relative influence of one migratory mechanism compared with another to drive tissue movements in the developing embryo. The micropillar constructs from Chapter 4 allow me to theorize about the two migratory mechanisms of cell crawling and tissue surface tension. I discussed how the inferred magnitudes of forces from a tissue surface tension mediated toroid closure compared with the forces generated through the migratory mechanism of cellular crawling. However, this exercise itself is limited in that we expect the surface tension of the toroid tissue explanted from the embryo to differ from mesendoderm within the embryo. The extent to which this tissue surface tension is modulated *in vivo* is currently unclear. While comparison of experimentally quantified magnitudes of forces may yield insight into the balance of some migratory mechanisms, experimentally modulating other mechanisms of migration (such as cohesotaxis or intercalation) in isolation may be impossible.

While it is difficult to determine the relative roles of mechanisms that are difficult to study in experiment or observe *in vivo*, progress towards this goal could be made by instead asking the question: which mechanisms are *required*? An initial example of this is presented in Chapter 2, where the influence of cohesotaxis is made less relevant by the construction of representative *in vivo* geometry. Thus, geometry allows for directed migration in the absence of a cohesotactic mechanism. A more comprehensive "virtual embryo" could feasibly be created by applying all the modular model mechanisms described in this dissertation into one larger model with a realistic number and configuration of cells.

To obtain a representative model configuration, we may look to unpublished imaging currently collected by the DeSimone lab. The lab has created confocal imaging datasets of the mesendoderm mantle of multiple fixed and stained whole embryos. These imaging data of fixed embryos may be manually segmented and imported into a CompuCell3D or TissueForge simulation environment with the model mechanisms developed in this thesis already applied. This would yield a virtual representation of the animal pole of the *Xenopus laevis* gastrula with a realistic number and organization of mesendoderm cells. This virtual embryo may be calibrated to data consisting of measured rates of closure of live albino embryos that lab manager Ben Edwards in the DeSimone lab has gathered, as well as average morphometric data of individual cells and that of the entire tissue could be determined from segmentation data of fixed embryos at multiple time points.

Calibration data for this virtual embryo would thus consist of optimizing three main objectives: 1) rate of toroidal closure over time, 2) a morphometric measure of individual cell shapes, and 3) a morphometric measure of the shape of the mesendoderm mantle over time (how stretched out or bunched up it may be). Because we have multiple model mechanisms that affect migration, and multiple parameters per mechanism, we may be presented with an overdetermined system when attempting to calibrate a comprehensive model. However, I believe it would be informative to attempt a sensitivity analysis of model mechanisms to determine which specific mechanisms have the greatest influence over the fit, and which mechanisms could be removed while still maintaining a good fit to the data. Validation of this model could consist of reproducing morphometric changes present in experimentally perturbed embryos. We know from other efforts in the DeSimone lab that certain perturbations such as knocking down fibronectin through injecting FN-morpholino at the 2-cell stage, then fixing and imaging at stage 11.5 (our stage of interest) yields a mesendoderm mantle that closes more slowly and is thicker and less tightly adhered to the ectodermal blastocoel roof. Understanding the combinations of model mechanisms that can be both calibrated and validated in this way would yield a greater theoretical understanding of the described cell- and tissue- scale migratory mechanisms at physiological scale.

A significant outstanding challenge to pursuing this proposed investigation is gathering the additional required imaging data. Current confocal imaging of a limited region of the mesendoderm mantle yields thousands of cells which is very difficult to manually segment. Currently, we've attempted to label cells by staining for phosphomyosin, β-catenin, and membrane-bound GFP, however we have yet to find a membrane label suitable for applying automated volumetric segmentation tools, and current cell membrane labels are difficult to reliably segment manually. We are currently facing difficulty manually segmenting all mesendoderm cells in a one-fourth section of the toroid as it is viewed *in situ*. Calibration and validation data for this next step would require segmenting all cells from imaging of multiple embryos each at multiple time points.

While most of the model mechanisms described in this dissertation are implemented in the Cellular-Potts model environment, the vertex models exist in a separate framework and there are notable differences that may serve as a barrier to the proposed investigation. Cells in the Cellular-Potts model environment exist on a square lattice which makes translating imaging data to the simulation environment convenient. In contrast, the vertex model method is an off-lattice method requiring the construction of mesh objects made of vertices, edges, and faces. Additional software tools would need to be developed for this virtual embryo model to import segmented imaging data into the vertex model simulation environment.

Work in Chapter 4 defines a novel construct to explicitly quantify the magnitude of biomechanical force generated by the surface tension properties of mesendoderm tissue. Toroidal mesendoderm explants appear to generate forces on the scale of micronewtons in the absence of cell crawling. This scale of force is much greater than literature reported measurements of the traction stresses produced during lamellipodial or filopodial extension-retraction events. These findings, along with those from Chapter 3, support ongoing work in the DeSimone lab that extracellular matrix constituent proteins (likely fibronectin) decrease the tissue surface tension of migrating tissues to support migration *in vivo*. The 3D printed hydrogel construct described here may also be patterned with RGD or fibronectin to

support further experimental investigation into this phenomenon. Measuring toroid contractility with fibronectin coated pillars would be of immediate interest to ongoing efforts in the lab. We currently hypothesize that fibronectin-integrin mediated signaling results in a decrease in actomyosin contractility of contacting cells, thus reducing the surface tension of the tissue in the embryo. Fibronectin coated pillars would be expected to measure a decreased contractility due to decreased tissue surface tension resulting from cellular contact with fibronectin.

This thesis has resulted in the development of both computational and experimental tools with which we may continue to investigate how cells and tissues migrate and self-organize. While collective migration and tissue self-organization is very relevant for development and morphogenesis, the same underlying biological processes that result in these movements are active and relevant in other broadly studied physiologic phenomena such as wound healing and cancer metastasis. The computational methods developed in this thesis are similarly relevant to other widely studied systems of cell motility and migration.

REFERENCES

Adhyapok, P., Piatkowska, A. M., Norman, M. J., Clendenon, S. G., Stern, C. D., Glazier, J. A. and Belmonte, J. M. (2021). A mechanical model of early somite segmentation. *iScience* **24**, 102317.

Alfandari, D., Wolfsberg, T. G., White, J. M. and DeSimone, D. W. (1997). ADAM 13: a novel ADAM expressed in somitic mesoderm and neural crest cells during Xenopus laevis development. *Dev. Biol.* **182**, 314–330.

Alfandari, D., Cousin, H., Gaultier, A., Smith, K., White, J. M., Darribère, T. and DeSimone, D. W. (2001). Xenopus ADAM 13 is a metalloprotease required for cranial neural crest-cell migration. *Curr. Biol.* **11**, 918–930.

Alfandari, D., Cousin, H., Gaultier, A., Hoffstrom, B. G. and DeSimone, D. W. (2003). Integrin α5β1 supports the migration of Xenopus cranial neural crest on fibronectin. *Dev. Biol.* **260**, 449–464.

Alt, S., Ganguly, P. and Salbreux, G. (2017). Vertex models: from cell mechanics to tissue morphogenesis. *Philos. Trans. R. Soc. Lond. B Biol. Sci.* **372**,.

An, G., Mi, Q., Dutta-Moscato, J. and Vodovotz, Y. (2009). Agent-based models in translational systems biology. *Wiley Interdiscip. Rev. Syst. Biol. Med.* **1**, 159–171.

Ataliotis, P., Symes, K., Chou, M. M., Ho, L. and Mercola, M. (1995). PDGF signalling is required for gastrulation of Xenopus laevis. *Development* **121**, 3099–3110.

Barbacena, P., Dominguez-Cejudo, M., Fonseca, C. G., Gómez-González, M., Faure, L. M., Zarkada, G., Pena, A., Pezzarossa, A., Ramalho, D., Giarratano, Y., et al. (2022). Competition for endothelial cell polarity drives vascular morphogenesis in the mouse retina. *Dev. Cell* **57**, 2321-2333.e9.

Barua, D., Nagel, M. and Winklbauer, R. (2021). Cell-cell contact landscapes in Xenopus gastrula tissues. *Proc Natl Acad Sci USA* **118**,.

Belmonte, J. M., Swat, M. H. and Glazier, J. A. (2016). Filopodial-Tension Model of Convergent-Extension of Tissues. *PLoS Comput. Biol.* **12**, e1004952.

blender.org - Home of the Blender project - Free and Open 3D Creation Software.

Bornschlögl, T., Romero, S., Vestergaard, C. L., Joanny, J.-F., Van Nhieu, G. T. and Bassereau, P. (2013). Filopodial retraction force is generated by cortical actin dynamics and controlled by reversible tethering at the tip. *Proc Natl Acad Sci USA* **110**, 18928–18933.

Brieher, W. M. and Gumbiner, B. M. (1994). Regulation of C-cadherin function during activin induced morphogenesis of Xenopus animal caps. *J. Cell Biol.* **126**, 519–527.

Chan, W. K. V., Son, Y.-J. and Macal, C. M. (2010). Agent-based simulation tutorial - simulation of emergent behavior and differences between agent-based simulation and discrete-event simulation. In *Proceedings of the 2010 Winter Simulation Conference*, pp. 135–150. IEEE.

Comlekoglu, T., Dzamba, B. J., Pacheco, G. G., Shook, D. R., Sego, T. J., Glazier, J. A., Peirce, S. M. and DeSimone, D. W. (2024). Modeling the roles of cohesotaxis, cell-intercalation, and tissue geometry in collective cell migration of Xenopus mesendoderm. *Biol. Open* **13**,.

Davidson, L. A., Hoffstrom, B. G., Keller, R. and DeSimone, D. W. (2002). Mesendoderm extension and mantle closure in Xenopus laevis gastrulation: combined roles for integrin alpha(5)beta(1), fibronectin, and tissue geometry. *Dev. Biol.* **242**, 109–129.

Davidson, L. A., Keller, R. and DeSimone, D. W. (2004). Assembly and remodeling of the fibrillar fibronectin extracellular matrix during gastrulation and neurulation in Xenopus laevis. *Dev. Dyn.* **231**, 888–895.

Davidson, L., von Dassow, M. and Zhou, J. (2009). Multi-scale mechanics from molecules to morphogenesis. *Int. J. Biochem. Cell Biol.* **41**, 2147–2162.

Davis, G. S., Phillips, H. M. and Steinberg, M. S. (1997). Germ-layer surface tensions and "tissue affinities" in Rana pipiens gastrulae: quantitative measurements. *Dev. Biol.* **192**, 630–644.

De Pascalis, C., Pérez-González, C., Seetharaman, S., Boëda, B., Vianay, B., Burute, M., Leduc, C., Borghi, N., Trepat, X. and Etienne-Manneville, S. (2018). Intermediate filaments control collective migration by restricting traction forces and sustaining cell-cell contacts. *J. Cell Biol.* **217**, 3031–3044.

Farhadifar, R., Röper, J.-C., Aigouy, B., Eaton, S. and Jülicher, F. (2007). The influence of cell mechanics, cell-cell interactions, and proliferation on epithelial packing. *Curr. Biol.* **17**, 2095–2104.

Feroze, R., Shawky, J. H., von Dassow, M. and Davidson, L. A. (2015). Mechanics of blastopore closure during amphibian gastrulation. *Dev. Biol.* **398**, 57–67.

Fletcher, A. G., Osterfield, M., Baker, R. E. and Shvartsman, S. Y. (2014). Vertex models of epithelial morphogenesis. *Biophys. J.* **106**, 2291–2304.

Fortuna, I., Perrone, G. C., Krug, M. S., Susin, E., Belmonte, J. M., Thomas, G. L., Glazier, J. A. and de Almeida, R. M. C. (2020). Compucell3d simulations reproduce mesenchymal cell migration on flat substrates. *Biophys. J.* **118**, 2801–2815.

Foty, R. A. and Steinberg, M. S. (1997). Measurement of tumor cell cohesion and suppression of invasion by E- or P-cadherin. *Cancer Res.* **57**, 5033–5036.

Foty, R. A. and Steinberg, M. S. (2013). Differential adhesion in model systems. *Wiley Interdiscip. Rev. Dev. Biol.* **2**, 631–645.

Foty, R. A., Corbett, S. A., Schwarzbauer, J. E. and Steinberg, M. S. (1998). Dexamethasone up-regulates cadherin expression and cohesion of HT-1080 human fibrosarcoma cells. *Cancer Res.* **58**, 3586–3589.

Friedl, P. and Gilmour, D. (2009). Collective cell migration in morphogenesis, regeneration and cancer. *Nat. Rev. Mol. Cell Biol.* **10**, 445–457.

Gillespie, J. I. (1983). The distribution of small ions during the early development of Xenopus laevis and Ambystoma mexicanum embryos. *J Physiol (Lond)* **344**, 359–377.

Glazier, J. A. and Graner, F. (1993). Simulation of the differential adhesion driven rearrangement of biological cells. *Phys. Rev. E Stat. Phys. Plasmas Fluids Relat. Interdiscip. Topics* **47**, 2128–2154.

Glen, C. M., Kemp, M. L. and Voit, E. O. (2019). Agent-based modeling of morphogenetic systems: Advantages and challenges. *PLoS Comput. Biol.* **15**, e1006577.

Gov, N. S. (2007). Collective cell migration patterns: follow the leader. *Proc Natl Acad Sci USA* **104**, 15970–15971.

Graner, F. and Glazier, J. A. (1992). Simulation of biological cell sorting using a two-dimensional extended Potts model. *Phys. Rev. Lett.* **69**, 2013–2016.

Harrison, N. C., Diez del Corral, R. and Vasiev, B. (2011). Coordination of cell differentiation and migration in mathematical models of caudal embryonic axis extension. *PLoS ONE* **6**, e22700.

Hayashi, S. and Kondo, T. (2018). Development and function of the drosophila tracheal system. *Genetics* **209**, 367–380.

Hegedüs, B., Marga, F., Jakab, K., Sharpe-Timms, K. L. and Forgacs, G. (2006). The interplay of cell-cell and cell-matrix interactions in the invasive properties of brain tumors. *Biophys. J.* **91**, 2708–2716.

Helfand, B. T., Mendez, M. G., Murthy, S. N. P., Shumaker, D. K., Grin, B., Mahammad, S., Aebi, U., Wedig, T., Wu, Y. I., Hahn, K. M., et al. (2011). Vimentin organization modulates the formation of lamellipodia. *Mol. Biol. Cell* **22**, 1274–1289.

Hernández-Vega, A., Marsal, M., Pouille, P.-A., Tosi, S., Colombelli, J., Luque, T., Navajas, D., Pagonabarraga, I. and Martín-Blanco, E. (2017). Polarized cortical tension drives zebrafish epiboly movements. *EMBO J.* **36**, 25–41.

Holtfreter, J. (1944). A study of the mechanics of gastrulation. *J. Exp. Zool.* **95**, 171–212.

Huang, Y. and Winklbauer, R. (2018). Cell migration in the Xenopus gastrula. *Wiley Interdiscip. Rev. Dev. Biol.* **7**, e325.

Inoue, Y., Suzuki, M., Watanabe, T., Yasue, N., Tateo, I., Adachi, T. and Ueno, N. (2016). Mechanical roles of apical constriction, cell elongation, and cell migration during neural tube formation in Xenopus. *Biomech. Model. Mechanobiol.* **15**, 1733–1746.

Jeong, H.-W., Hernández-Rodríguez, B., Kim, J., Kim, K.-P., Enriquez-Gasca, R., Yoon, J., Adams, S., Schöler, H. R., Vaquerizas, J. M. and Adams, R. H. (2017). Transcriptional regulation of endothelial cell behavior during sprouting angiogenesis. *Nat. Commun.* **8**, 726.

Keller, R. E. (1976). Vital dye mapping of the gastrula and neurula of Xenopus laevis. *Dev. Biol.* **51**, 118–137.

Keller, R. E. (1980). The cellular basis of epiboly: an SEM study of deep-cell rearrangement during gastrulation in Xenopus laevis. *J. Embryol. Exp. Morphol.* **60**, 201–234.

Keller, R. (1991). Chapter 5 Early Embryonic Development of Xenopus laevis. In *Xenopus laevis: Practical Uses in Cell and Molecular Biology*, pp. 61–113. Elsevier.

Keller, R. and Jansa, S. (1992). Xenopus Gastrulation without a blastocoel roof. *Dev. Dyn.* **195**, 162–176.

Keller, R. and Shook, D. (2008). Dynamic determinations: patterning the cell behaviours that close the amphibian blastopore. *Philos. Trans. R. Soc. Lond. B Biol. Sci.* **363**, 1317–1332.

Keller, R. and Tibbetts, P. (1989). Mediolateral cell intercalation in the dorsal, axial mesoderm of Xenopus laevis. *Dev. Biol.* **131**, 539–549.

Keller, R., Davidson, L., Edlund, A., Elul, T., Ezin, M., Shook, D. and Skoglund, P. (2000). Mechanisms of convergence and extension by cell intercalation. *Philos. Trans. R. Soc. Lond. B Biol. Sci.* **355**, 897–922.

Keller, R., Davidson, L. A. and Shook, D. R. (2003). How we are shaped: the biomechanics of gastrulation. *Differentiation.* **71**, 171–205.

Khalil, A. A. and de Rooij, J. (2019). Cadherin mechanotransduction in leader-follower cell specification during collective migration. *Exp. Cell Res.* **376**, 86–91.

Khataee, H., Czirok, A. and Neufeld, Z. (2020). Multiscale modelling of motility wave propagation in cell migration. *Sci. Rep.* **10**, 8128.

Krens, S. F. G., Veldhuis, J. H., Barone, V., Čapek, D., Maître, J.-L., Brodland, G. W. and Heisenberg, C.-P. (2017). Interstitial fluid osmolarity modulates the action of differential tissue surface tension in progenitor cell segregation during gastrulation. *Development* **144**, 1798–1806.

Krieg, M., Arboleda-Estudillo, Y., Puech, P. H., Käfer, J., Graner, F., Müller, D. J. and Heisenberg, C. P. (2008). Tensile forces govern germ-layer organization in zebrafish. *Nat. Cell Biol.* **10**, 429–436.

Kumar, S., Das, A. and Sen, S. (2018). Multicompartment cell-based modeling of confined migration: regulation by cell intrinsic and extrinsic factors. *Mol. Biol. Cell* **29**, 1599–1610.

Lebreton, G. and Casanova, J. (2014). Specification of leading and trailing cell features during collective migration in the Drosophila trachea. *J. Cell Sci.* **127**, 465–474.

Lecuit, T. and Lenne, P.-F. (2007). Cell surface mechanics and the control of cell shape, tissue patterns and morphogenesis. *Nat. Rev. Mol. Cell Biol.* **8**, 633–644.

Li, L., He, Y., Zhao, M. and Jiang, J. (2013). Collective cell migration: Implications for wound healing and cancer invasion. *Burns Trauma* **1**, 21–26.

Li, W., Wang, M., Ma, H., Chapa-Villarreal, F. A., Lobo, A. O. and Zhang, Y. S. (2023). Stereolithography apparatus and digital light processing-based 3D bioprinting for tissue fabrication. *iScience* **26**, 106039.

Longo, D., Peirce, S. M., Skalak, T. C., Davidson, L., Marsden, M., Dzamba, B. and DeSimone, D. W. (2004). Multicellular computer simulation of morphogenesis: blastocoel roof thinning and matrix assembly in Xenopus laevis. *Dev. Biol.* **271**, 210–222.

Manning, M. L., Foty, R. A., Steinberg, M. S. and Schoetz, E.-M. (2010). Coaction of intercellular adhesion and cortical tension specifies tissue surface tension. *Proc Natl Acad Sci USA* **107**, 12517–12522.

Marsden, M. and DeSimone, D. W. (2001). Regulation of cell polarity, radial intercalation and epiboly in Xenopus: novel roles for integrin and fibronectin. *Development* **128**, 3635–3647.

Mayor, R. and Etienne-Manneville, S. (2016). The front and rear of collective cell migration. *Nat. Rev. Mol. Cell Biol.* **17**, 97–109.

Mo, X., Ouyang, L., Xiong, Z. and Zhang, T. (2022). Advances in digital light processing of hydrogels. *Biomed. Mater.* **17**,.

Nagel, M., Tahinci, E., Symes, K. and Winklbauer, R. (2004). Guidance of mesoderm cell migration in the Xenopus gastrula requires PDGF signaling. *Development* **131**, 2727–2736.

Nagel, M., Barua, D., Damm, E. W., Kashef, J., Hofmann, R., Ershov, A., Cecilia, A., Moosmann, J., Baumbach, T. and Winklbauer, R. (2021). Capillarity and active cell movement at mesendoderm translocation in the Xenopus gastrula. *Development*.

Nam, J. and Kim, M. (2024). Advances in materials and technologies for digital light processing 3D printing. *Nano Convergence* **11**, 45.

Nguyen Edalgo, Y. T., Zornes, A. L. and Ford Versypt, A. N. (2019). A hybrid discrete–continuous model of metastatic cancer cell migration through a remodeling extracellular matrix. *AIChE J.*

Omelchenko, T., Vasiliev, J. M., Gelfand, I. M., Feder, H. H. and Bonder, E. M. (2003). Rho-dependent formation of epithelial "leader" cells during wound healing. *Proc Natl Acad Sci USA* **100**, 10788–10793.

Osborne, J. M., Fletcher, A. G., Pitt-Francis, J. M., Maini, P. K. and Gavaghan, D. J. (2017). Comparing individual-based approaches to modelling the self-organization of multicellular tissues. *PLoS Comput. Biol.* **13**, e1005387.

Pan, M., Yang, Y. and Liu, L. (2021). Physical Forces Influence the Self-organization of the Leader Cell Formation During Collective Cell Migration. In *2021 IEEE 16th International Conference on Nano/Micro Engineered and Molecular Systems (NEMS)*, pp. 1923–1926. IEEE.

Qin, L., Yang, D., Yi, W., Cao, H. and Xiao, G. (2021). Roles of leader and follower cells in collective cell migration. *Mol. Biol. Cell* **32**, 1267–1272.

Ramos, J. W., Whittaker, C. A. and DeSimone, D. W. (1996). Integrin-dependent adhesive activity is spatially controlled by inductive signals at gastrulation. *Development* **122**, 2873–2883.

Roca-Cusachs, P., Sunyer, R. and Trepat, X. (2013). Mechanical guidance of cell migration: lessons from chemotaxis. *Curr. Opin. Cell Biol.* **25**, 543–549.

Romero, S., Quatela, A., Bornschlögl, T., Bornschlög, T., Guadagnini, S., Bassereau, P. and Tran Van Nhieu, G. (2012). Filopodium retraction is controlled by adhesion to its tip. *J. Cell Sci.* **125**, 4999–5004.

Rørth, P. (2012). Fellow travellers: emergent properties of collective cell migration. *EMBO Rep.* **13**, 984–991.

Rozario, T., Dzamba, B., Weber, G. F., Davidson, L. A. and DeSimone, D. W. (2009). The physical state of fibronectin matrix differentially regulates morphogenetic movements in vivo. *Dev. Biol.* **327**, 386–398.

Sater, A. K., Steinhardt, R. A. and Keller, R. (1993). Induction of neuronal differentiation by planar signals in Xenopus embryos. *Dev. Dyn.* **197**, 268–280.

Scarpa, E. and Mayor, R. (2016). Collective cell migration in development. *J. Cell Biol.* **212**, 143–155.

Schindelin, J., Arganda-Carreras, I., Frise, E., Kaynig, V., Longair, M., Pietzsch, T., Preibisch, S., Rueden, C., Saalfeld, S., Schmid, B., et al. (2012). Fiji: an open-source platform for biological-image analysis. *Nat. Methods* **9**, 676–682.

Schötz, E.-M., Burdine, R. D., Jülicher, F., Steinberg, M. S., Heisenberg, C.-P. and Foty, R. A. (2008). Quantitative differences in tissue surface tension influence zebrafish germ layer positioning. *HFSP J.* **2**, 42–56.

Scianna, M., Preziosi, L. and Wolf, K. (2013). A Cellular Potts Model simulating cell migration on and in matrix environments. *Math. Biosci. Eng.* **10**, 235–261.

Sego, T. J., Aponte-Serrano, J. O., Ferrari Gianlupi, J., Heaps, S. R., Breithaupt, K., Brusch, L., Crawshaw, J., Osborne, J. M., Quardokus, E. M., Plemper, R. K., et al. (2020). A modular framework for multiscale, multicellular, spatiotemporal modeling of acute primary viral infection and immune response in epithelial tissues and its application to drug therapy timing and effectiveness. *PLoS Comput. Biol.* **16**, e1008451.

Sego, T. J., Comlekoglu, T., Peirce, S. M., Desimone, D. and Glazier, J. A. (2023a). General, Open-Source Vertex Modeling in Biological Applications Using Tissue Forge.

Sego, T. J., Comlekoglu, T., Peirce, S. M., Desimone, D. W. and Glazier, J. A. (2023b). General, open-source vertex modeling in biological applications using Tissue Forge. *Sci. Rep.* **13**, 17886.

Shahapure, R., Difato, F., Laio, A., Bisson, G., Ercolini, E., Amin, L., Ferrari, E. and Torre, V. (2010). Force generation in lamellipodia is a probabilistic process with fast growth and retraction events. *Biophys. J.* **98**, 979–988.

Shellard, A. and Mayor, R. (2019). Supracellular migration - beyond collective cell migration. *J. Cell Sci.* **132**,.

Shellard, A., Szabó, A., Trepat, X. and Mayor, R. (2018). Supracellular contraction at the rear of neural crest cell groups drives collective chemotaxis. *Science* **362**, 339–343.

Shook, D. R. and Keller, R. (2008). Morphogenic machines evolve more rapidly than the signals that pattern them: lessons from amphibians. *J. Exp. Zool. B Mol. Dev. Evol.* **310**, 111–135.

Shook, D. R., Kasprowicz, E. M., Davidson, L. A. and Keller, R. (2018). Large, long range tensile forces drive convergence during Xenopus blastopore closure and body axis elongation. *eLife* **7**,.

Shook, D. R., Wen, J. W. H., Rolo, A., O'Hanlon, M., Francica, B., Dobbins, D., Skoglund, P., DeSimone, D. W., Winklbauer, R. and Keller, R. E. (2022). Characterization of convergent thickening, a major convergence force producing morphogenic movement in amphibians. *eLife* **11**,.

Sive, H. L., Grainger, R. M. and Harland, R. M. (2000). *Early Development of Xenopus Laevis: A Laboratory Manual*. illustrated, revised ed. (ed. Sive, H. L.), Grainger, R. M.), and Harland, R. M.) CSHL Press.

Smith, J. C., Symes, K., Hynes, R. O. and DeSimone, D. (1990). Mesoderm induction and the control of gastrulation in Xenopus laevis: the roles of fibronectin and integrins. *Development* **108**, 229–238.

Sonavane, P. R., Wang, C., Dzamba, B., Weber, G. F., Periasamy, A. and DeSimone, D. W. (2017). Mechanical and signaling roles for keratin intermediate filaments in the assembly and morphogenesis of Xenopus mesendoderm tissue at gastrulation. *Development* **144**, 4363–4376.

Spahn, P. and Reuter, R. (2013). A vertex model of Drosophila ventral furrow formation. *PLoS ONE* **8**, e75051.

Spatarelu, C.-P., Zhang, H., Trung Nguyen, D., Han, X., Liu, R., Guo, Q., Notbohm, J., Fan, J., Liu, L. and Chen, Z. (2019). Biomechanics of collective cell migration in cancer progression: experimental and computational methods. *ACS Biomater. Sci. Eng.* **5**, 3766–3787.

Staddon, M. F., Bi, D., Tabatabai, A. P., Ajeti, V., Murrell, M. P. and Banerjee, S. (2018). Cooperation of dual modes of cell motility promotes epithelial stress relaxation to accelerate wound healing. *PLoS Comput. Biol.* **14**, e1006502.

Steinberg, M. S. (2007). Differential adhesion in morphogenesis: a modern view. *Curr. Opin. Genet. Dev.* **17**, 281–286.

St Johnston, D. and Sanson, B. (2011). Epithelial polarity and morphogenesis. *Curr. Opin. Cell Biol.* **23**, 540–546.

Swat, M. H., Thomas, G. L., Belmonte, J. M., Shirinifard, A., Hmeljak, D. and Glazier, J. A. (2012). Multi-scale modeling of tissues using CompuCell3D. *Methods Cell Biol.* **110**, 325–366.

Symes, K. and Mercola, M. (1996). Embryonic mesoderm cells spread in response to platelet-derived growth factor and signaling by phosphatidylinositol 3-kinase. *Proc Natl Acad Sci USA* **93**, 9641–9644.

Szabó, A. and Mayor, R. (2018). Mechanisms of neural crest migration. *Annu. Rev. Genet.* **52**, 43–63.

Tamargo, M. A., Nash, T. R., Fleischer, S., Kim, Y., Vila, O. F., Yeager, K., Summers, M., Zhao, Y., Lock, R., Chavez, M., et al. (2021). milliPillar: A Platform for the Generation and Real-Time Assessment of Human Engineered Cardiac Tissues. *ACS Biomater. Sci. Eng.* **7**, 5215–5229.

Tambe, D. T., Hardin, C. C., Angelini, T. E., Rajendran, K., Park, C. Y., Serra-Picamal, X., Zhou, E. H., Zaman, M. H., Butler, J. P., Weitz, D. A., et al. (2011). Collective cell guidance by cooperative intercellular forces. *Nat. Mater.* **10**, 469–475.

Tan, J. L., Tien, J., Pirone, D. M., Gray, D. S., Bhadriraju, K. and Chen, C. S. (2003). Cells lying on a bed of microneedles: an approach to isolate mechanical force. *Proc Natl Acad Sci USA* **100**, 1484–1489.

Tetley, R. J., Staddon, M. F., Heller, D., Hoppe, A., Banerjee, S. and Mao, Y. (2019). Tissue fluidity promotes epithelial wound healing. *Nat. Phys.* **15**, 1195–1203.

Townes, P. L. and Holtfreter, J. (1955). Directed movements and selective adhesion of embryonic amphibian cells. *J. Exp. Zool.* **128**, 53–120.

Unable to find information for 15582439.

Wacker, S., Brodbeck, A., Lemaire, P., Niehrs, C. and Winklbauer, R. (1998). Patterns and control of cell motility in the Xenopus gastrula. *Development* **125**, 1931–1942.

Wang, X., Merkel, M., Sutter, L. B., Erdemci-Tandogan, G., Manning, M. L. and Kasza, K. E. (2020). Anisotropy links cell shapes to tissue flow during convergent extension. *Proc Natl Acad Sci USA* **117**, 13541–13551.

Wang, S., Matsumoto, K., Lish, S. R., Cartagena-Rivera, A. X. and Yamada, K. M. (2021). Budding epithelial morphogenesis driven by cell-matrix versus cell-cell adhesion. *Cell* **184**, 3702-3716.e30.

Weber, G. F., Bjerke, M. A. and DeSimone, D. W. (2012). A mechanoresponsive cadherin-keratin complex directs polarized protrusive behavior and collective cell migration. *Dev. Cell* **22**, 104–115.

Wei, S., Xu, G., Bridges, L. C., Williams, P., White, J. M. and DeSimone, D. W. (2010). ADAM13 induces cranial neural crest by cleaving class B Ephrins and regulating Wnt signaling. *Dev. Cell* **19**, 345–352.

Winklbauer, R. (1990). Mesodermal cell migration during Xenopus gastrulation. *Dev. Biol.* **142**, 155–168.

Winklbauer, R. (2020). Mesoderm and endoderm internalization in the Xenopus gastrula. *Curr. Top. Dev. Biol.* **136**, 243–270.

Winklbauer, R. and Schürfeld, M. (1999). Vegetal rotation, a new gastrulation movement involved in the internalization of the mesoderm and endoderm in Xenopus. *Development* **126**, 3703–3713.

Wu, D., Yamada, K. M. and Wang, S. (2023). Tissue morphogenesis through dynamic cell and matrix interactions. *Annu. Rev. Cell Dev. Biol.* **39**, 123–144.

Yang, Y., Zheng, H., Zhan, Y. and Fan, S. (2019). An emerging tumor invasion mechanism about the collective cell migration. *Am. J. Transl. Res.* **11**, 5301–5312.

Yu, J. S. and Bagheri, N. (2020). Agent-Based Models Predict Emergent Behavior of Heterogeneous Cell Populations in Dynamic Microenvironments. *Front. Bioeng. Biotechnol.* **8**, 249.

Zajac, M., Jones, G. L. and Glazier, J. A. (2003). Simulating convergent extension by way of anisotropic differential adhesion. *J. Theor. Biol.* **222**, 247–259.

Zhang, Y., Thomas, G. L., Swat, M., Shirinifard, A. and Glazier, J. A. (2011). Computer simulations of cell sorting due to differential adhesion. *PLoS ONE* **6**, e24999.

Zhao, J., Cao, Y., DiPietro, L. A. and Liang, J. (2017). Dynamic cellular finite-element method for modelling large-scale cell migration and proliferation under the control of mechanical and biochemical cues: a study of re-epithelialization. *J. R. Soc. Interface* **14**,.

Zhou, S., Li, P., Liu, J., Liao, J., Li, H., Chen, L., Li, Z., Guo, Q., Belguise, K., Yi, B., et al. **(2022). Two Rac1 pools integrate the direction and coordination of collective cell migration.** ***Nat. Commun.*** 13**, 6014.**